THE DEVELOPMENT AND APPLICATION OF A DIODE-LASER-BASED ULTRAVIOLET ABSORPTION SENSOR FOR NITRIC OXIDE

A Thesis

by

THOMAS NATHAN ANDERSON

Submitted to the Office of Graduate Studies of
Texas A&M University
in partial fulfillment of the requirements for the degree of

MASTER OF SCIENCE

May 2003

Major Subject: Mechanical Engineering

THE DEVELOPMENT AND APPLICATION OF A DIODE-LASER-BASED ULTRAVIOLET ABSORPTION SENSOR FOR NITRIC OXIDE

A Thesis

by

THOMAS NATHAN ANDERSON

Submitted to Texas A&M University
in partial fulfillment of the requirements
for the degree of

MASTER OF SCIENCE

Approved as to style and content by:

Jerald A. Caton (Co-chair of Committee)	Robert P. Lucht (Co-chair of Committee)
Edward S. Fry (Member)	John A. Weese (Head of Department)

May 2003

Major Subject: Mechanical Engineering

ABSTRACT

The Development and Application of a Diode-Laser-Based Ultraviolet Absorption Sensor for Nitric Oxide. (May 2003)

Thomas Nathan Anderson, B. S., Texas A&M University

Co-Chairs of Advisory Committee: Dr. Jerald A. Caton
Dr. Robert P. Lucht

This thesis describes the development of a new type of sensor for nitric oxide (NO) that can be used in a variety of combustion diagnostics and control applications. The sensor utilizes the absorption of ultraviolet (UV) radiation by the NO molecule to determine the concentration via optical absorption spectroscopy. UV radiation at 226.8 nm is generated by sum frequency mixing the outputs from a 395-nm external cavity diode laser (ECDL) and a 532-nm diode-pumped, intracavity frequency doubled Nd:YAG laser in a beta-barium borate (BBO) crystal. This radiation is used to probe the (v'=0, v"=0) band of the $A^2\Sigma^+ - X^2\Pi$ electronic transition of NO. The ECDL is tuned so that the UV radiation is in resonance with a specific energy level transition, and it is then scanned across the transition to produce a fully resolved absorption spectrum. Preliminary experiments were performed in a room-temperature gas cell in the laboratory to determine the accuracy of the sensor. Results from these experiments indicated excellent agreement between theoretical and experimental absorption line shapes as well as NO concentrations. Further experiments were performed at two actual combustion facilities to demonstrate the operation of the sensors in realistic combustion environments. Tests on a gas turbine auxiliary power unit (APU) at Honeywell Engines and Systems and on a well-stirred reactor (WSR) at Wright-Patterson Air Force Base produced excellent results despite the harsh temperatures and vibrations present. Overall, the sensitivity was estimated to be 0.8 parts per million (ppm) of NO (at 1000 K) for a 1 meter path length and the measurement uncertainty was estimated to be ±10%.

DEDICATION

To my loving family for your unwavering love and support throughout my life. All that I am is because of you. I thank you and I love you.

ACKNOWLEDGMENTS

This research was accomplished with the support of many individuals and organizations that I would like to gratefully acknowledge. First, I would like to thank my advisor, Dr. Robert Lucht, for all of his help and patience throughout my time in this laboratory. It has been a pleasure and an honor working for such an intelligent and caring man who has provided me with an education that is far more valuable than anything I have learned in the classroom. I am truly grateful for his guidance and his friendship. I also appreciate the help of my other committee members, Dr. Jerald Caton and Dr. Edward Fry, who have been very kind and supportive throughout this research. I cannot forget Dr. Thomas Walther who, though now in Germany, has been tremendously helpful in getting this project to its present state.

I also owe a great deal of thanks to my coworkers in the lab for their help and friendship. Gus Ray introduced me to diode-laser-sensors and taught me a lot when I first began working in this lab. I thank him for his patience and knowledge in answering my many questions. Sherif Hanna did much of the initial work on the sensor before I began graduate school, and I gratefully acknowledge his hard work on the sensor. I also thank him for his genuine friendship and his loyal support throughout my graduate career. His great faith in God and amazing perseverance has been immensely encouraging to me. Rudy Barron-Jimenez has also been vital to this research in virtually every aspect. We have worked together every day since this research began, and we have even been all over the country together for the field demonstrations of the sensor. He is one of the few people that I still enjoy being around even after weeks together on the road. I thank him for his patience with me even after all this time. I also thank him for the many things he continues to teach me about science and life and for the support he has given me throughout my graduate career. I consider him a true friend. Mark Gallina took time out of his schedule to teach me LabView, which made our project much easier and faster. I appreciate his help and his quick wit to keep us laughing.

Jonathan DuBois has helped through various stages of this project, for which I am grateful. He has also been a good friend and has been a great addition to our research group. I thank all of the students in our lab for such an open and friendly environment to work in. It truly has been a blessing to be here.

A number of people were instrumental in carrying out the field demonstrations of the sensors. At Wright-Patterson Air Force Base, Dr. Jim Gord, Dr. Mike Brown, and Dr. Sukesh Roy provided valuable assistance during the experiments and many times afterwards. Dr. Scott Stouffer and Mike Arstingstall also put in many long days in the test cell to help complete the experiments. At Honeywell Engines and Systems, Ian Critchley and Luis Flamand patiently helped us through the many obstacles of the gas turbine tests. We are very grateful to everyone for their contributions to this research.

I am also indebted to several organizations for providing the necessary funding for this research. My education has been supported by the National Science Foundation through a graduate research fellowship. The equipment and other expenses of the sensor have been funded by the Air Force Research Laboratory, Propulsion Directorate, Wright-Patterson Air Force Base through Innovative Scientific Solutions, Inc. under Contract #F33615-00-C-2020, by the U.S. EPA under Project No. R-82818001, and by the U.S. DOE through Honeywell Power Systems under Contract #DE-FC02-00-CH11053.

Finally, I want to thank my family and friends for their love and encouragement through my many years of school. I could not have made it without their love and care. Most of all, I thank God for his amazing grace and love. Through Him we have everything, and I firmly trust in Him.

TABLE OF CONTENTS

LIST OF FIGURES

FIGURE Page

FIGURE Page

LIST OF TABLES

1. INTRODUCTION

Combustion processes are some of the most vital processes to our modern world. From electricity to transportation to warmth, we depend on combustion processes for almost every aspect of our lives. Despite all the beneficial results from combustion, there is unfortunately one potentially harmful byproduct, namely air pollution. Air pollution includes a host of gases and particulate emissions resulting from the combustion process that have adverse effects on humans and our environment. The sheer number of applications across the world that use combustion magnifies these harmful effects, requiring significant action on our part to prevent serious and irreparable damage to humans and the environment.

The Clean Air Act was passed by congress in 1970 to monitor six of the most harmful pollutants and enact regulations to reduce the amount of these pollutants emitted. Since then, the amounts of five of these pollutants have significantly decreased. The sixth pollutant, nitrogen oxides (NO_x), has actually increased in emission since that time.[1] To successfully reduce the emission of this pollutant, we must develop technology to detect and monitor NO_x so that we can fully understand how it is produced and how to minimize its production during the combustion process. Before getting into these details, though, let us first examine the effects of these molecules.

1.1. Relevance of the Nitric Oxide Molecule

The family of molecules labeled as nitrogen oxides, or NO_x, includes several species. The main two molecules in terms of quantities emitted and effects are nitric oxide (NO) and nitrogen dioxide (NO_2). During the combustion process, typically around 90% of the NO_x produced is in the form of NO with the remainder being NO_2.[2] For this reason,

---

This thesis follows the style and format of Applied Optics.

measurement of NO_x in combustion systems typically focuses on the NO molecule.

Numerous studies of the NO molecule have proven it to be a molecule of significant importance for both beneficial and harmful reasons. In very small quantities, NO is actually essential for human life. In fact, it plays such a vital role in biological processes that an entire journal is devoted to the study of NO.[3] Larger quantities, however, can be harmful and potentially fatal to humans. NO levels up to around 50 parts per million (ppm) can be slightly irritating to the mucous membranes. Levels between 60 and 150 ppm become increasingly irritating, causing coughing and burning of the throat. Above 200 ppm, NO can be fatal even at short exposure times.[4] Fortunately, high levels of NO rarely persist after the combustion products are exhausted to the atmosphere.

In the atmosphere, the NO molecule produces the worst effects on the environment. When exposed to air and sunlight, NO rapidly reacts to form NO_2, which in turn reacts to form ozone (O_3). Ozone is the major constituent of ground-level smog, which produces adverse health effects in humans and inhibits plant growth.[2] Many larger cities have drawn acute attention to the problem of smog. NO_2 can also react with molecules in the atmosphere to form nitric acid, which is a major component of acid rain. Acid rain is known to damage lakes and streams along with the wildlife in them.[2] It also damages forests and other vegetation.

The overall damage to the environment by these molecules has prompted many regulations and restrictions on the production of NO by combustion processes, which are the main source of NO emissions. For example, the state of California recently set emission limits for ground based gas turbines at 9 ppm (@ 15% O_2).[5] In complying with these restrictions, manufacturers have begun producing combustion equipment that emits very small amounts of NO. Advanced lean-premixed gas turbines are now capable of producing less than 10 ppm of NO.[6] With levels many times less than previous NO levels, researchers are now faced with the challenge of finding sensor equipment that can measure such small quantities of NO in order to continue reducing the emissions.

1.2. Current NO Sensor Technology

Most of the sensor technologies currently available to measure NO concentrations have been around for some time. A recent report lists the five main types of NO sensors currently used: chemiluminescent analyzers, chemical cells, FTIR analyzers, UV analyzers, and diode-laser-based sensors.[6]

The most common means of measuring NO concentration is the chemiluminescent (CL) analyzer. CL analyzers measure the concentration by measuring the intensity of light emitted during the reaction between NO and ozone. Several different manufacturers produce analyzers capable of measuring 1 to 5 ppm up to 5000 ppm. There are even instruments capable of measuring parts per billion (ppb) of NO in ambient air. While these analyzers are capable of sensitive measurements of NO, they also require physical sampling of the gas and calibration before use.

Chemical cells are another popular and accurate way to measure NO concentration. These types of sensors operate by measuring the electric current produced through the chemical reaction with an analyte. Chemical cells can be used to accurately measure 0 to 5 ppm of NO up to around 3000 ppm. Again, continuous physical sampling is required along with calibration. Furthermore, chemical cells have response times of up to 80 seconds and they are subject to temperature drift. They must also be replaced every 1 to 2 years.

A third type of NO sensor currently used is a Fourier transform infrared (FTIR) analyzer. FTIR analyzers operate using the absorption of infrared (IR) radiation by the NO molecule. An IR beam is passed from an interferometer through the gas sample and then detected. After analyzing the signal with Fourier transform analysis, it is compared with a known spectrum to determine the concentration. Concentrations down to 20 ppb can be measured with FTIR analyzers, but extractive probe sampling into a gas cell is required. The gas sample must also be dried to reduce interferences with water vapor. Interference with carbon dioxide (CO_2) still presents a problem for FTIR analyzers.

Similar to the FTIR analyzer, ultraviolet (UV) analyzers are available to measure NO concentrations down to 500 ppb. UV analyzers use a broadband ultraviolet light source

with a diffraction grating to simultaneously measure a broad range of wavelengths. After passing the dispersed UV beam through the exhaust gas in a gas cell, it is detected using a charge coupled device (CCD) array. Concentration is determined from the resulting signal. Extractive probe sampling is required for low sensitivities, although the gas temperature must be below 250°C.

The most recent and by far the most promising technology to measure NO is diode-laser-based sensors. Also commonly known as tunable diode laser absorption spectroscopy (TDLAS) sensors, they have been under development for over twenty years and continue to become more practical as laser technology rapidly advances. Allen provides an excellent review on the current state of diode-laser-based absorption sensors.[7] Diode-laser-based sensors can be used to determine the NO concentration using the well-developed technique of absorption spectroscopy. All molecules absorb energy at certain discrete levels corresponding to the internal energy levels within the molecule. When radiation at a specific energy level (which is directly proportional to the wavelength of the light) is incident on a molecule, it is partially absorbed according to well-known quantum mechanical relationships. By detecting the amount of light at a particular wavelength absorbed through a sample of gas, the concentration of the gas can be determined using the quantum-mechanical relationships along with the properties of the gas such as pressure and temperature. Many groups including ours have carried the development of these types of sensors to a point where they can begin to replace older technology. The intense interest in diode-laser-based sensors is driven by their many advantages over traditional sensor technology.

1.3. Advantages of Diode-Laser-Based Sensors

The most important advantage of diode-laser-based sensors over traditional sensor technology is the increased sensitivity. Groups have demonstrated sensitivities in the parts per billion (ppb) range for various molecules, far exceeding the limits of current sensors. This will continue to become even more important as manufacturers push the levels of NO emissions even lower in response to the stringent regulations.

Another advantage of diode-laser-based sensors is the non-intrusive nature of the measurement. Some current sensors like chemiluminescent analyzers and chemical cells require the gas to be physically sampled using a probe in the exhaust stream. This not only disturbs the flow, but it also can introduce errors in the measurement if the gas continues to react through the probe. The only requirement for diode-laser-based sensors is optical access to the gas, such as windows on both sides of the exhaust stack, so that a laser beam can be passed through the gas. Measurements provide the average concentration present at that location without chance of bias due to reactions in a probe.

Since the concentration measurements made by diode-laser-based sensors are calculated from the known structure of the molecule, an absolute concentration measurement is provided. This means that no calibration is required, unlike most other types of sensors currently used. Eliminating calibration saves both time and money for the users of the sensors.

One of the most promising features of diode-laser-based sensors is the potential for continuous, real-time measurements of pollutant concentration. With this capability, diode-laser-based sensors can be incorporated into control schemes to optimize the combustion process and minimize emissions. Indeed, one group has already demonstrated the optimization of a pulsed, 50-kW dump combustor with a diode-laser-based sensor.[8] Docquier and Candel also describe many applications of optical sensors to automotive engines, gas turbines, and several other types of combustors.[5] The benefits of this feature alone are significant not only to the users of combustion processes, but to all of society if emissions can be reduced.

Currently, the cost of these sensors is slightly greater than traditional sensor technology such as chemiluminescent analyzers. However, an advantage of these sensors is the potential use of diode lasers developed for the telecommunications industry. If these mass-produced diode lasers can be used, then these sensors would be much cheaper than current sensor technology. Even if telecommunications lasers cannot be used, the cost of the sensor will continue to decrease as laser technology improves. Furthermore, these sensors provide a much simpler and cheaper alternative diagnostic

for NO than traditional laser diagnostics such as laser induced fluorescence (LIF), coherent anti-Stokes Raman spectroscopy (CARS), and degenerate four-wave mixing (DFWM).

1.4. Objectives of This Research

Due to the obvious advantages and potential of diode-laser-based sensors, the focus of this thesis research is to develop such a sensor for NO. To achieve this end result, there are three specific objectives set forth for this research: to develop an ultraviolet laser system, to demonstrate the ability of the laser system to detect NO, and to demonstrate the sensor in a realistic environment.

For reasons discussed later, the optimum sensor for nitric oxide is based on the absorption of ultraviolet (UV) radiation by the NO molecule. Unfortunately, no diode lasers are currently produced that emit UV radiation. Recent advances in laser technology have opened up an alternative (but more complex) means of producing UV, which will be employed for this sensor. Thus, the first objective in this research is to develop a laser system capable of producing sufficient radiation at 226 nm to perform spectroscopic measurements of the NO molecule.

Once this laser system is developed, it must be tested in a controlled laboratory environment to determine that it can detect NO and can accurately measure the concentration of a well-known sample of gas. These spectroscopic measurements are essential to understanding how the sensor performs and what its limitations are.

When these are known, then the third and final objective can be addressed. This is to demonstrate the use of the sensor for making accurate measurements in a realistic combustion environment. In order for this sensor to replace existing sensors, it must withstand the conditions encountered around real combustion equipment. Successful field demonstrations of this sensor will prove the feasibility of this new sensor and pave the way for continued development into a commercial product.

1.5. Thesis Organization

The remainder of this thesis presents the design, development, and testing of the diode-laser-based UV absorption sensor for NO. The following section, *Background and Theory*, presents previous work done on diode-laser-based sensors for NO as well as research into UV generation. The theory behind absorption spectroscopy is also developed fully in that section. In *Experimental Setup and Procedure*, the layout of the sensor is discussed along with the methodology for setting up and using the sensor. Results towards all three objectives are presented in the *Results and Discussion* section. Finally, the performance of the sensor is summarized in *Conclusions and Recommendations* along with suggestions for future improvements to the sensor.

2. BACKGROUND AND THEORY

Fortunately for the development of this sensor, the theory behind absorption spectroscopy for NO is quite well understood. Much of the theory was developed from basic quantum mechanical principles in the field of statistical thermodynamics. Experimental work was done as early as the 19th century. After the arrival of the laser, the theory was strengthened with more accurate experimental results from large, laboratory-based laser systems. As laser technology has improved, diode lasers have become available at wavelengths required for NO spectroscopy, and much work has been done with these smaller, more rugged laser systems. In recent years, laser systems have been miniaturized further, allowing the development of diode-laser-based sensors. Before discussing previous diode-laser-based sensors for NO, the general theory behind absorption spectroscopy will first be developed.

2.1. Theory of Absorption Spectroscopy

All atoms and molecules absorb energy in a very specific manner, which can be accurately predicted for simpler molecules such as NO. Energy is absorbed only in very discrete quanta that correspond to changes in internal energy of the atom or molecule. A diatomic molecule like NO can be modeled as two masses connected by a spring. These masses vibrate along the internuclear axis and rotate about the center of mass of the molecule. In addition to rotational and vibrational energy, the internal energy of a molecule is also comprised of electronic energy. Each of these three internal energy modes is quantized, and therefore the molecule will only change internal energy when it is bombarded by a photon with the correct amount of energy. Hence, molecules will only absorb particular wavelengths of light that are in resonance with an energy level transition. The amount of energy absorbed for a specific wavelength can be predicted from quantum mechanical principles. In practice, a tunable laser is used to send light through a volume of gaseous molecules and the intensity of the light is measured before

and after transmission through the gas. Tuning the laser wavelength across the resonance produces an absorption spectrum. A theoretical absorption spectrum can then be fit to the experimental spectrum to determine properties of the volume of gas such as concentration and temperature.

A rigorous development of the theory required for absorption spectroscopy of diatomic molecules is found in Lucht et al.,[9] from which most of these equations are taken. A more complete description of the physical picture is also found in Herzberg.[10] According to Beer's law, the transmission of light at a frequency ν through a path length L of matter is

$$T_\nu = \frac{I}{I_0} = \exp(-k_\nu L) \tag{2.1}$$

where I is the transmitted light intensity, I_0 is the initial (or reference) light intensity, and k_ν is the spectral absorption coefficient. The absorption is simply the complement of the transmission, or

$$A_\nu = \frac{I - I_0}{I_0} = 1 - \exp(-k_\nu L). \tag{2.2}$$

The spectral absorption coefficient accounts for the strength of the energy level transition as well the proximity of the laser frequency to the resonance frequency of the transition. For a particular light frequency, ν, the spectral absorption coefficient is given by

$$k_\nu = K_{ji} g(\nu) \tag{2.3}$$

where K_{ji} is the line strength for the transition from state i state j, and $g(\nu)$ is the lineshape function or line profile. State i is typically called the ground state or lower level and state j is the excited state or upper level. The line strength for a particular energy transition centered at λ_{ji} can be found using the Einstein spontaneous emission coefficient, A_{ji}, by the relation

$$K_{ji} = \frac{1}{4}\left(\frac{g_i}{g_j}\right)(n_i - n_j)(\lambda_{ji})^2 A_{ji}. \tag{2.4}$$

The terms g_i and g_j are the degeneracies of the i^{th} and j^{th} levels while the terms n_i and n_j are the population densities of the i^{th} and j^{th} levels. For this research, the frequency of the resonances and the corresponding Einstein spontaneous emission coefficients for ultraviolet energy transitions of NO were taken from Luque and Crosley.[11] The population density of the upper level, n_j, is assumed to be zero since the upper level is typically not populated significantly even at combustion temperatures. Calculation of the lower level population density, n_i, requires more detailed knowledge of the NO molecule and will be discussed shortly. The degeneracy of the k^{th} level is found from its rotational quantum number, J, by

$$g_k = 2J_k + 1. \tag{2.5}$$

The other term required to calculate the spectral absorption coefficient (equation 2.3) is the lineshape function, $g(\nu)$. The lineshape function accounts for line broadening due to several factors, and it also accounts for the proximity of the laser frequency to the resonance frequency. Further details and references for the lineshape function can be found in Eckbreth.[12] For a particular transition, this function is a maximum when the laser frequency is equal to the resonance frequency, and it approaches zero as the laser frequency moves away from the resonance frequency. The line shape is the commonly used Voigt profile, which is a convolution of the Lorentzian and Gaussian profiles. The lineshape function involves the Voigt function $V(a,x)$ and the Doppler width $\Delta\nu_d$ in the form

$$g(\nu) = \sqrt{\frac{\ln 2}{\pi}}\frac{2}{\Delta\nu_d}V(a,x). \tag{2.6}$$

The Voigt function is given by the equation

$$V(a,x) = \frac{a}{\pi}\int_{-\infty}^{\infty}\frac{\exp(-y^2)dy}{a^2+(x-y)^2} \tag{2.7}$$

and can be calculated using well-developed numerical routines (demonstrated in the computer code in Appendix A). The parameters for the Voigt function are found from the collisional width, $\Delta\nu_c$, the Doppler width, $\Delta\nu_d$, the laser frequency, ν, and the resonance frequency, ν_{ji}, using the relations

$$a = \sqrt{\ln 2}\,\frac{\Delta\nu_c}{\Delta\nu_d} \tag{2.8}$$

and

$$x = 2\sqrt{\ln 2}\,\frac{\nu - \nu_{ji}}{\Delta\nu_d}\,. \tag{2.9}$$

The collisional and Doppler widths are parameters quantifying the broadening of the absorption line shape due to pressure and temperature effects. With no broadening, the absorption line appears as a sharp spike located exactly at the resonance frequency. There will always be some broadening, however, due to several factors. Natural broadening is always present, but its magnitude is usually negligible compared to collisional and Doppler broadening. Collisional broadening is due to the presence of other molecules of NO and other species and is directly proportional to the pressure. It is also known as pressure broadening. The width of the absorption line caused by collisional broadening, called the collisional width, is calculated from the collision-broadening coefficient, 2γ, the total pressure, P, and the temperature, T, by

$$\Delta\nu_c = 2\gamma\left(\frac{298K}{T}\right)^n P\,. \tag{2.10}$$

The coefficient n is known as the temperature exponent for the broadening coefficient, and a value of 0.75 was used as suggested by Chang et al. for NO in nitrogen (N_2).[13] The collision-broadening coefficient, 2γ, is the full-width at half maximum (FWHM) divided by the pressure (typically cited in units of cm^{-1}/atm), and it is an adjustable parameter that depends on the exact species present in the gas mixture. Chang et al.[13] and Danehy et al.[14] have previously studied the same transitions of NO and provide an excellent reference for collision-broadening coefficients.

The other source of broadening results from the motion of the molecules and the Doppler effect. Hence, it is known as Doppler broadening. The Doppler width is calculated using the molecular weight of the absorbing molecule, M_{NO}, the temperature of the gas, T, and the resonance frequency, ν_{ji}, in the relation

$$\Delta\nu_d = 7.1623x10^{-7}\sqrt{\frac{T}{M_{NO}}}\nu_{ji}. \tag{2.11}$$

The resulting units are wavenumbers (cm^{-1}) if the temperature is in Kelvin (K) and the resonance frequency is in wavenumbers (cm^{-1}).

At this point, the only unknown term is the lower level population density, n_i, from equation 2.4. From statistical thermodynamics, the relative population of a level i at thermodynamic equilibrium is given by

$$\frac{n_i}{n_{tot}} = \frac{g_i \exp\left(\frac{E_i}{kT}\right)}{Z_{tot}}. \tag{2.12}$$

where E_i is the energy of level i, k is Boltzmann's constant, T is the temperature of the gas, and Z_{tot} is the total molecular partition function. The degeneracy of level i, g_i, is found using equation 2.5. The total number of molecules, n_{tot}, is found simply using the ideal gas law and the temperature, the total pressure of the mixture, P, and the mass fraction of NO, x_{NO}. The relation is

$$n_{tot} = \frac{Px_{NO}}{kT}. \tag{2.13}$$

Both the energy of level i, E_i, and the partition function, Z_{tot}, must be calculated from a more detailed knowledge of the molecular structure of NO.

As mentioned previously, there are three modes of internal energy within a diatomic molecule: electronic, rotational, and vibrational. Each of the modes is assumed to be independent of the others so that the quantum mechanical wave equations can be solved. The term energies for electronic, vibrational, and rotational modes are labeled as T, G, and F, respectively. These term energies are related to the mode energies by the following equations:

$$T = E_e/hc \tag{2.14}$$

$$G = E_v/hc \tag{2.15}$$

$$F = E_r / hc . \qquad \textbf{(2.16)}$$

The subscripts *e*, v, and *r* represent the electronic, vibrational, and rotational modes. Figure 2.1 shows a schematic diagram of the energy levels present within a molecule for a ground and excited electronic state (n_0 and n_1, respectively). The term energies corresponding to equations 2.14 through 2.16 are indicated in Figure 2.1.

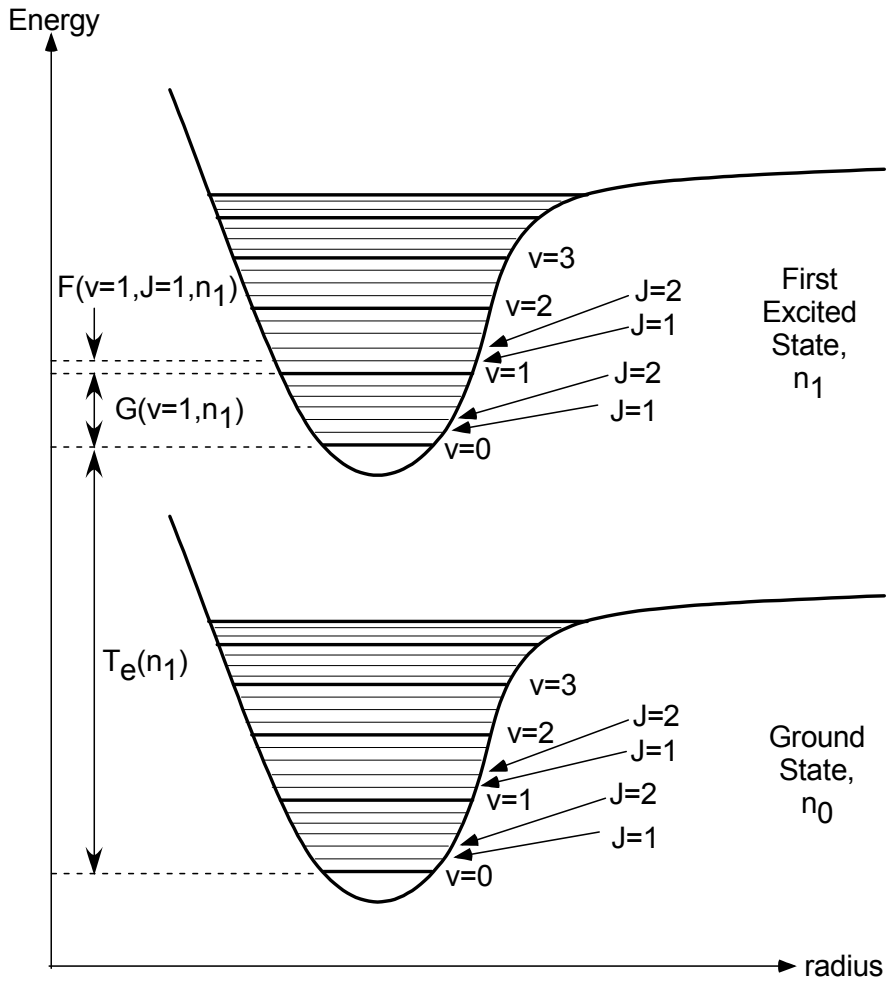

Fig. 2.1. Energy level diagram for a diatomic molecule. Thick lines indicate vibrational levels and thin lines indicate rotational levels. Higher vibrational and rotational energy levels are omitted for clarity.

The electronic energy, T_e, between two electronic states is quite well known for the NO molecule and can be found in the literature (see references 9, 10, 15, and 16). To solve for the vibrational and rotational energies, the mass and spring model mentioned earlier (known as the rigid rotator, harmonic oscillator model) is used. Solving the wave equation for this model yields simplified expressions for the vibrational and rotational term energies. For a more detailed description of the wave equations and corresponding solutions see Incropera.[17] The actual molecule is neither rigid nor harmonic, and corrections can be made for non-rigid rotation and anharmonic vibration using experimental data. The corrected vibrational term energy is found by the series

$$G(\mathrm{v}) = \omega_e\left(\mathrm{v}+\tfrac{1}{2}\right) - \omega_e x_e\left(\mathrm{v}+\tfrac{1}{2}\right)^2 + \omega_e y_e\left(\mathrm{v}+\tfrac{1}{2}\right)^3 \qquad \textbf{(2.17)}$$

where v is the vibrational quantum number and ω_e, $\omega_e x_e$, and $\omega_e y_e$ are molecular constants. The subscript e signifies that the quantity is constant for a given electronic level.

For the rotational term energy, the situation is complicated further by the coupling of the electronic and rotational angular momentum. This coupling is explained in Lucht et al. and expressions are given to calculate the different term energies.[9] However, more accurate equations for the rotational term energies are found in Reisel et al.[15] From that work, the expression for the rotational term energy of the $^2\Pi_{1/2}$ state is

$$F_1(J) = B_\mathrm{v}\left[\left(J+\tfrac{1}{2}\right)^2 - 1\right] - D_\mathrm{v}\left[\left(J+\tfrac{1}{2}\right)^4 - \left(J+\tfrac{1}{2}\right)^2 + 1\right] - B_\mathrm{v}\sqrt{\alpha} \qquad \textbf{(2.18)}$$

where Y_v is calculated specifically for this state by

$$Y_\mathrm{v} = \frac{A + C\left(J-\tfrac{1}{2}\right)^2}{B_\mathrm{v}}. \qquad \textbf{(2.19)}$$

Terms A, C, B_v, and D_v are molecular constants for NO, found in Reisel et al. (see Table 2.1 on the following page).[15] The rotational term energy of the $^2\Pi_{3/2}$ state is given in Reisel et al. as

$$F_2(J) = B_\mathrm{v}\left[\left(J+\tfrac{1}{2}\right)^2 - 1\right] - D_\mathrm{v}\left[\left(J+\tfrac{1}{2}\right)^4 - \left(J+\tfrac{1}{2}\right)^2 + 1\right] + B_\mathrm{v}\sqrt{\alpha}\,, \qquad \textbf{(2.20)}$$

and Y_v must again be specifically calculated for this state using

$$Y_{\mathrm{v}} = \frac{A - C\left(J - 1/2\right)^2}{B_{\mathrm{v}}}. \tag{2.21}$$

In equations 2.18 and 2.20, the term α is found for both states by

$$\alpha = \frac{\left(Y_{\mathrm{v}} - 2\right)^2}{4} + \left[\left(J + 1/2\right)^2 - 1\right]\left\langle 1 + 2\mu\left[2\left(J + 1/2\right)^2 - Y_{\mathrm{v}}\right] + \mu^2\left\{\left[2\left(J + 1/2\right)^2 - 1\right]^2 - 1\right\}\right\rangle \tag{2.22}$$

where

$$\mu = \frac{D_{\mathrm{v}}}{B_{\mathrm{v}}}. \tag{2.23}$$

Values for the molecular constants taken from Reisel et al. that were used in our calculations are given in Table 2.1 below.

With knowledge of the energy distribution within the molecule, both the population density and partition function can be calculated. For equation 2.12, the energy of level *i*, E_i, is simply the sum of the vibrational and rotational energies, E_{v} and E_r, calculated from the term energies using equations 2.15 and 2.16, thus

$$E_i = E_{\mathrm{v}} + E_r = \left[F(J) + G(\mathrm{v})\right]hc, \tag{2.24}$$

and *h* is Planck's constant and *c* is the speed of light in a vacuum. The partition function, Z_{tot}, required in equation 2.12 is calculated from all possible states of the

Table 2.1. Molecular constants for the NO molecule used in theoretical calculations (from Reisel et al.).[15]

Parameter	Value
B_v(v=0)	1.696190
D_v(v=0)	5.326×10^{-6}
A	123.0372
C	-1.1871×10^{-3}
ω_e	1904.405
$\omega_e x_e$	14.187

molecule. The rotational and vibrational partition functions can be considered independently, such that

$$Z_r = \sum_{N=1}^{\infty} \left\{ 2g_1 \exp\left(\frac{-hcF_1(N)}{kT} \right) + 2g_2 \exp\left(\frac{-hcF_2(N)}{kT} \right) \right\} \quad \textbf{(2.25)}$$

and

$$Z_{\mathrm{v}} = \sum_{\mathrm{v}=0}^{\infty} \exp\left(\frac{-hcG(\mathrm{v})}{kT} \right) \quad \textbf{(2.26)}$$

so the total partition function is then

$$Z_{tot} = Z_{\mathrm{v}} Z_r . \quad \textbf{(2.27)}$$

In equation 2.25, N is another form of the rotational quantum number, and g_1 and F_1 are calculated from equations 2.5 and 2.18 with $J = N + ½$, while g_2 and F_2 are calculated from equations 2.5 and 2.20 with $J = N - ½$.

Finally, the set of equations is complete to calculate the amount of light absorbed at a given frequency when passed through a certain volume of NO molecules. By calculating the spectral absorption over a range of frequencies that correspond to the tuning range of the laser, a theoretical absorption line shape results. Most of the parameters in the equations are molecular constants (Table 2.1) or measured values such as temperature, pressure, and path length. Only two parameters, the concentration of NO (x_{NO}) and the collision-broadening coefficient (2γ), remain unknown and must be varied until the theoretical absorption lineshape matches the experimental absorption line shape. In practice, the temperature is not precisely known along the entire path of the beam, so the temperature may also be varied in the calculations to optimize the fit between theoretical and absorption lineshapes. With this theoretical framework, diode-laser-based sensors can be used to measure the concentration of NO, the average temperature of the gas, and the collision-broadening coefficient for the mixture using only knowledge of the path length of the laser beam and the pressure of the mixture.

Practically, the discussion of the theory reveals one important feature of diode-laser-based sensors. That is, they require a tunable light source at frequencies corresponding to the energy level transitions of NO. Transitions for the NO molecule occur at

frequencies in the ultraviolet (UV) to the infrared (IR) region of the spectrum. However, the strongest transitions occur in the UV region of the spectrum. In particular, the (v′=0, v″=0) (abbreviated (0,0)) band of the $A^2\Sigma^+$-$X^2\Pi$ electronic transition of NO provides the optimum transitions for absorption spectroscopy of NO. Figure 2.2 shows the absorption spectrum for this particular band of NO.

Unfortunately, lasers are currently available only in wavelengths above 635 nm except for a small region around 400 nm. Therefore, most of the previous research on diode-laser-based sensors employs IR absorption due to laser technology limitations. Details of these previous systems as well as the means to probe UV transitions will be discussed next.

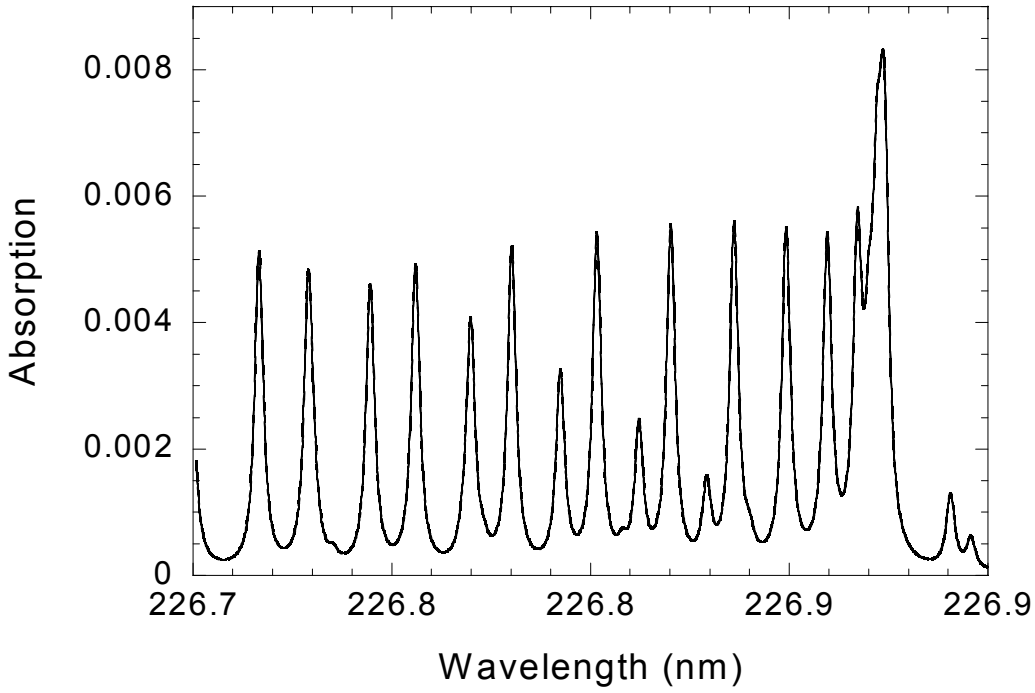

Fig. 2.2. Partial absorption spectrum of (0,0) band of $A^2\Sigma^+$-$X^2\Pi$ electronic transition of NO for 1 ppm of NO at 500 K.

2.2. Literature Review

Previous work related to this thesis falls into two categories. The most obvious category is previously developed diode-laser-based sensor systems for NO. Several such systems have been built successfully, proving the feasibility of this sensor. However, they all have drawbacks, namely IR absorption. The disadvantages of IR absorption will be discussed shortly. The sensor system developed in this thesis addresses that problem by using UV absorption instead. Accordingly, the second category of previous work relates to methods of generating UV radiation. The integration of these two areas of technology provides significant advantages for this sensor over previously developed diode-laser-based sensors for NO.

2.2.1. Previous Diode-Laser-Based NO Sensors

With one exception, all of the previously developed diode-laser-based sensors for NO are based on available lasers operating at wavelengths above 1.8 μm. Several groups have made measurements in the second overtone (3,0) absorption band of NO. Kessler et al.[18] and Sonnenfroh and Allen[19] used an experimental distributed feedback (DFB) laser operating at 1.8 μm to measure NO in several sources. After careful spectroscopic study of the NO molecule and water vapor, the $P_{11}(6)$ and $P_{21}(6)$ doublet lines were probed in order to minimize water vapor interference. Initial measurements were made in a room temperature absorption cell while higher temperature measurements were attempted in an H_2-air flame seeded with NO.[19] A dual-beam technique, called balanced ratiometric detection (BRD), was used to significantly reduce the noise in the system, resulting in a sensitivity of 3 ppmv per meter for the room temperature cell measurements. *In situ* measurements of the flame were made using a 27-pass arrangement directly above the burner. Although water vapor significantly interfered with the high temperature experiments, they reported a sensitivity of 140 ppmv per meter assuming a minimum detectable absorbance of 10^{-5}.

Mihalcea et al. also reported measurements of the second overtone absorption band of NO using an experimental DFB laser at 1.8 μm.[20] As with the previous groups, great

care was taken to choose absorption lines that were sufficiently free from water vapor interference. Ultimately, two Λ-doubled line pairs were studied: $R_{2e}(7.5) + R_{2f}(7.5)$ and $R_{1e}(7.5) + R_{1f}(7.5)$. Measurements were made as part of a multiplexed absorption sensor for several species including NO. The NO source was a CH_4-air flame seeded with ammonia and the exhaust gases were sampled and dried before flowing through a multi-pass cell. The cell provided a path length of 3276 cm for high sensitivity measurements, and the estimated sensitivity for the system is 20 ppm of NO based on a minimum absorbance of 4.5×10^{-5} in a 20 Hz noise bandwidth and a one second measurement time.

Further in the IR, Oh and Stanton demonstrated measurements in the first overtone (2,0) absorption band of NO at 2.65 μm.[21] They used a single-mode, antimonide diode laser cooled by liquid nitrogen to 183 K to perform measurements of NO in an absorption cell. Subatmospheric measurements were made of the two Λ-doublet components of the $^2\Pi_{3/2}$ R(16.5) transition of NO in the (2,0) band, which were sufficiently free from water vapor interference. With wavelength modulation spectroscopy (WMS), the reported detection limit of the sensor is 15 ppm per meter for a signal to noise ratio of 2.

For measurement of on-road vehicle emissions, Nelson et al. developed a diode-laser-based sensor for NO operating at 5.25 μm.[22] Two liquid nitrogen-cooled diode lasers operating at 5.25 μm and 4.45 μm were used to measure NO and CO_2, respectively, over a long path length across a highway. The ratio of absorption of these two molecules provided a means to calculate the absolute NO concentration using the concentration of CO_2 produced during stoichiometric combustion of gasoline. With this technique, a sensitivity of 9 ppmv was estimated assuming a three standard deviation (3σ) measurement precision.

Several groups have also performed measurements of NO using newly developed quantum cascade (QC) lasers. While these types of lasers are not traditional diode lasers, they do provide a relatively compact source of radiation at frequencies not previously available for NO spectroscopy. Measurements by these groups are all made on transitions in the fundamental absorption band of NO in the mid-IR region from 5.25

μm to 5.4 μm. Menzel et al. have used a cryogenically cooled QC-DFB laser to detect biological NO at concentrations down to 3 ppb in a 100-m path length gas cell.[23] The unresolved components of the R12.5 transition of NO were probed in this study. Sonnenfroh et al. employed a room temperature QC laser to probe the P5.5e and P5.5f transitions of NO in a room temperature absorption cell.[24] Using dual-beam, balanced ratiometric detection (BRD), they demonstrated a detection limit of 520 ppbv per meter path length for NO. Even more sensitive measurements of NO were made by Kosterev et al. using a cryogenically cooled QC-DFB laser and cavity ringdown spectroscopy (CRDS).[25] The R(13.5) doublet was chosen for these experiments. For subatmospheric, room temperature measurements in a ringdown cell, a sensitivity of 0.7 ppb NO was achieved. Finally, Wehe et al. demonstrated NO absorption measurements at 5.26 μm in the hot exhaust of a C_2H_4-air flame.[26] NO was injected into the exhaust gases above the burner and then flowed through a 1.22-m long horizontal exhaust tube with optical access. Experiments were performed using a room temperature QC laser and dual beam BRD to probe the R(6.5) transition of NO. Sensitivities of 0.36 ppm per meter were demonstrated in the experiments.

2.2.2. UV Absorption Spectroscopy

Up to this point, the NO sensors discussed are all relatively simple and straightforward in the sense that they directly employ available lasers to perform spectroscopic measurements. For this reason, they are limited to the IR region of the spectrum where available lasers coincide with energy level transitions of NO. However, IR absorption spectroscopy of NO is less than ideal for several reasons. First, water vapor, CO, and CO_2 all interfere with NO spectroscopy because of energy level transitions in similar regions of the spectrum. It is evident from the literature on IR-based NO sensors that a great deal of time and effort is spent in finding absorption lines that do not coincide with water vapor, which is a major constituent of combustion exhaust and even ambient air. Even when isolated lines can be found, interference from other molecules limits the ultimate sensitivity of the sensor because absorption lines from these molecules are usually quite broad due to the large concentrations present.

Secondly, the sensitivity of the sensors is further reduced because of the relatively weak transitions of NO that lie in the IR region.

Fortunately, both of these problems can be solved by probing transitions in the UV region of the NO absorption spectrum. Energy level transitions in the UV are many times stronger than in the IR and provide greater possible sensitivity for a sensor. Also, there are few other molecules that have transitions in the UV, eliminating almost all interferences that plague IR-based sensors. Furthermore, UV-based sensors can use room temperature, solar-blind detectors that are inexpensive and extremely sensitive. These three factors are powerful arguments for research into developing a NO sensor that utilizes UV absorption. Unfortunately, there is no readily available source of UV radiation that would suit the demands of sensor applications. The radiation source must be small, light, rugged, and relatively inexpensive to match the performance of previous diode-laser-based sensors and to compete with other sensor technology for NO. Several such sources exist that employ nonlinear optical techniques to convert the frequency of existing laser sources. These methods will be discussed in the next section.

2.2.3. Previous UV Generation Methods

Many groups have demonstrated UV generation using nonlinear optical techniques for a variety of purposes. However, consistent with our objectives, only research pertinent to diode-laser-based spectroscopy will be reviewed. As we will see, these references describe a suitable UV source for the NO sensor developed in this thesis.

The first type of nonlinear optical process useful for UV generation is second harmonic generation (SHG). This process uses a nonlinear optical crystal to generate a small amount of radiation at a frequency that is twice the frequency of the input beam. Near-UV has been generated by frequency-doubling existing diode lasers to study excited argon and CH radicals. Hancock et al. doubled the output from an 860-nm diode laser in a $KNbO_3$ crystal to study excited argon atoms at 430 nm.[27] Peterson and Oh demonstrated a similar sensor for CH radicals at 426 nm by doubling an 852-nm diode laser.[28] Further into the UV, Barry et al. detected the OH radical using 308-nm radiation produced by frequency-doubling a liquid nitrogen-cooled 616-nm diode laser in a $LiIO_3$

crystal.[29] Ray et al. also studied OH in the UV region at 266-nm by frequency-quadrupling the output of a 1064-nm external cavity diode laser (ECDL).[30] A periodically poled lithium niobate (PPLN) crystal was used to produce 532-nm radiation in the first frequency-doubling stage, and a beta-barium borate (BBO) crystal was used to generate 266-nm radiation in the second frequency-doubling stage. Finally, Koplow et al. have already measured NO in the UV at 215 nm.[31] A diode-laser-seeded tapered amplifier at 860-nm was frequency-doubled to 430 nm in a $KNbO_3$ crystal and then doubled again in a BBO crystal to generate the UV radiation. While this system demonstrates the feasibility of a diode-laser-based UV absorption sensor for NO, the tapered amplifier is very expensive.

Despite the new possible wavelengths available with SHG, laser technology is still too limited to generate the exact wavelength required for the sensor developed in this research. Specifically, we need a source of 226-nm radiation to probe the (0,0) band of the $A^2\Sigma^+ - X^2\Pi$ electronic transition of NO. Tunable lasers at the necessary wavelengths with enough power for frequency-doubling or quadrupling are not available with current laser technology. With the success of the previously mentioned UV sensor for various molecules, we look to other nonlinear optical techniques to find a suitable source of 226-nm radiation. Indeed, a promising nonlinear optical process is found in sum frequency generation (SFG). Several groups have demonstrated UV absorption sensors for various molecules using this process.

Corner et al. developed a system to measure OH at 309 nm by sum frequency mixing the output of a 404-nm diode laser with a 1320-nm DFB laser in a BBO crystal.[32] With their experimental setup, around 0.8 nW of UV radiation was produced. Oh also studied the OH radical at 308 nm using a SFG system mixing the output of an 835-nm diode laser with the output of a 488-nm Ar^+-laser in a β-BBO crystal.[33] Over 1.5 μW of UV radiation was produced in the SFG process. Deeper in the UV, Alnis et al. generated 254-nm radiation by SFG to study the mercury atom.[34] The reported system used a newly available 404-nm diode laser and a 688-nm diode laser to generate 0.9 nW of 254-nm radiation in a BBO crystal. The results from these few sensors confirm that

sufficient UV power can be generated with SFG to perform spectroscopic measurements of molecules. The only challenge that remains is finding lasers available to use in the SFG process to produce 226-nm radiation. Such lasers do exist, and the resulting system will be discussed in detail in the following chapter.

2.3. Theory of Nonlinear Optics

Before proceeding to the experimental setup of the UV absorption sensor, the theoretical background for the SFG process will be presented briefly. An excellent reference on all nonlinear optical processes is found in Boyd.[35] Some details for this discussion were also taken from Walther.[36]

Nonlinear optics refers to the phenomena that occur when intense laser light interacts with matter. When an optical field is applied to a material, a polarization is induced in the material that is dependent on the strength of the electric field. In conventional optics, the induced polarization, $\tilde{P}(t)$, depends linearly on the strength of the electric field, $\tilde{E}(t)$, as

$$\tilde{P}(t) = \chi^{(1)} \tilde{E}(t) \qquad \textbf{(2.28)}$$

where $\chi^{(1)}$ is called the linear susceptibility. Physically, it is understood that the electrons in the medium can follow the applied electric field exactly. When the strength of the applied electric field is too intense, as in a laser beam, the electrons cannot follow the applied electric field, and the induced polarization becomes nonlinear, creating new frequencies within the material. In that case, the strength of the induced polarization is given by

$$\tilde{P}(t) = \chi^{(1)} \tilde{E}(t) + \chi^{(2)} \tilde{E}(t)^2 + \chi^{(3)} \tilde{E}(t)^3 + \cdots \qquad \textbf{(2.29)}$$

where $\chi^{(2)}$ and $\chi^{(3)}$ are called the second- and third-order nonlinear optical susceptibilities.

When two different optical fields with frequencies ω_1 and ω_2 are applied to a material, the applied electric field can be represented by

$$\tilde{E}(t) = E_1 e^{-i\omega_1 t} + E_2 e^{-i\omega_2 t} + c.c. \tag{2.30}$$

In response to this electric field, the second-order contribution to the induced nonlinear polarization in the material (the second term of the sum in equation 2.29) is given by

$$\begin{aligned}\tilde{P}^{(2)}(t) = \chi^{(2)}\tilde{E}(t)^2 = \chi^{(2)}\Big[&E_1^2 e^{-2i\omega_1 t} + E_2^2 e^{-2i\omega_2 t} + 2E_1E_2 e^{-(\omega_1+\omega_2)t} \\ &+ 2E_1E_2^* e^{-i(\omega_1-\omega_2)t} + c.c\Big] + 2\chi^{(2)}\Big[E_1E_1^* + E_2E_2^*\Big]\end{aligned} \tag{2.31}$$

for a noncentrosymmetric material (for which $\chi^{(2)}$ is nonzero). The various generated frequencies within the material become evident in this expression. Pertinent to this discussion, the third term of equation 2.31 indicates that a frequency component is generated that has the sum of the two input frequencies, or

$$\omega_3 = \omega_1 + \omega_2\,, \tag{2.32}$$

which is the basis of SFG. Physically, the process occurs because photons of frequency ω_1 and ω_2 are annihilated and a photon of frequency of ω_3 is simultaneously created in a single quantum-mechanical process. An energy level diagram of the SFG process is shown in Figure 2.3.

The induced polarization given by equation 2.31 is the response of a single atomic dipole to the applied electric field. In a given volume of material, there are large numbers of atoms that all oscillate similarly. If the phases of these atomic dipoles can be

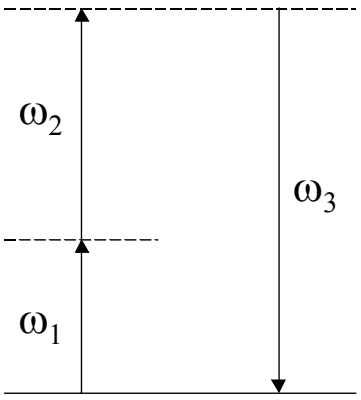

Fig. 2.3. Energy level diagram of the sum-frequency generation process.

matched correctly, then the electromagnetic field generated by each dipole will add constructively in the forward direction and result in a well-defined beam of radiation at frequency ω_3. We can determine this phase-matching condition quantitatively by solving the coupled-wave equations for the propagation of light through a nonlinear optical material. From the solution, the intensity of the generated radiation is given by

$$I_3 = \frac{512\pi^5 d^2 I_1 I_2}{n_1 n_2 n_3 \lambda_3^2 c} L^2 \mathrm{sinc}^2\left(\frac{\Delta kL}{2}\right) \qquad \textbf{(2.33)}$$

where I_1 and I_2 are the intensities of the incident electric fields, d is related to the second-order nonlinear optical susceptibility $\chi^{(2)}$, L is the length of the crystal, λ_3 is the vacuum wavelength of the generated radiation, and Δk is the wave vector (or momentum) mismatch. For the condition of perfect phase-matching, the wave vector mismatch, Δk, is zero, and the intensity of the generated radiation is maximum.

The condition for phase-matching in terms of the indices of refraction for the various waves propagating through the nonlinear optical crystal is given by

$$n_3 - n_2 = (n_1 - n_2)\frac{\omega_1}{\omega_3} \qquad \textbf{(2.34)}$$

where n_i corresponds to the index of refraction for frequency ω_i. In a typical material, the index of refraction increases with frequency (called normal dispersion). In this case, equation 2.34 cannot be satisfied since the left hand side will always be positive and the right hand side will always be negative (for $\omega_1<\omega_2<\omega_3$). It can be satisfied, however, using birefringence displayed in some crystals, where the index of refraction depends on the polarization and propagation direction of the applied field. In particular, we distinguish two beams in a uniaxial crystal: the ordinary beam, which is polarized perpendicular to the plane defined by the optic axis of the crystal and the propagation direction, and the extra-ordinary beam, which is polarized within the aforementioned plane. The index of refraction of the ordinary beam, n_o, is independent of the propagation direction while the index of refraction of the extra-ordinary beam, n_e, varies as

$$\frac{1}{n_e(\theta)^2} = \frac{\sin^2\theta}{\bar{n}_e^2} + \frac{\cos^2\theta}{n_o^2} \qquad \textbf{(2.35)}$$

as a function of incidence angle θ with respect to the optic axis. The quantity $\bar{n}_e$ is the principal value of the extra-ordinary refractive index. By orienting the incident optical fields correctly into the birefringent, nonlinear optical crystal, equation 2.34 can be satisfied and perfect phase-matching can be achieved.

The most commonly used nonlinear optical crystal used for SFG of UV radiation is a beta-barium borate (BBO) crystal. A useful resource for BBO crystals is the Inrad, Inc. website.[37] BBO crystals have a negative uniaxial optical symmetry. For uniaxial crystals, there are two schemes for phase-matching, called Type I and Type II phase-matching. In this research, we use Type I phase-matching where the two incident optical fields (ω_1 and ω_2) are both polarized linearly in the same direction. The phase matching condition for negative uniaxial crystals becomes

$$n_3^e\omega_3 = n_1^o\omega_1 + n_2^o\omega_2 \,. \qquad \textbf{(2.36)}$$

where n_i^e and n_i^o are the extra-ordinary and ordinary indices of refraction, respectively, for frequency ω_i, and n_3^e can be calculated with the help of equation 2.35. Thus, by rotating the crystal, $n_3^e(\theta)$ can be adjusted until equation 2.36 is satisfied and perfect phase-matching is achieved.

With this development, it is now clear how UV can be generated using the nonlinear optical process of SFG. Summarizing, we can produce radiation of frequency ($\omega_1 + \omega_2$) by directing two collinear laser beams of frequency ω_1 and ω_2 into a BBO crystal at an angle of θ relative to the optical axis of the crystal. If one of the incident beams is a tunable radiation source, then the resulting UV radiation will also be tunable. Therefore, the required features of lasers for our system are the following:

1. A continuous wave (cw), single-mode, tunable laser with a large mode-hop-free tuning range.
2. A high-power, cw, fixed frequency, single-mode laser.

In general, tunable diode lasers have relatively low output powers, so the fixed frequency laser source in our system must provide the majority of the power for sufficient UV generation. Both lasers must be single-mode so that the linewidth of the UV radiation is much narrower than the linewidths of the NO transitions as required for fully-resolved spectroscopic measurements. Additionally, the tunable laser must be able to tune without mode-hopping to another longitudinal mode within the laser cavity so that the resulting UV is scanned continuously across the absorption line. This mode-hop-free tuning range must be larger than the expected linewidth of the NO transitions to completely scan across the absorption line for accurate measurements.

Recent advances in laser technology have led to lasers with these characteristics, enabling the development of the compact UV laser source used for our diode-laser-based sensor. External cavity diode lasers (ECDLs) have become widely available in practically every wavelength available in diode lasers. ECDLs provide narrow linewidth, tunable radiation by extending the laser cavity with a movable diffraction grating. A resonant cavity is formed between the back facet of the diode and the diffraction grating so that a single longitudinal mode is amplified when the diffracted wavelength matches a mode within the resonant cavity. By translating and rotating the diffraction grating at the same time, both the cavity length and the diffracted wavelength can be changed simultaneously and mode-hop-free tuning is achieved over tens to hundreds of GHz. They also provide coarse-tuning of the wavelength over a few nanometers so that a wide range of transitions can be probed with the sensor. These characteristics along with their relative simplicity make ECDLs well suited for our sensor application.

Another innovation in laser technology has led to an ideal high power, fixed frequency laser source for diode-laser-based sensor applications. CrystaLaser® very recently introduced an all-solid-state laser based on a diode-pumped Nd:YAG that is intracavity frequency doubled to produce single-mode radiation at 532 nm with powers up to 200 mW. These lasers are extremely compact and rugged, ideal for a portable NO sensor. This laser source, when sum-frequency mixed with a 395-nm ECDL available

from Toptica Photonics, Inc., provides the necessary UV radiation for our sensor. In the next chapter, the construction of the sensor based on these two laser sources will be discussed.

3. EXPERIMENTAL SETUP AND PROCEDURE

With the review of previous diode-laser-based sensors for NO, the general layout of the sensor is fairly straightforward. For our sensor, the laser source is more complicated than previous sensors because sum-frequency generation (SFG) is required to generate UV radiation. As described in the previous chapter, the UV source is actually two laser sources mixed in a nonlinear optical crystal. After the laser source, however, the layout of our sensor is similar to that of previous sensors. In the remainder of this section, the details of the layout and the required components for the sensor will be described. The general setup and alignment procedures will also be outlined along with the data acquisition methodology. Finally, the specific setup of three different experiments with the NO sensor will be explained.

3.1. Components and Layout of Laser System

The detailed optical layout of the NO sensor system is shown in Figure 3.1. Generally, the system is relatively simple: outputs from two continuous wave (cw) lasers (395 nm and 532 nm) are aligned and focused into a BBO crystal where UV radiation at 226.8 nm is generated by SFG. Then, a beamsplitter directs half of the UV radiation onto a photomultiplier tube (PMT) for detection as the reference signal. The remainder of the UV radiation is sent through the medium of interest and finally to a second PMT for detection of the absorption signal. Each component will now be explained individually.

3.1.1. Lasers

In addition to the wavelength requirements for SFG, both lasers have specific roles in the system. The 395-nm external cavity diode laser (ECDL) provides the tunable input radiation required to generate tunable UV radiation in the SFG process. The other laser in the system (532 nm IFD Nd:YAG) provides high power to compensate for the

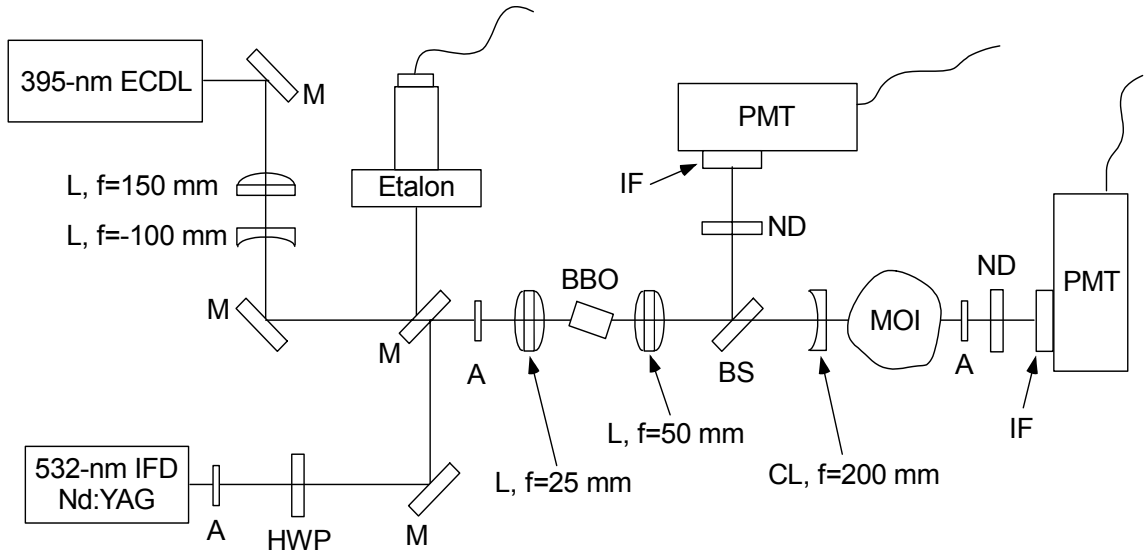

A - Aperture, BS - Beamsplitter, CL - Cylindrical Lens, HWP - Half-Wave Plate, IF - Interference Filter, L - Lens, M - Mirror, MOI - Medium of Interest, ND - Neutral Density Filter, and PMT - Photomultiplier Tube

Fig. 3.1. Schematic of NO sensor layout.

low power of the tunable laser. With this combination of lasers, the tunable UV radiation generated is sufficient to perform spectroscopic measurements of NO.

For the tunable laser source, a Toptica Model DL-100 ECDL operating at 395 nm (blue) was used. The laser head is controlled by a Toptica Controller with temperature and current control as well as modulation capabilities. The output can be coarsely tuned from 394.2 nm to 397.4 nm. The power of the output depends on injection current, but a maximum power of 15 mW is available. To prolong the life of the diode, lower injection currents were used, resulting in a laser power of 8 mW typically (for an injection current of 48 mA). The output laser beam has a diameter of approximately 1 mm and is linearly polarized in the vertical direction. Due to the construction of the laser cavity using a diffraction grating, the spectral width of the laser output is extremely narrow. Analysis of the etalon spectrum for the ECDL shows a linewidth on the order of

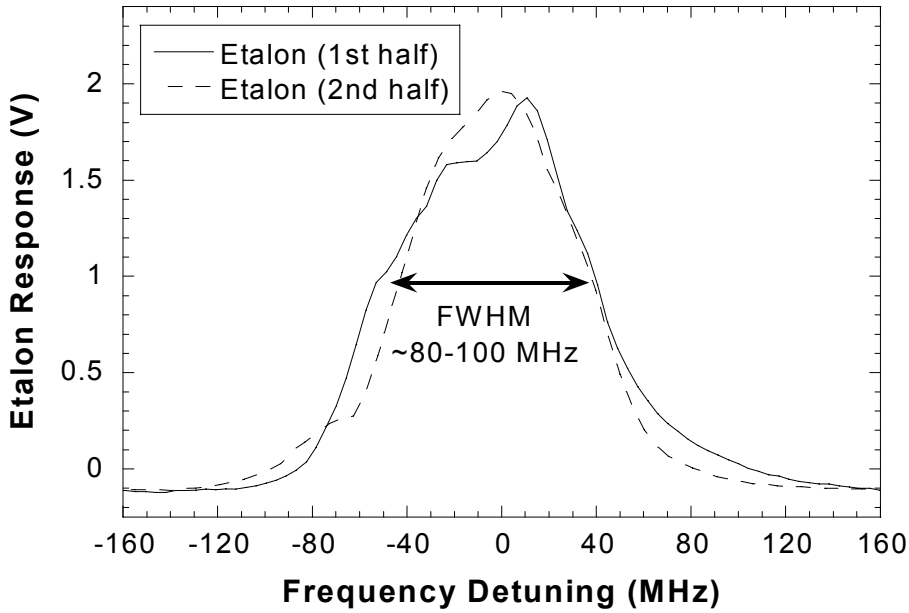

Fig. 3.2. Etalon spectrum for the 395-nm ECDL showing a laser linewidth of 80 to 100 MHz (FWHM).

80 to 100 MHz as shown in Figure 3.2. The exact linewidth is approximately 80 MHz, determined from many such traces.

Tuning the ECDL is accomplished by moving the diffraction grating inside the laser head. A piezoelectric crystal is located between the grating mount and the tip of a finely threaded screw so that the laser can be tuned finely (with the piezoelectric crystal) and coarsely (with the screw). Coarse tuning with the screw was done before the experiments to center the wavelength on the desired NO transition. Fine-tuning of the center wavelength was achieved with small adjustments in the temperature and current of the diode.

During the experiments, the ECDL was tuned back and forth across the absorption line by applying a ramp voltage to the piezoelectric crystal via the Scan Control Module (SC 100) in the controller. A maximum ramp voltage range of –20 V to 20 V can be applied to the piezoelectric crystal at rates of up to 10 kHz. Typically, the laser was scanned at a rate of 5 Hz over the maximum range (±20 V). However, other adjustments

were required to achieve mode-hop-free tuning over this entire tuning range. The SC 100 module has a feed-forward setting that can be adjusted to achieve mode-hop-free tuning. The feed-forward applies a simultaneous modulation of the laser injection current using a ramp proportional to the applied piezoelectric crystal voltage ramp (output ramp). Changing the feed-forward adjusts the ratio of these two ramps, allowing up to $1/50^{th}$ of the amplitude of the output ramp to be applied to the injection current. In addition to the feed-forward, the injection current also had to be adjusted slightly to achieve mode-hop-free tuning over the entire range. Once set, however, the feed-forward typically did not require further adjustment, but the injection current required occasional tweaking to maintain mode-hop-free tuning. With proper current and feed-forward settings, a mode-hop-free tuning range of 24 GHz was achieved.

The high-power laser source is a green, fixed frequency, diode-pumped, intracavity frequency doubled (IFD) Nd:YAG laser made by CrystaLaser®. The power was measured to be >115 mW. The 532.299 nm (vacuum) output is single-mode with a linewidth of $1x10^{-5}$ nm (10.6 MHz). Both the single mode operation and the frequency were checked in the laboratory before experiments began. The output beam has a diameter of 0.36 mm ($1/e^2$) and is linearly polarized at 45° from the horizontal. This laser is ideal for sensor applications because of the high power available and the extremely small size (3 cm x 3 cm x 12 cm).

3.1.2. Sum Frequency Generation Setup

To generate UV radiation in the BBO crystal, the outputs from both lasers were overlapped and focused into the crystal. Care was taken to match the size and polarization of the beams to maximize the UV generation. For the green beam, a half-wave plate was used to rotate the polarization of the beam to vertical to match the polarization of the blue laser. The half-wave plate was anti-reflection (AR) coated for 532 nm. The half-wave plate was placed at a slight angle relative to the incident beam so that the reflection did not follow the original beam path. An aperture located immediately after the green laser was used to block the back reflection and maintain the stability of the laser cavity. After the half-wave plate, the green beam was reflected

twice using mirrors AR coated for 532 nm. Two reflections provided the necessary degrees of freedom required to align the beam through the BBO crystal.

For the blue beam, the polarization was already vertical as required for the type I mixing in the BBO crystal. The size of the beam was slightly larger than the green beam, however, so a telescope was required to reduce the size of the beam. The telescope consisted of a plano-convex lens with f = 150 mm (nominal) and a plano-concave lens with f = -100 mm (nominal). Both lenses were AR coated for 395 nm. One of the lenses was fixed in position while the other was placed on a translation stage to precisely control the separation between the two lenses. When the separation of the two lenses was exactly equal to the sum of the focal lengths, then the beam was collimated as it left the second lens, and the size was reduced by a factor of 1.5. The ability to control the collimation of the beam allowed us to match the focal point of the blue beam in the BBO crystal. Since the focal length of a lens depends on the wavelength of the light, the blue and green beams (when collimated) will have different focal lengths when focused by the same lens into the BBO crystal. By causing the blue beam to diverge or converge slightly before entering this common lens, the focal point of the blue beam could be adjusted to match that of the green beam. Hence, the telescope allowed us to match both the size and focal points of both beams, thereby maximizing the generated UV radiation within the BBO crystal.

Similar to the green beam, the blue beam was reflected twice before entering the BBO crystal. Both mirrors were AR coated for 400 nm. To align the blue beam collinearly with the green beam, the blue beam was sent through the back of the second green mirror. This arrangement was chosen to maximize the transmitted power of both beams, since the green beam suffers greater attenuation through fused silica. Typically over 80% of the blue power was transmitted through the green mirror. Furthermore, the small reflection from the back of this mirror was useful in monitoring the wavelength and frequency spectrum of the blue laser. The reflection was directed into a Burleigh SA-Plus Spectrum Analyzer (free spectral range of 2 GHz) for monitoring the frequency spectrum while tuning the ECDL. Alternately, a removable mirror was used to direct the

reflection to a Burleigh WA-1000 cw wavemeter to determine the vacuum wavelength of the ECDL.

After the second green mirror, both beams were aligned and collinear. A bi-convex lens with f = 25 mm and AR-coated for 350-650 nm focused both beams into the BBO to increase the intensity of the beams and therefore increase the nonlinear response of the crystal. The BBO crystal was manufactured by Inrad, Inc. and is designated "OPO2". It was cut at 57.5° and coated for 532 nm and 395 nm on the entrance face and 226 nm on the exit face. The crystal has a cross section of 4 mm x 4 mm and a length of 8 mm. The crystal came from the manufacturer mounted in a small protective housing which was attached to an electronically controlled piezoelectric rotation stage from Newport. This allowed the crystal to be rotated in extremely small increments to a phase-matching angle of 61.2° as required for type I mixing of 395-nm and 532-nm radiation. The rotation stage was subsequently mounted to a translation stage so that the crystal could be moved along the beam path to optimize the location of the focal point and hence maximize the UV generation within the crystal. The generated UV radiation was collimated using a plano-convex lens with f = 50 mm and coated for 222 nm. This lens was mounted on a translation stage to finely adjust its position so that the UV beam was properly collimated. The resulting UV radiation was polarized in the horizontal direction.

3.1.3. Detection System

All the components up to the collimating UV lens comprise the laser source for our sensor. The remainder of the sensor is arranged in a manner similar to the previous diode-laser-based sensors reviewed in the previous chapter. The scheme common to these sensors is dual-beam detection. In this scheme, the laser source is split into two beams, called signal and reference beams. The reference beam is detected immediately to serve as the reference intensity of the laser source. The signal beam is sent through the medium of interest and then detected. The simultaneous detection of both beams allows for the subtraction of common-mode noise and etalon effects in the optical system, which significantly increases the possible sensitivity of the sensor.

For our sensor, a beamsplitter coated for 226 nm was used to split the UV into the signal and reference beams. The beamsplitter was manufactured to reflect 50% of the radiation when incident at 45° with p-polarization. The reflected beam served as the reference beam, and it was detected immediately with a solar-blind photomultiplier tube (PMT). The beam transmitted through the beamsplitter was the signal beam, and it was directed through the medium of interest and then onto another solar-blind PMT. The PMTs were Hamamatsu R166 side-on type with a photo-cathode area of 8 mm x 24 mm. They were mounted in PR1402 SHCE housings from Products for Research and powered by Stanford Research Systems Model PS325 high voltage power supplies. Mounted to each PMT housing was an interference filter centered at 228 nm to block the fundamental 395-nm and 532-nm beams. The filters were manufactured by Andover Corporation and have a bandwidth of 25 nm (FWHM) and a peak transmission of 23% at 228 nm. At 226 nm, the transmission is approximately 22%. In addition to the interference filters, neutral density (ND) filters were used in both beam paths to reduce the intensity of the beam into the PMT in order to maintain linearity of the detectors and prevent saturation. Several different optical density filters were used, but all were UV fused silica metallic ND filters from Newport Corporation.

After the initial construction of the sensor laser system, one more component was added to improve the operation of the system. The UV beam was observed to diverge significantly in the horizontal direction, especially over the long path of the signal beam. A CCD camera was used to investigate the UV beam, and it was observed to diverge to a width of over 25 mm at a distance of 3 m after the BBO crystal. In the vertical direction, the UV beam was well collimated to a height of around 2 mm at the same point. Figure 3.3 shows the image from the CCD camera at this point in the beam. To correct for this, a square, cylindrical plano-convex lens with a focal length of 200 mm was placed in the signal beam path after the beamsplitter. When located at the proper position, the UV beam was sufficiently collimated in the horizontal direction to a width of approximately 3 to 5 mm, even at a path length of 3 m.

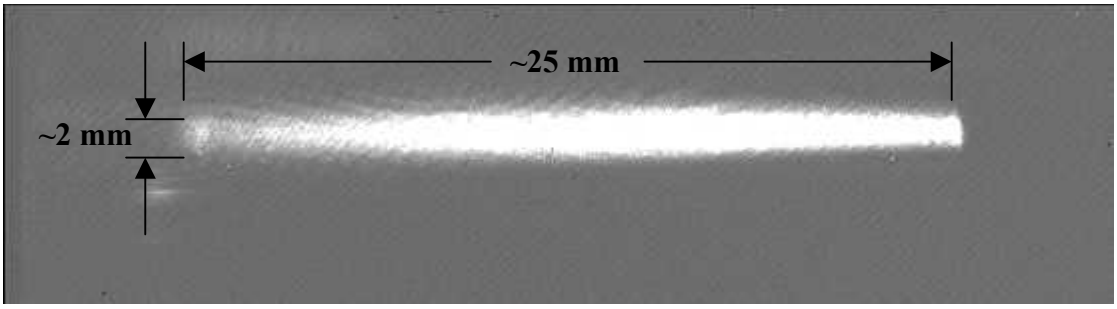

Fig. 3.3. Image of UV beam taken approximately 3 m from BBO crystal with a CCD camera. The estimated dimensions of the beam are indicated to show the horizontal divergence.

3.2. Alignment Procedure

The alignment of the laser beams into the BBO crystal is critical to producing the maximum possible UV radiation in the SFG process. A detailed procedure is required to ensure the collinearity of the blue and green beams and to match the size and focus of both beams in the BBO crystal. The procedure followed in the development of this sensor is outlined here.

The first step in aligning the system was mounting the two lasers at the proper height. This height was dictated in our system by the BBO crystal, mount, and rotation stage. All optics and lasers were mounted so that the beams passed through the center of BBO crystal. Once the lasers were mounted, the two apertures were placed along the center of the sensor (as shown in Figure 3.1) to aid in the alignment of the two beams. When these were located at the proper height, then each beam was aligned through these two points using the two mirrors. Before aligning the green beam, however, the half-wave plate was mounted in the path of the green beam. Since the half-wave plate was rotated slightly to prevent back reflection into the green laser, it would have steered the beam if mounted after aligning through the apertures. The aperture between the green laser and the half-wave plate was mounted at the same time as the half-wave plate to block the back-reflection from the waveplate. The blue beam was aligned after the green beam since the blue beam had to pass through the second green mirror, and any

movement in the green mirror would have misaligned the blue beam. When aligning the blue beam, care was taken to allow the small reflection from the back of the green mirror to pass by the mirror mount so it could be used for the spectrum analyzer and wavemeter.

Once both beams were roughly aligned through the apertures with only the mirrors, the lenses were added to the system. The best method was to work from back to front to simplify the alignment procedure. The first lens mounted was the collimating lens after the BBO crystal. Although the beams diverged substantially after placing this lens in the path, it was still aligned easily by opening the last aperture to the size of the beams. For precise alignment, the lenses were rotated (horizontally and vertically) so that the back reflections from the lens followed the incident beam path. This procedure was then repeated for the lens in front of the BBO crystal (the focusing lens). These two lenses composed a telescope, so the spacing between them was roughly equal to the sum of the focal lengths of each lens. Initially, the focusing lens was placed at this approximate distance and then checked to see if there was sufficient room between the two lenses to mount the BBO crystal on the translation and rotation stages. Exact positioning of the collimating lens was done later after a UV beam was generated and detected. When checking the back reflections from the focusing lens, the beam was blocked immediately after it so that the back reflections from the collimating lens did not interfere.

The same procedure was followed for the two lenses in the blue telescope beginning with the lens closest to the BBO crystal and finishing with the lens closest to the blue laser. The lens closest to the ECDL was mounted on a translation stage to allow for adjustment of the focal point of the blue beam at the BBO crystal. Again, the separation of the two lenses was the sum of the two focal lengths (retaining the negative sign for the concave lenses). This separation was adjusted precisely later, so the placement of the lenses was only approximate for this initial alignment.

At this point, both beams were aligned collinearly and focused through the point where the BBO crystal would be. However, with the rough alignment through the apertures, the two beams were not yet overlapped spatially at the focal point within the

BBO crystal. To precisely overlap the two focal points, a 25-μm pinhole was used. The pinhole was first placed on the translation stage where the BBO crystal would be mounted. Then, with the blue beam blocked, the pinhole was aligned horizontally, vertically, and along the beam path so that it was located at the waist of the green beam. Alignment was aided by a power meter to measure the power transmitted through the pinhole. Typically, over 80 to 90% of the green power was transmitted through the pinhole when located at this position. For example, in the latest alignment of the system, the power before the BBO focusing lens was 94 mW, and 86 mW was measured after the pinhole.

Once the pinhole was aligned with the green beam, the green beam was blocked and the blue beam was aligned. The horizontal and vertical location of the focal point was adjusted slightly using the first telescope mirror. Although adjusting the vertical and horizontal location of the beam maximized the power through the pinhole, the focal point of the beam could still lie before or after the pinhole. Therefore, the longitudinal location of the focal point was optimized by adjusting the separation between the two lenses in the blue telescope. An iterative procedure of moving the translation stage and then adjusting the vertical and horizontal location of the beam was required to find the global maximum for transmission of the blue beam through the pinhole. Around 33% of the blue beam was consistently transmitted through the pinhole in all alignments. In the latest alignment, the power before the BBO focusing lens was 5.85 mW and it dropped to 1.9 mW after the pinhole. At this optimized position, both focal points were spatially overlapped and UV generation should be maximized in the BBO crystal. The pinhole was then removed and replaced with the rotation stage and the BBO crystal.

For initial detection of the UV beam, a PMT was mounted directly after the collimating lens after the BBO crystal. This ensured that any generated UV was detected by the PMT since all three beams were essentially collinear at this point. Before looking for UV, the polarization of the green beam was checked with a polarizer to ensure it was vertically polarized. Optimization of the polarization was done after the UV beam was detected. With proper alignment and polarization of the beams, the

remaining factor required for SFG was the phase-matching angle of the BBO crystal. To find the correct phase-matching angle, the crystal was rotated with the motorized rotation stage until UV was detected with the PMT. Usually, the blue laser was scanned while looking for UV to aid identification of the signal. During scanning, a ramp voltage was applied to the diffraction grating in the ECDL, causing the wavelength of the ECDL to be tuned up and back down in a ramp function. A representative signal from the PMT when scanning is shown in Figure 3.4. The intensity modulation of the UV beam during scanning arises because the blue laser power varies during scanning due to the modulation of the injection current by the feed-forward setting.

Once any amount of UV signal was found, the system was then optimized to produce the maximum possible UV power. The first item adjusted was the rotation of the BBO crystal. After optimizing the BBO crystal angle, the location was optimized using the translation stage beneath the BBO crystal to move the crystal along the beam path. The

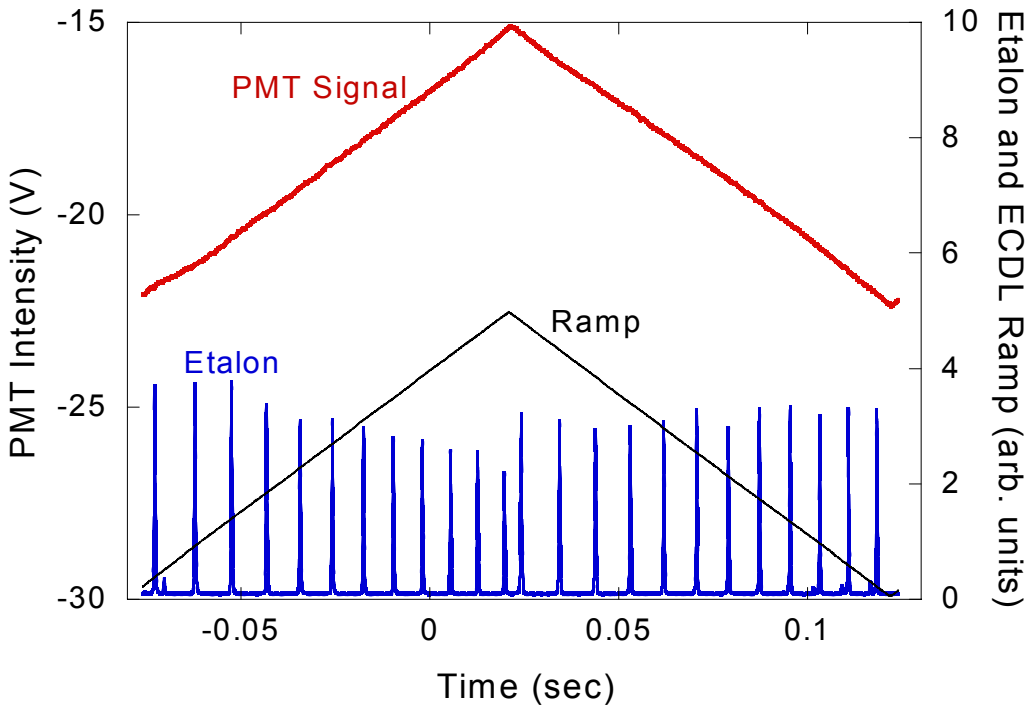

Fig. 3.4. Representative trace from the PMT during scanning. The voltage ramp applied to the ECDL is shown along with the frequency spectrum of the ECDL recorded by the etalon.

half-wave plate for the green beam was also rotated to maximize the UV signal. Finally, the actual beam paths were adjusted very slightly to optimize the overlap of the focal points in the BBO. This was a delicate process because the alignment was very sensitive. The mirrors sometimes had to be adjusted in tandem so that the beam was actually translated instead of just deflected. The second lens of the blue telescope could also be adjusted slightly to optimize the alignment of the beams. When all of these items were adjusted, then the maximum generated UV power was achieved, and the sensor was ready to make spectroscopic measurements after mounting the detectors.

With a UV beam successfully generated within the BBO crystal, the remainder of the sensor had to be set up to make spectroscopic measurements. Since the UV beam follows the fundamental beams closely, the intense green beam was used to align the UV beam closely enough to get a signal on the PMTs. Once a UV signal was detected with the PMT, then the beam could be aligned optimally. The beamsplitter was mounted after the collimating lens after the BBO crystal, and the reference PMT was mounted to detect the reflection from the beamsplitter. Care was taken to ensure that the beamsplitter was 45° to the incident beam so that around 50% of the light was reflected as designed. ND filters were added as needed to attenuate the UV beam entering each PMT to prevent the PMT from saturating. For the signal beam, multiple configurations were used depending on the medium of interest. Gas cell measurements were the simplest, where the signal beam was sent directly from the beamsplitter through a 30-cm long gas cell. The signal PMT was then mounted to detect the signal beam immediately after the gas cell. For the field tests, multiple reflections through the gas sample were required before sending the signal beam to the PMT. These specific configurations will be discussed in more detail later in this chapter.

3.3. Data Acquisition Setup and Experimental Procedure

The basic components of the data acquisition system are shown in Figure 3.5 along with the major components of the laser system. All data was collected through a four-channel, digital oscilloscope (Tektronix TDS 3014). The following signals were

recorded on the four channels: the ramp from the ECDL drive electronics, the spectral response of the ECDL from the etalon, the voltage from the reference PMT, and the voltage from the signal PMT. The oscilloscope was connected to a personal computer via a GPIB cable to record the data automatically. A program written in LabView software was used to record the data from the oscilloscope, and additional programs were written to process the data to determine the concentration and other parameters of NO in the medium of interest. The processing was not automatic, however, because several scans must be taken before the data can be processed. The details of the data acquisition and processing procedure will be discussed next.

Before performing the experiments, the first step was coarse-tuning the ECDL to a wavelength that produced UV near the resonance of the desired transition. When the ECDL wavelength was within 0.001 to 0.01 nm of the required wavelength, then temperature and injection current were adjusted to fine-tune the wavelength to the exact resonance wavelength of the transition. The ECDL was scanned at these settings to check for mode-hop-free tuning using the spectrum analyzer. Usually, the feed-forward and the injection current were adjusted until the laser scanned mode-hop-free over 24 GHz. Occasionally, the temperature and even coarse-tuning had to be adjusted to find a

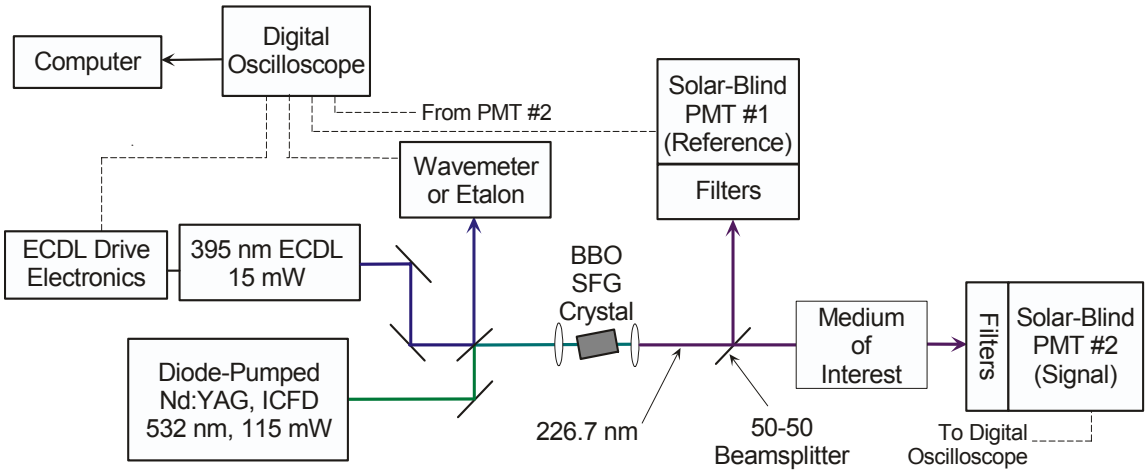

Fig. 3.5. Schematic diagram of NO sensor showing data acquisition components and general optics. Laser beams are shown with solid lines and BNC cables are indicated with dashed lines.

suitable operating range for the diode where mode-hop-free tuning over 24 GHz could be achieved. After all adjustments, the wavelength of the ECDL was rechecked. Typically, a deviation of 0.001 nm from the required center frequency was allowed; otherwise, further adjustments were made until the desired wavelength and mode-hop-free tuning range was achieved.

With the green laser turned on and the ECDL scanning, UV was generated in the BBO crystal and detected on both PMTs. Before starting the experiments, the signals from the PMTs were matched using two methods. Neutral density (ND) filters were placed in the beam path so that the signals were roughly half of the saturation values. For the PMTs used in our sensor, saturation usually occurred for output voltages around –60 V, therefore ND filters were used to attenuate the output voltages to roughly –30 V. Low attenuating filters (e.g. 90% transmission) were used to match output voltages between the two PMTs. The applied voltages from the power supplies were also adjusted to closely match the output voltages between the two PMTs. Values of 900 to 1000 V were typically applied to the PMTs.

Once the lasers and detectors were properly adjusted, experiments were started. During the experiments, the ECDL was scanned at a rate of 5 Hz across the transition with the internal ramp function on the laser controller. Initial scans were taken without NO present in the medium of interest to serve as a reference. After recording several scans without NO, the medium of interest was changed (i.e. flowed gas into the gas cell or ignited the combustor) and scans were taken with NO present in the medium of interest. For each scan, the oscilloscope recorded all four channels (ramp, etalon and both PMTs) averaged over 32 points, typically. For the gas cell measurements, oscilloscope averaging produced good results since very little noise was present in the laboratory. However, for the field demonstrations further averaging was required to reduce the high frequency noise present during the experiments. In the LabView software 10 separate scans were acquired every 0.5 second and averaged together. For a single scan the typical acquisition time was around 4 seconds, and the total acquisition time for the 10-scan average was 45 seconds. The relatively long acquisition time is due

to the data transfer of the 10,000 points for each of the four channels. No attempt was made to reduce or optimize the acquisition time for these preliminary experiments.

With the two scans acquired with and without NO present in the gas sample, the data was processed to determine the concentration of NO. Figure 3.6 shows the raw data from the gas cell experiments for a scan with only air present in the cell. The typical matching between PMT output voltages is evident in this scan. Figure 3.7 shows a subsequent scan recorded with NO present.

The normalized transmission is determined from the ratio of the voltages from the signal and reference PMTs for both scans by

$$Normalized\ Transmission = \frac{\left(\frac{\text{Signal}}{\text{Reference}}\right)_{\text{with NO}}}{\left(\frac{\text{Signal}}{\text{Reference}}\right)_{\text{without NO}}}. \qquad \textbf{(3.1)}$$

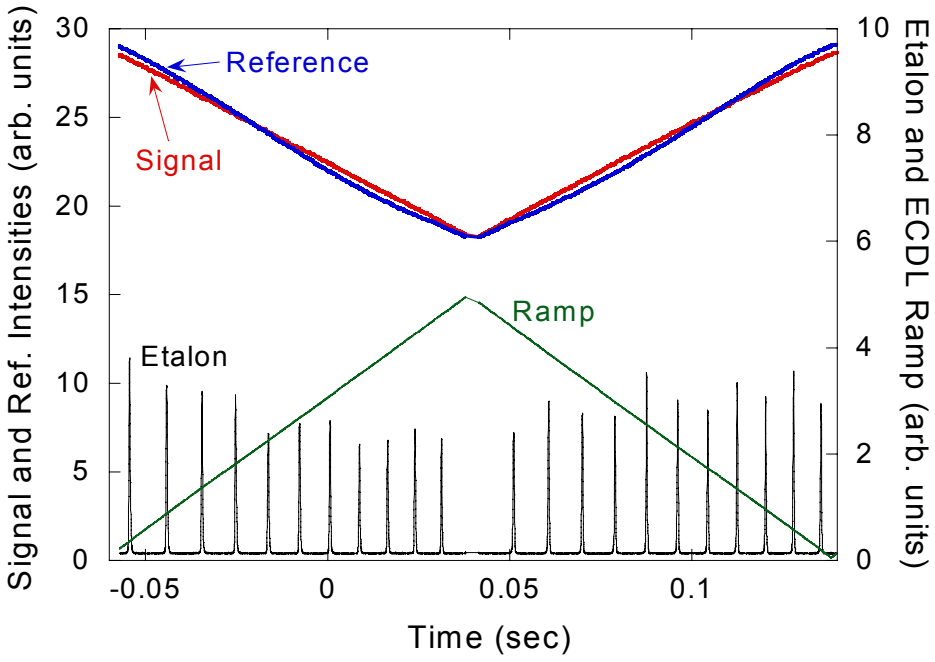

Fig. 3.6. Raw data recorded during the gas cell experiments for a scan taken with pure air present in the gas cell.

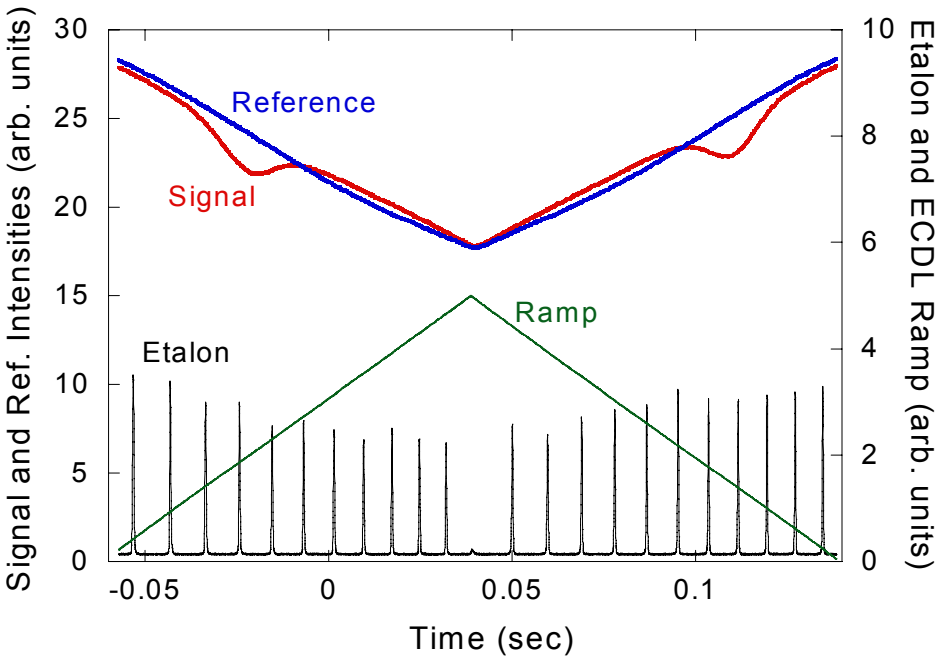

Fig. 3.7. Raw data recorded during the gas cell experiments for a scan with NO present in the gas cell.

If we examine the numerator and denominator of this expression individually, then the necessity of taking scans without NO becomes obvious. Figure 3.8 shows the comparison of these two ratios. Clearly, the different responses of the two detectors contribute to the observed structure in the baseline of Figure 3.8. By taking the ratio of these two ratios, this structure is eliminated. Furthermore, this procedure reduces the effects of PMT drift and laser power fluctuations, and it also accounts for possible etalon effects. The resulting normalized transmission for the scans in Figures 3.6 and 3.7 is shown in Figure 3.9. Finally, the normalized absorption, as required for Equation 2.2 from the previous section, is found by subtracting the normalized transmission from unity.

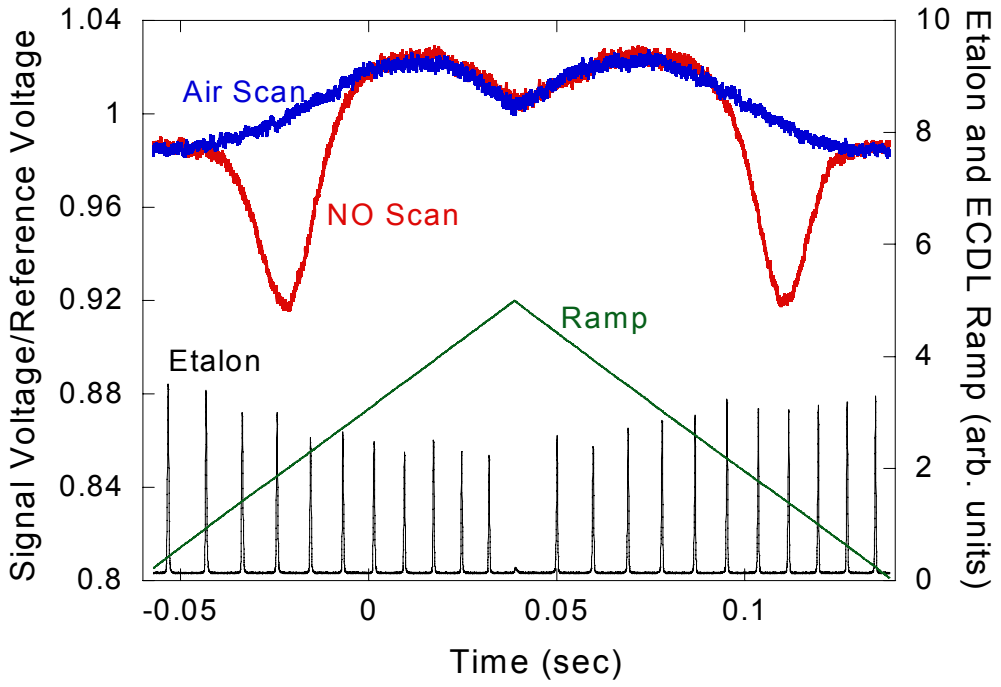

Fig. 3.8. Ratio of Signal PMT voltage to Reference PMT voltage for scans with NO and scans without NO present in the medium of interest. Structure in baseline is evident in both scans.

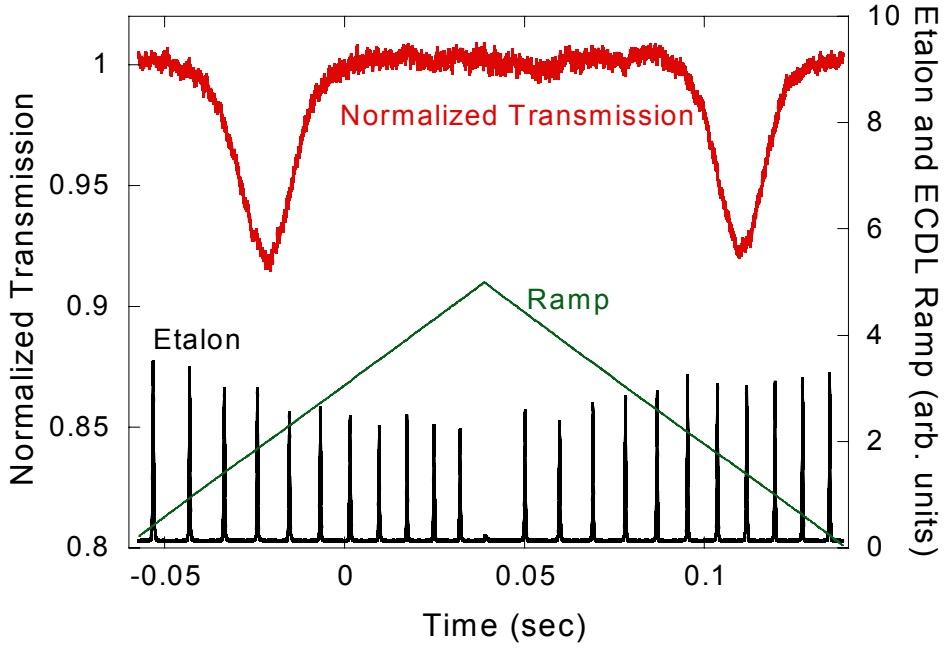

Fig. 3.9. Normalized transmission for the traces shown in Figures 3.6 and 3.7 calculated by Equation 3.1.

With the normalized absorption calculated for the scan, two more steps were required before the NO concentration could be calculated. Since the theoretical equations developed in the previous chapter depend on the frequency of the laser, the absorption spectrum must be converted from time domain to frequency domain. The recorded etalon trace is the key to this conversion since peaks occur every 2 GHz (the free spectral range, FSR, of the etalon). During tuning of the ECDL, the diffraction grating actually speeds up as it moves through one pass of the scan. Therefore, the peaks become more closely spaced as the scan progresses, as evident in Figures 3.6 to 3.9. A second or third order polynomial can be fit to the centers of each etalon peak (in seconds) to determine the relationship between time and frequency. Figure 3.10 shows an example of this process along with the best-fit equations for frequency for each half of the scan. Note that the frequency increases by 2 GHz for each peak in the first half and decreases by 2 GHz for each peak in the second half, as dictated by the actual

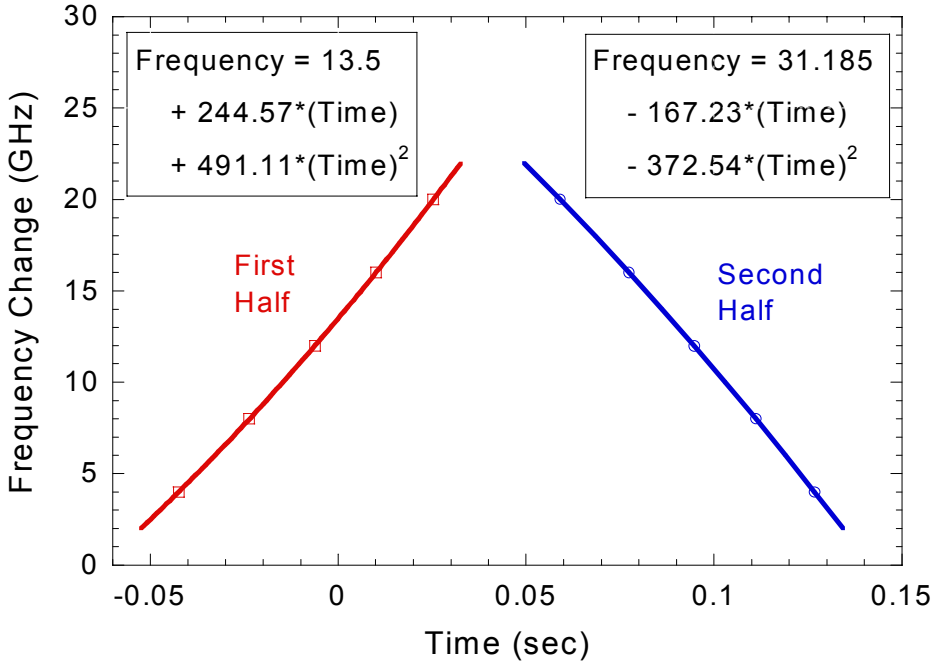

Fig. 3.10. Time vs. frequency plot for a representative absorption spectrum. The center of each etalon peak is plotted on the abscissa and the FSR (2 GHz) of the etalon is plotted on the ordinate.

scanning of the ECDL (wavelength decreases as ramp voltage increases). Using these equations, the absorption spectrum is converted from a time scale to a frequency scale. Usually the absorption spectrum was first divided in half before frequency conversion. The ECDL ramp served as the guide for the turnaround where the scan was divided.

At this point, there were actually two separate absorption spectra that correspond to each half of the scan. These two spectra were then used to fit the theoretical absorption spectrum and determine the theoretical concentration and other parameters. The theoretical absorption spectrum was calculated with a FORTRAN code that we developed using the equations from the previous chapter. The code is included in Appendix A for reference. To simplify the fitting process, this code was incorporated into a LabView program that displayed the two halves of the experimental absorption along with the calculated theoretical absorption spectrum. For most of the data presented in this thesis, the data was fit manually by adjusting parameters and running the code until the theoretical and experimental absorption spectra fit well visually. The data was also averaged further with the LabView program by binning 20 to 50 neighboring channels recorded by the digital oscilloscope. This reduced the electronic read noise from the oscilloscope's 10,000 channels, and we verified that it did not change the spectral line shapes. The resulting spectrum from this processing procedure is shown in Figure 3.11 on the next page.

3.4. Laboratory Gas Cell Experimental Setup

Initial experiments with the sensor were performed in the laboratory in a room temperature gas cell. The 30-cm long gas cell was located in the signal beam between the beamsplitter and the signal PMT. The cylindrical lens was not required in these experiments due to the relatively short path length of the beam. Windows in the gas cell were fused silica windows AR-coated for 226 nm. A Pfeiffer vacuum pump was used to evacuate the cell to pressures below 2 torr. The pressure within the cell was measured using an Omega PX205-015A1 pressure transducer with an uncertainty of ±2 torr.

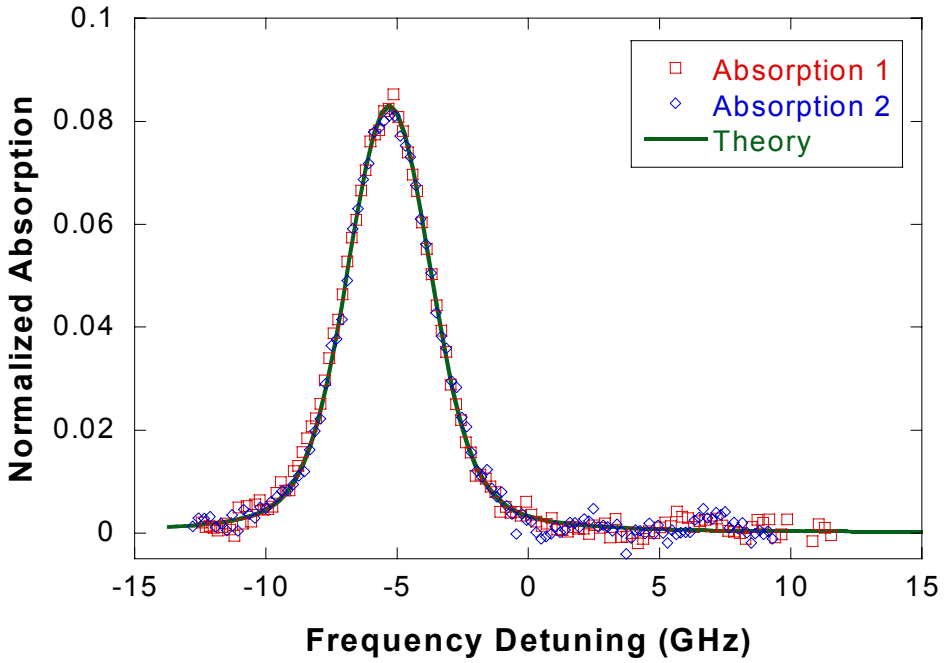

Fig. 3.11. Representative theoretical and experimental absorption spectra resulting from the data processing routine.

Tests were performed on a mixture of 100 ppm NO in N_2 from Matheson. The mixture was certified to be within 10% of the nominal concentration (90 - 110 ppm NO). The procedure was quick and straightforward. First, the gas cell was purged several times with pure air or N_2 and then vacuumed down the desired pressure. Several scans were taken for air following the data acquisition procedure described previously. Next, the cell was purged several times with the NO/N_2 mixture and then vacuumed down to the desired pressure. Again, several more scans were taken with NO present in the cell. This procedure was repeated for a variety of pressures from 300 torr down to around 2 torr. Several different transitions were also probed during the course of the experiments. Table 3.1 on the following page summarizes the transitions and pressures examined during the gas cell experiments. The wavelength settings for the lasers are also indicated in the table.

Table 3.1. Summary of NO transitions probed during gas cell experiments. Wavelengths for the blue and green lasers are also indicated for each experiment.

Date	NO Transitions Probed	Center of Transition, cm^{-1}	ECDL Wavelength, nm (vac)	Green Wavelength, nm (vac)
1/2/02 – 1/11/02	$P_2(10)$, $^QP_{12}(10)$	44087.79, 44087.77	395.235-395.237	532.299
1/14/02, 4/8-4/12/02	$P_2(2)$, $^QP_{12}(2)$ $P_2(5)$, $^QP_{12}(5)$	44078.08 44077.71, 44077.70	395.389-395.394	532.299
1/15/02	$P_2(3)$, $^QP_{12}(3)$ $P_2(4)$, $^QP_{12}(4)$ $P_2(5)$, $^QP_{12}(5)$	44077.42 44077.30 44077.71, 44077.70	395.398	532.299

3.5. Field Test Experimental Setup

After verifying the operation of the sensor in the laboratory, experiments were performed on actual combustion equipment at two locations to demonstrate the sensor in the field environment. The first tests were performed at Honeywell Power System in Phoenix, Arizona on a 90 kW gas turbine auxiliary power unit (APU). The APU is a smaller gas turbine engine with a generator and compressor connected to the front portion of the main shaft. It is designed to provide cabin air and electrical power to airplanes while the engines are off. Fuel flow is controlled in the APU to maintain a constant turbine speed, so the equivalence ratio changes as loads are applied to either the compressor or the generator. In this way, a variety of combustion conditions (and therefore NO levels) were tested in the APU. The sensor is shown next to the APU in the photograph in Figure 3.12.

Tests were also performed at Wright-Patterson Air Force Base in Dayton, Ohio on a well-stirred reactor (WSR) apparatus. A well-stirred reactor is a laboratory tool that simulates an ideal gas turbine combustor. A variety of combustion conditions can be tested with the WSR, and indeed many effects have been studied such as lean blowout and emissions.[38] Details on the initial design of the WSR can be found in Nenniger et al.[39] A photograph of the NO sensor set up at the WSR facility is shown in Figure 3.13.

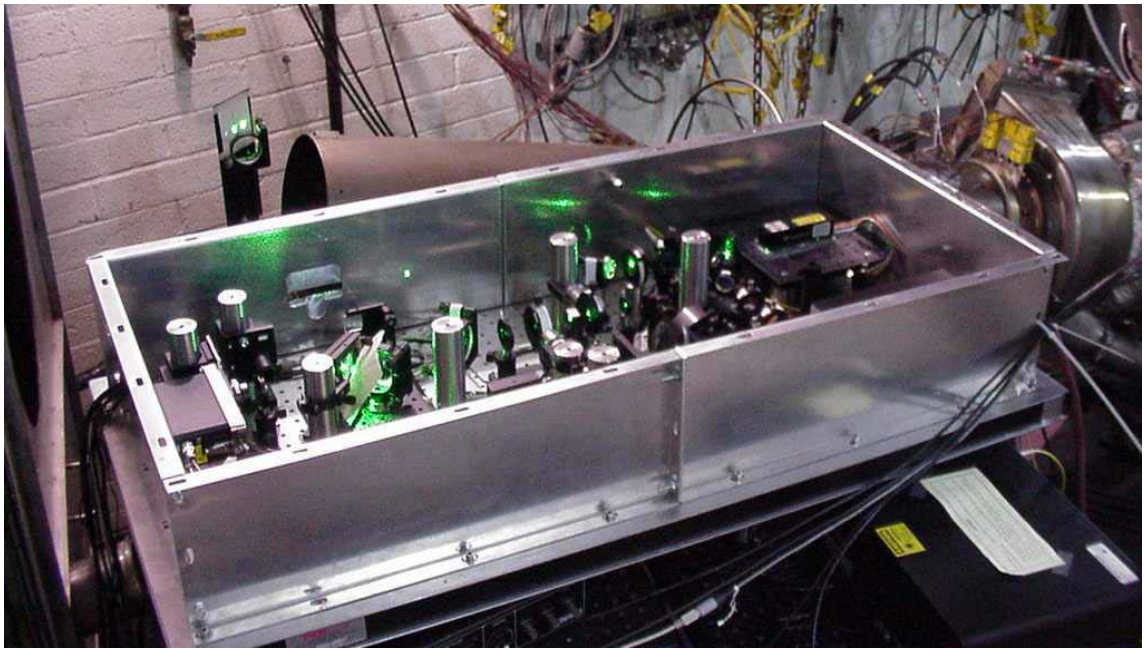

Fig. 3.12. Photograph of the NO sensor by the gas turbine APU. The sensor is shown mounted on a 0.6 x 1.2-m optical breadboard with part of the aluminum enclosure (top is not shown).

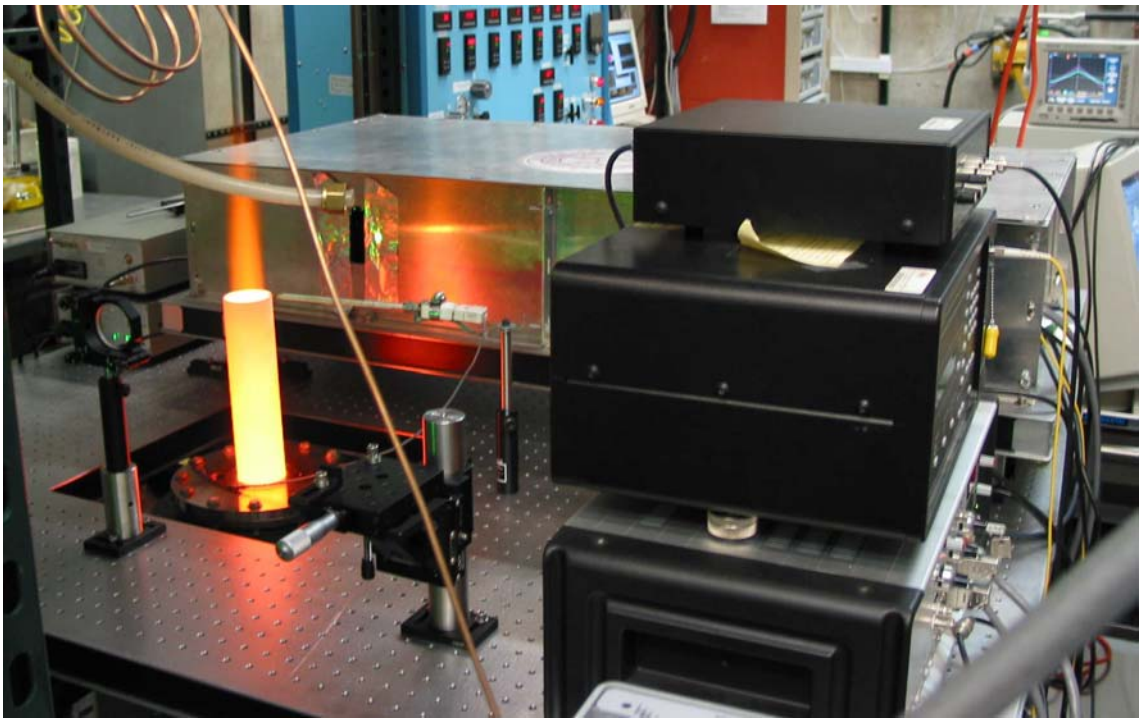

Fig. 3.13. Photograph of the NO sensor and equipment setup for measurements on the WSR at Wright Patterson Air Force Base.

Environments at both facilities were much more severe than the laboratory environment, so there were additional requirements in the setup and operating procedure of the sensor. All of the components of the sensor were moved to a 0.6 x 1.2-m optical breadboard to facilitate transportation to the different locations. An aluminum enclosure was also built to protect the sensor during travel and testing. The breadboard and enclosure (without the top) are visible in Figure 3.12. The layout of the optics in the sensor remained the same except for a modification of the signal beam path. This modification is shown in Figure 3.14a. To protect the signal PMT from high temperatures and excessive vibrations during testing, it was kept inside the sensor housing. Therefore, a mirror coated for 226 nm was added after beamsplitter to send the signal beam out of the sensor housing and through the combustor exhaust. Another mirror coated for 226 nm was placed on the opposite side of the exhaust to reflect the signal beam back through the exhaust and into the sensor housing. A third mirror was located inside the sensor to send the signal beam into the PMT for detection. Also, a

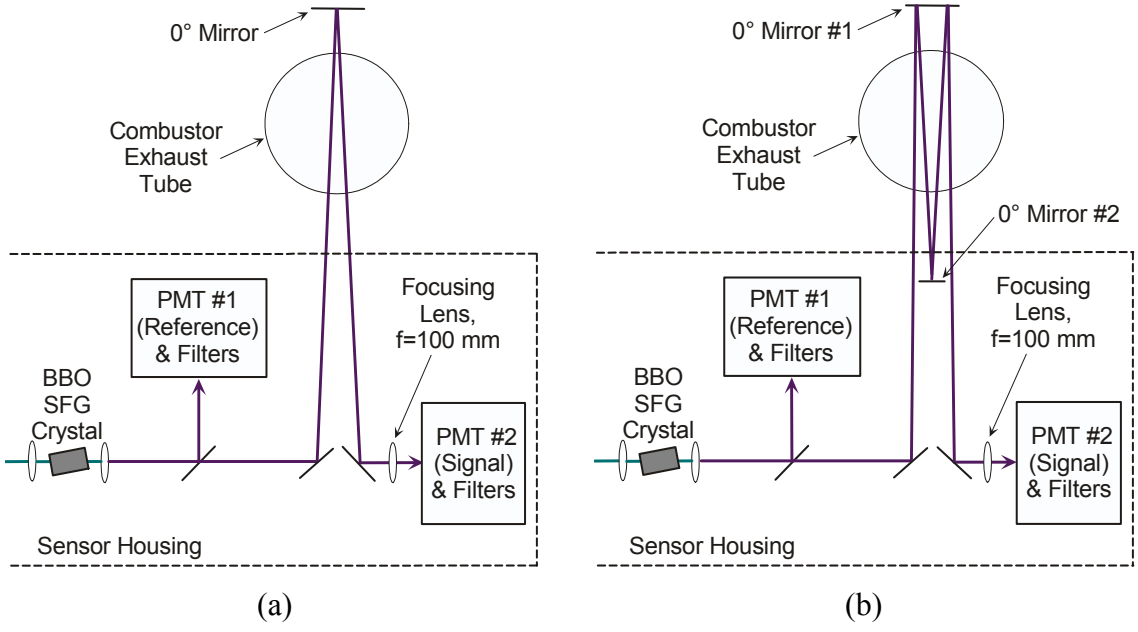

Fig. 3.14. Layout of signal beam for the a) two-pass arrangement used for the gas turbine APU experiments and b) four-pass arrangement used for the WSR experiments.

lens coated for 226 nm with a focal length of 100 mm was mounted approximately 75 mm from the signal PMT to reduce the size of the UV beam on the detector face. This reduced the effects of beam steering caused by the hot exhaust gases from the combustors.

At both facilities, precautions were taken to minimize the effect of high temperatures and excessive vibrations. The reflective finish on the aluminum enclosure was kept to lower radiative heat transfer to the sensor from the high temperature flames. During testing, a low flow rate of dry air or N_2 was forced through the sensor housing to maintain a constant temperature for the lasers and optics. Great care was also taken to reduce vibrations transmitted to the sensor because of the sensitivity of the lasers, especially the ECDL, to movement. At both facilities, the sensor breadboard was mounted on optical benches and vibration isolation pads to minimize the effect of vibrations on the operation of the sensors.

The sensors were mounted near each combustor so that the signal beam passed approximately 5 mm from the edge of exhaust tube. The beam passed along the diameter of the tube to maximize the path length for each pass. For the gas turbine APU, the exhaust tube was 25.4 cm in diameter, and the two-pass arrangement just described was sufficient to measure the NO present in the exhaust. At the well-stirred reactor facility, the exhaust tube was only 5 cm in diameter so more passes through the exhaust were needed to make accurate spectroscopic measurements of the NO present. An additional mirror was added on the sensor side of the exhaust to add two more reflections through the exhaust stream. This is depicted in Figure 3.14b. The mirror was coated for 226 nm and was only 25 mm in diameter to allow the beam to pass on both sides, as shown in the figure. Since the exhaust tube of the WSR was vertical, the four passes were arranged vertically so that each pass traversed a path length equal to the diameter of the tube (5 cm). The first pass from the sensor was located the closest to the exhaust tube exit (5 mm above), and the final pass was approximately 5 cm above the exit.

Temperatures of the exhaust gases were measured during experiments at both facilities using thermocouples. Knowledge of the temperatures provided a starting point for processing the data and simplified the fitting process. It also provided a means to check the accuracy of the results. At Honeywell, temperatures were measured at three radial locations on the large diameter exhaust tube. The K-type thermocouples were located at the exit of the exhaust tube in the same plane as the beam path. On the WSR, a single B-type thermocouple was placed just beside the first pass of the UV beam across the exhaust (i.e. 5 mm above the tube and almost in the center of the exhaust stream). Temperatures were continuously monitored at both facilities but only recorded when each scan was taken.

Concentrations of NO in the exhaust gases were also monitored during both field demonstrations to compare with measurements from our sensor. At both facilities, the gases were probe-sampled and analyzed with chemiluminescent analyzers. Samples were taken at four radial locations on the gas turbine APU and averaged together to provide a mean concentration measurement. The probes were located in the middle of the 1.8-m long exhaust tube on the APU, so they were approximately 0.9 m upstream from the beam path. At the WSR facility, samples were taken with only one probe located in the center of the exhaust about 1 cm downstream of the beam location. Before beginning tests at both facilities, the analyzers were spanned and calibrated to ensure accuracy of the measurements.

Uncertainty of the analyzer readings is estimated at 3.6% for the WSR facilities. This was calculated from the uncertainty in the calibration gases and the systematic error. For the calibration gases, the uncertainty in the mixture fraction is 2%, and the systematic error in the analyzer is estimated to be 3%. Therefore, the total uncertainty in the readings is the square root of the sum of the squares, or 3.6%. The analyzer used in the APU experiments has an uncertainty of ±1% according to the Honeywell technicians.

As evident in Figure 3.13, the conditions near the WSR were benign enough that people were allowed near the reactor during testing. Therefore, all of the equipment and controllers were set up beside the sensor as in the laboratory. For the APU tests,

however, the conditions were much worse, and people were not allowed in the test cell while the APU was running. Hence, the sensor equipment setup was modified to control the sensor remotely from outside the test cell. The ECDL laser controller, digital oscilloscope, and computer were set up in the control room to continuously monitor and record data from the sensor. The controller was connected to the laser head with special 15-m long cables custom fabricated and tested by Toptica. Both PMT outputs and the etalon output were transferred from the test cell to the oscilloscope using 15-m long BNC cables. The remainder of the equipment (CrystaLaser controller, wavemeter, and PMT voltage supplies) did not require continuous monitoring or control and was therefore left in the test cell near the sensor.

Before each test, the wavelength of the ECDL was checked with the wavemeter inside the test cell. Adjustments were also made to ensure mode-hop-free tuning of the ECDL. Finally, the voltages of the PMT power supplies were adjusted to match the signal levels on each PMT. Then, the lid was replaced on the sensor housing and tests were begun after everyone evacuated the test cell.

With the configurations just described, tests were run at both facilities on a variety of NO levels. Measurements were made first at conditions with the highest possible temperature in each combustor where the maximum levels of NO were produced. Then, measurements were made at several leaner conditions where levels of NO decreased. Finally, absorption scans were taken at the leanest possible condition of each combustor to test the detection limit of the sensor. The results from these field demonstrations as well as the laboratory gas cell experiments are described in detail in the next chapter.

4. RESULTS AND DISCUSSION

The results of this thesis research will be discussed in three categories consistent with the objectives outlined in the first chapter. First are the results of the basic setup and alignment of the laser system to generate UV radiation. Second, the results from the initial spectroscopic measurements made of NO in a laboratory gas cell are presented. Finally, the results from the field demonstrations are explained individually for both of the facilities tested. We begin with the results from the initial setup of the laser system.

4.1. UV Generation Results

The first step in the development of the sensor was to successfully generate enough UV power to perform spectroscopic measurements of NO. According to Koplow et al., powers on the order of 1 nW are sufficient for this purpose.[31] In fact, UV power greater than around 0.5 nW cannot be detected with the PMTs used in this sensor (including interference filters) without saturating the PMTs. However, to explore the capabilities of our laser system and verify the alignment, the first main goal was to generate the maximum possible amount of UV radiation. This maximum power was then compared to the theoretical power to confirm that the components and alignment of the sensor were correct.

To determine the theoretical amount of UV power generated in the SFG process, the computer program SNLO was used. This free software is available from Sandia National Laboratories to analyze many different nonlinear optical processes.[40] The *2D-mix-LP* module of the program was used in conjunction with the *Focus* and *Qmix* modules to calculate the theoretical UV power. With the *Focus* module, the beam diameter and radius of curvatures were calculated from the estimated beam waist diameter and the distance to focus (half the length of the crystal, or 4 mm). The remaining parameters for the *2D-mix-LP* module were found from the *Qmix* module. Parameters used in the final calculation of the UV power are listed in Table 4.1.

Table 4.1. Summary of values used in SNLO code to calculate the UV power generated in the SFG process.[40]

Parameter	Signal Beam	Idler Beam	Pump Beam
Wavelengths (nm)	532.3	395.3	226.8
Indexes of Refraction	1.674	1.694	1.686
Phases at input (rad)	0	0	0
AR coated (1=yes, 0=no)	1	1	1
Crystal Loss (1/mm)	0	0	0
Energy/Power (J or W)	0.098	0.0058	--
Pulse length (fwhm ns)	0	0	0
Beam diameter (fwhm mm)	0.0345	0.0287	0.0283
Supergaussian Coefficient	1	1	1
Walkoff angles (mrad)	0	0	76.43
Offset in wo dir. (mm)	0	0	0
Radius of Curvature (mm/air)	3.6	4.59	9.10
# of integ/grid points	100	128	128
Crystal/grid sizes (mm)	8	0.67766	0.06
Deff (pm/V)	1.40	--	--
Delta k (1/mm)	0	--	--
Distance to image (mm)	0	--	--
# time steps	50	--	--

For early calculations of the UV power, a beam waist diameter of 15 μm was used for the focus inside the BBO crystal. Also, the power of the ECDL was slightly higher than in later calculations. With these values the initial calculations yielded a theoretical UV power of 270 nW, as indicated in our paper.[41] For the most recent calculations of UV power, laser powers and focus waist diameters were updated. New values for the beam diameter and radius of curvature were calculated with the *Focus* module using a slightly larger focus waist of 20 μm. This was done to reflect the actual amount of power that was transmitted through the pinhole during alignment. The updated parameters are those listed in Table 4.1. The new calculations resulted in a predicted UV power of 288 nW.

Preliminary results from the initial construction and alignment of the system yielded a UV power of 40 nW, as discussed in our first paper.[41] The power was calculated using the sensitivity of the R166 PMT, given as 4×10^5 A/W (for 1000 V applied voltage).

After some investigation, two causes were found for the low UV power compared to the theoretical power. First, the initial measurements of the UV power were made after both the signal and reference beams were reflected with 45° mirrors coated at 226 nm. However, these mirrors were coated for s-polarization, and a significant amount of UV power was lost because the UV beam is p-polarized. Secondly, the BBO crystal was placed on a manual rotation stage at first, and the phase-matching angle could not be matched precisely enough to generate the theoretical UV power.

For subsequent experiments with the laser system, these two shortcomings were fixed, and the UV power generated in the BBO crystal increased significantly. The two mirrors were replaced with mirrors coated for p-polarized radiation incident at 45 °. The rotation stage under the BBO crystal was also replaced with the motorized rotation stage described in the previous chapter. Additionally, more time was spent adjusting the alignment and focus of the fundamental beams after some UV signal was generated. It was much easier to optimize the overlap of the two beams using the intensity as displayed on an oscilloscope as opposed to simply aligning the beams by eye through a pinhole. The improved components and alignment process resulted in a generated UV power of 280 nW. While this number agrees nicely with the theoretical power of 288 nW, there is a caveat on the uncertainty in the measured power. According to Hamamatsu, the uncertainty of the sensitivity values can range up to ±50%. This implies a measured power of 280 ± 140 nW. Nonetheless, the measurement still indicates that the UV power generated in the SFG process is on the same order of magnitude as the prediction, which is satisfactory given the potential variations in the crystal and beam properties.

For a generated UV power of 280 nW, the beam was attenuated by a factor of almost 2000 to prevent the PMTs from saturating. A combination of ND filters and the interference filters provided the necessary attenuation. Because of the UV power limit of the PMTs, usually very little effort was made to optimize the UV generation for the majority of the experiments. Fewer ND filters were used in those cases and excellent spectroscopic results were observed even for low UV powers.

4.2. Laboratory Gas Cell Measurements

Once the NO sensor was developed, tests were performed on a mixture of NO and N_2 in a room temperature gas cell in the laboratory. A variety of transitions in the (0,0) band of the $A^2\Sigma^+$ - $X^2\Pi$ electronic transition were probed at multiple subatmospheric pressures in the cell. The first transition probed was actually two overlapped transitions, $P_2(10)$ and $^PQ_{12}(10)$, at 44087.79 cm^{-1} and 44087.77 cm^{-1}, respectively.[11] For these lines, the ECDL was tuned to a wavelength of 395.237 nm (vacuum). The results from these first tests are shown in Figure 4.1 on the following page.

In Figure 4.1 and the remaining figures, Absorption 1 and Absorption 2 refer to the two halves of a single absorption scan, as explained in section 3.3. The best-fit theoretical curves shown in all figures were calculated using the LabView and FORTRAN code also discussed in that section. Known parameters input to the code were the path length (0.30 m for the gas cell) and temperature (298 K). Fitting was done by manually varying the concentration and collision-broadening coefficient (2γ in equation 2.10) until the theoretical absorption spectrum fit well visually with the experimental spectra. The pressure was initially input as the value from the transducer, but it was often varied slightly around this value to optimize the fit. Best-fit values for the NO concentration, collision-broadening coefficient, and pressure are indicated in all figures along with the measured values.

Returning to Figure 4.1, we see that the resulting fit between experimental and theoretical lineshapes is excellent for both conditions. This indicates that the sensor is fully resolving the absorption line and that our theoretical code is correctly calculating the lineshape. The concentrations that produced the best fits were 91 ppm and 89 ppm for 100 torr and 50 torr, respectively. The nominal concentration of the gas bottle used in all gas cell experiments was 100 ppm with an uncertainty of ±10%. For the sensor, the uncertainty in the concentration measurements is estimated at ±10 ppm for the gas cell measurements. This uncertainty is indicative of the variations in concentration observed over all of the gas cell results, as will be explained later. For the present

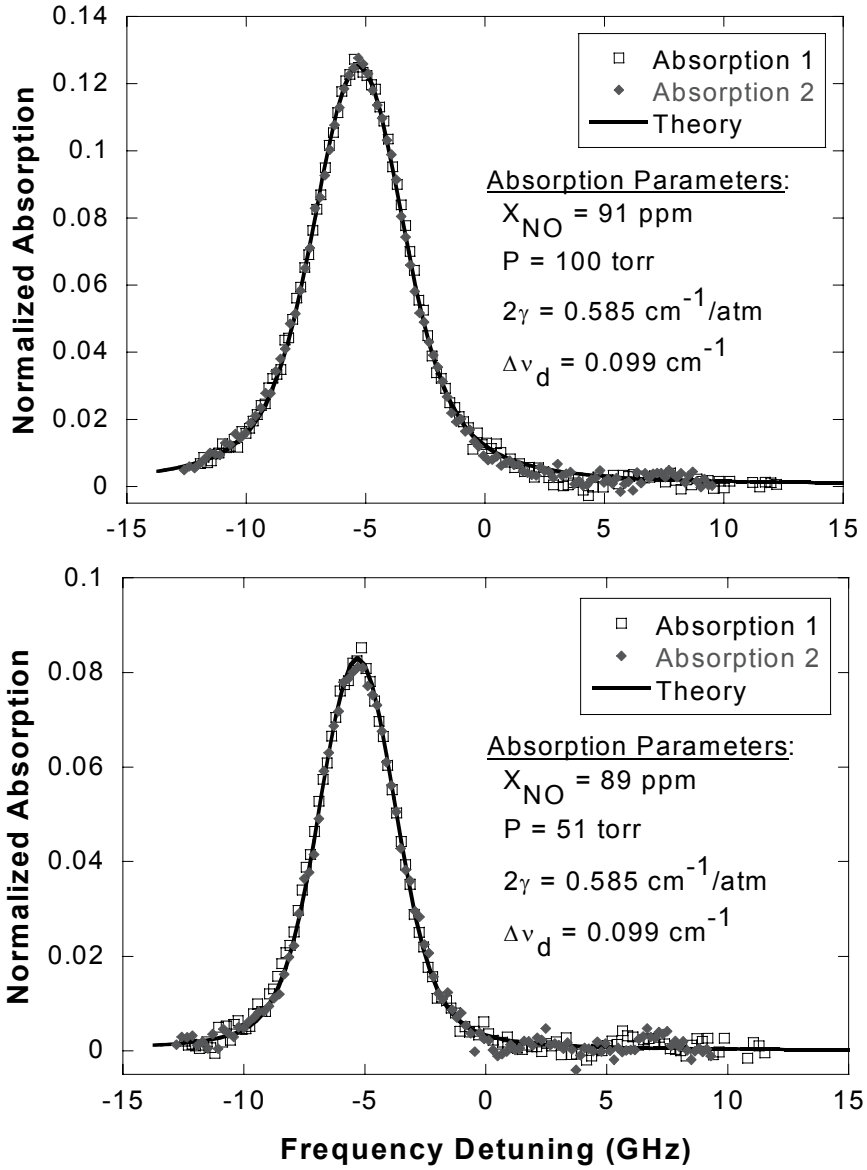

Fig. 4.1. Comparison of measured and calculated absorption line shapes for $P_2(10)$ and $^PQ_{12}(10)$ overlapped transitions measured in the gas cell at pressures of 100 torr (top) and 50 torr (bottom). The theoretical parameters used in the absorption code are indicated.

results, the absorption measurements of 89±10 ppm and 91±10 ppm certainly agree well with the actual concentration of the mixture, 100±10 ppm.

Values for the pressure used in the theoretical absorption calculations also agree well with the values obtained from the pressure transducer. For pressure transducer measurements of 100 torr (top panel of Figure 4.1) and 50 torr (bottom panel), the best-fit parameters for pressure were 100 torr and 51 torr. The pressure transducer used in the experiments has an uncertainty of ±0.25% of full scale, or ±2 torr. Therefore, both pressure measurements agree well within the uncertainty.

Finally, the last parameter from the fitting routine is the collision-broadening coefficient, 2γ. As mentioned in Chapter 2, two groups have studied this band of NO previously and have determined values for the collision-broadening coefficient for the transitions studied in this research. Chang et al.[13] reported a value of 0.583±0.03 cm^{-1}/atm (FWHM) for NO broadened by N_2, while Danehy et al.[14] reported a value of 0.586±0.04 cm^{-1}/atm for identical conditions. From Figure 4.1, the value for 2γ is 0.585 cm^{-1}/atm, in almost perfect agreement with both of the previously reported values. This again confirms the resolution of the sensor and the accuracy of the theoretical code.

After fully resolving a single transition in the gas cell, the sensor was tuned to probe a group of closely spaced transitions near 226.87 nm. The identifiable structure in these transitions provided an independent verification of the wavelength readings of both lasers. Initially, the ECDL was tuned to a center wavelength of 395.390 nm to probe two sets of overlapped transitions: the $P_2(2)$ and $^{P}Q_{12}(2)$ transitions at 44078.08 cm^{-1} and the $P_2(5)$ and $^{P}Q_{12}(5)$ transitions at 44077.71 and 44077.70 cm^{-1}, respectively. Results from scans of three different cell pressures are given in Figures 4.2 and 4.3.

In Figures 4.2 and 4.3, we again see the excellent fit between theoretical and experimental absorption line shapes, even for the multiple lines probed in the scan. Concentrations of NO determined from the best-fit routine are consistently low for the three tests shown in the figures. In the top panel if Figure 4.2, the concentration of 80±10 ppm is not likely to be within the 100±10 ppm concentration of the bottle. The low concentration measurement could possibly be due to uncertainties in the parameters from the spectral database, but it certainly needs more investigation to draw such a conclusion. The bottom panel of Figure 4.2 and Figure 4.3, however, are in closer

agreement with absorption measurements of 85±10ppm for both tests. The resulting pressure measurements, despite being consistently low, agree within the ±2 torr uncertainty of the transducer measurements. Also, the collision-broadening coefficient remained 0.585 cm^{-1}/atm, in excellent agreement with the literature.

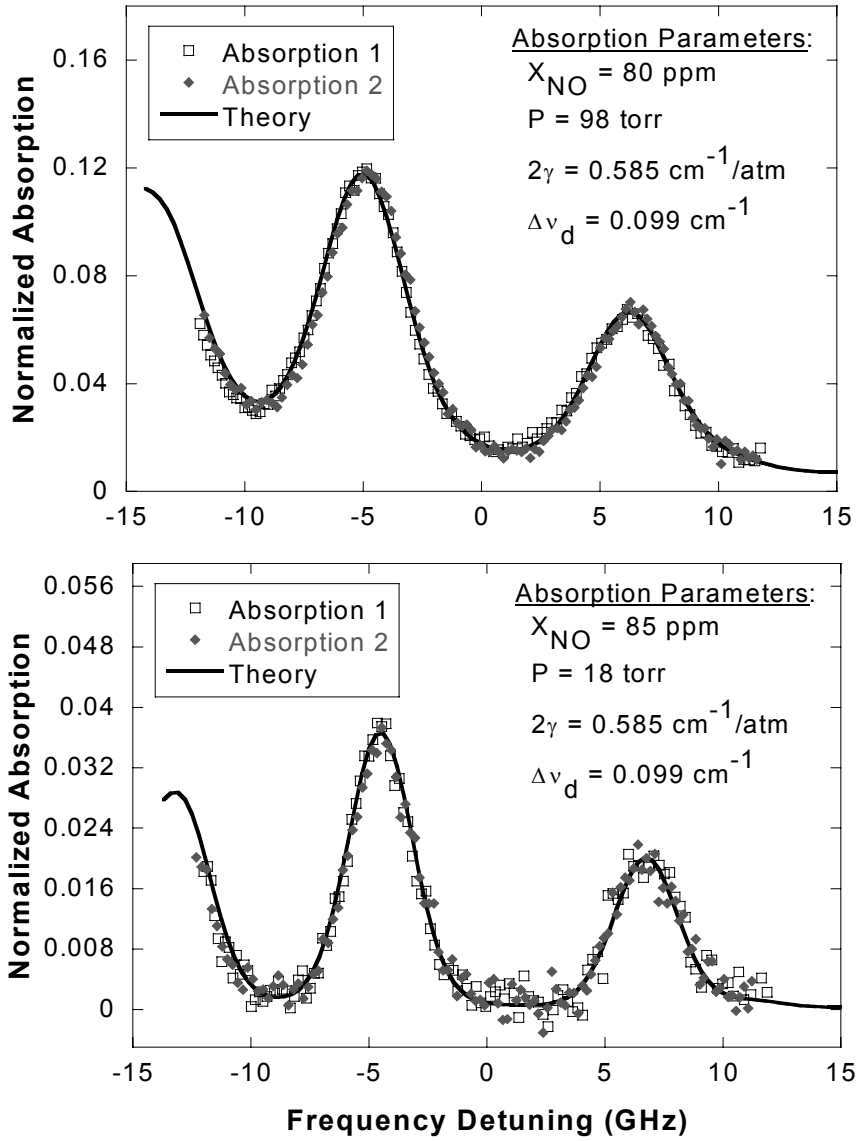

Fig. 4.2. Comparison of measured and calculated absorption line shapes for three overlapped transitions measured in the gas cell at pressures of 100 torr (top) and 20 torr (bottom). The transitions shown are (from left to right) are the overlapped $P_2(5)$ and $^PQ_{12}(5)$ transitions and the overlapped $P_2(2)$ and $^PQ_{12}(2)$ transitions.

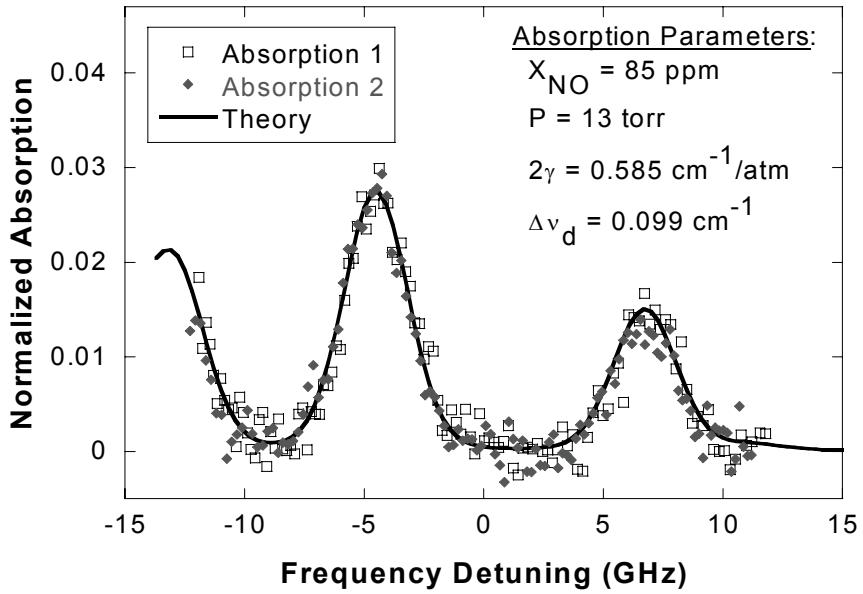

Fig. 4.3. Comparison of measured and calculated absorption line shapes for the transitions shown in Fig. 4.2 for a gas cell pressure of 15 torr.

The final experiments with the gas cell were performed on transitions immediately adjacent to those in Figures 4.2 and 4.3. The ECDL was tuned to a center wavelength of 395.398 nm to address three sets of overlapped transitions: the $P_2(3)$ and $^PQ_{12}(3)$ transitions at 44077.72 cm^{-1}, the $P_2(4)$ and $^PQ_{12}(4)$ transitions at 44077.30 cm^{-1}, and the $P_2(5)$ and $^PQ_{12}(5)$ transitions at 44077.71 and 44077.70 cm^{-1}, respectively. The resulting absorption scans are shown in Figures 4.4 and 4.5 for three different pressures.

As in the previous figures, the theoretical and experimental lineshapes in Figures 4.4 and 4.5 are in excellent agreement. With the extremely narrow linewidth of the UV radiation, the sensor was even capable of resolving the closely spaced lines shown at –9 and –5 GHz frequency detuning. The concentrations are again within good agreement of the bottle concentration, especially the lower pressure scans shown in the bottom panel of Figure 4.4 and Figure 4.5. Pressure measurements by the sensor gave lower values than those measured by the transducer for Figure 4.4, similar to the results from Figures 4.2 and 4.3. In Figure 4.5, the best-fit pressure is higher than the transducer. All three

values are within the uncertainty of the pressure transducer, though. Also, the value for the collision-broadening coefficient remained the same as the previous figures.

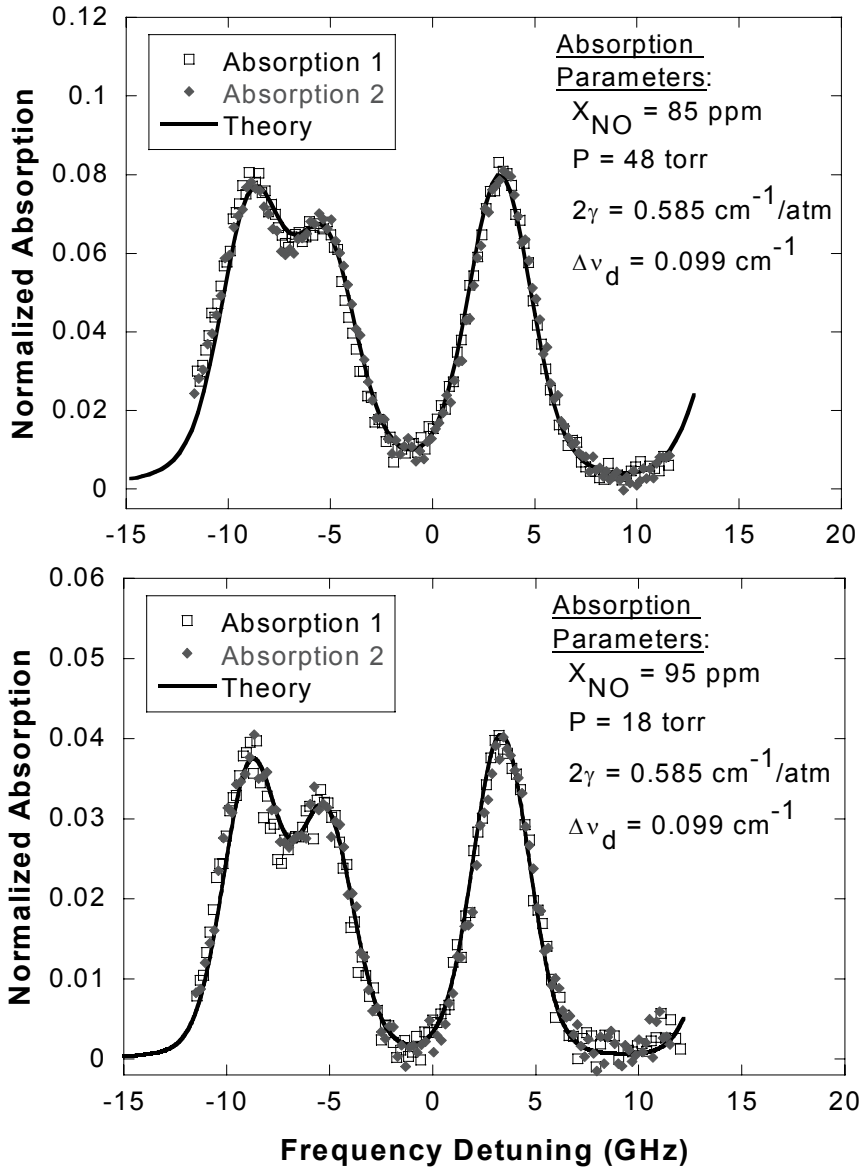

Fig. 4.4. Comparison of measured and calculated absorption line shapes for three overlapped transitions measured in the gas cell at pressures of 50 torr (top) and 20 torr (bottom). The transitions shown are (from left to right) are $P_2(4)$ and $^{P}Q_{12}(4)$, $P_2(3)$ and $^{P}Q_{12}(3)$, and $P_2(5)$ and $^{P}Q_{12}(5)$. Actual conditions and theoretical parameters are indicated.

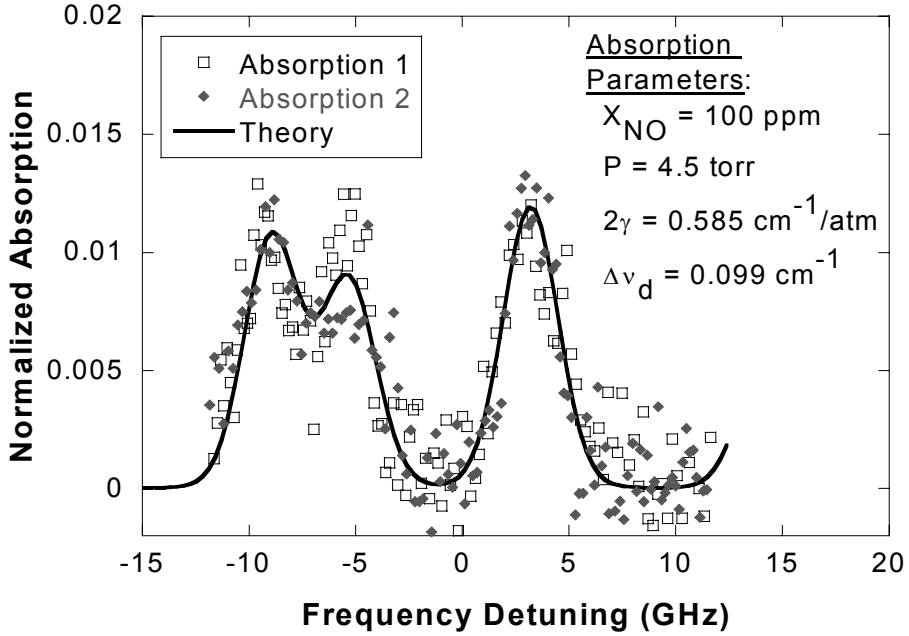

Fig. 4.5. Comparison of measured and calculated absorption line shapes for the transitions shown in Fig. 4.4 for a gas cell pressure of 3 torr.

In Figure 4.5, the extremely low pressure in the gas cell highlights the noise present in the scans. At such low pressures, very few NO molecules are present in the cell and very little UV radiation is absorbed. Indeed, only around 1% is absorbed in the 3 torr sample shown in Figure 4.5. Comparing two subsequent air scans (processed in the same way as absorption scans) revealed that the baseline noise has a rms standard deviation of 0.17%. The shot noise limit (the theoretical lowest noise level) for this configuration of the detection system is calculated to be 0.09% (see Appendix B). Hence, the observed noise in the measurements is only a factor of 2 greater than the shot noise limit. Although we are still limited by electronic noise in the detection channel, the detection limit is approaching the shot noise limit. Therefore, the sensitivity of the sensor is limited by the detection channel. Assuming a signal to noise (S/N) ratio of 1 at the detection limit, an absorption of 0.17% corresponds to a sensitivity of about 0.2 ppm of NO for a 1-m path length of gas at 300 K. In higher temperatures (typical of combustion exhaust), this detection limit is slightly worse at 0.5 ppm-m in 1000 K gas.

This estimated detection limit was confirmed empirically with extremely low-pressure absorption scans in the gas cell.

The results from all of the gas cell experiments reported here are summarized in Table 4.2 for comparison. The variation in concentration measurements in the gas cell experiments is evident in the table. Measured values range from 80 to 100 ppm over all of the pressures and lines tested. From the variation in these and other gas cell results, the overall sensitivity is estimated to be ±10% for these preliminary experiments. In all results, though, the measurements are within the uncertainty of the actual concentration of the gas mixture, which was 100±10 ppm.

The uncertainty observed in the sensor measurements comes from a variety of potential sources. First, the path length through the gas cell cannot be measured exactly and is known only to within approximately ± 5 mm. Second, the composition of the gas in the cell was not guaranteed to be solely the NO/N_2 mixture from the bottle despite careful efforts to completely purge the cell with the mixture. Some air could have remained in the cell after taking the air scans, thus diluting the mixture and lowering the actual concentration closer to the values observed with the sensor. Third, the parameters from the spectroscopic database could be in error. As mentioned earlier, this possibility must be investigated in more detail before drawing any conclusions, and we plan to carry out this investigation in the future. Fourth, the response of the PMTs could contribute to

Table 4.2. Summary of measured concentrations and pressures for gas cell experiments at room temperature (298 K). Actual concentration of NO in the bottle is 100 ppm (nominal).

	Pressure (torr)		Absorption Concentration
Fig.	Transducer	Absorption	(ppm)
4.1 (top)	100	100	91
4.1 (bottom)	50	51	89
4.2 (top)	100	98	80
4.2 (bottom)	20	18	85
4.3	15	13	85
4.4 (top)	50	48	85
4.4 (bottom)	20	18	95
4.5	3	4.5	100

the uncertainty in the measurements if the PMT response in nonlinear due to saturation. A detailed investigation of the PMT response and the saturation behavior of the PMT response is planned. Finally, the concentration measurements by the sensor depend on the assumption of an infinitely narrow laser linewidth in the calculations. The excellent agreement between theoretical and experimental line shapes indicates that this is a good assumption.

Elaborating on the laser linewidth, we estimate that the UV beam has a linewidth of approximately 80 MHz, which is the convolution of the two laser source linewidths. For the absorption linewidth, the Doppler-limited case has a linewidth equal to the Doppler width of 0.099 cm^{-1} or 2.97 GHz. Hence, the UV radiation linewidth is a factor of 37 narrower than the least broadened absorption line would have. This is not an infinitely narrow laser linewidth but is unlikely to introduce significant error in the sensor measurements.

Overall, the gas cell experimental results were quite encouraging. The performance of the laser system throughout was quite adequate to make fully resolved spectroscopic measurements of NO. It was also sufficiently tunable to address almost any transition within the (0,0) band that we are investigating. Resulting detection limits for the gas cell measurements were also reasonable for direct absorption measurements. Altogether, the initial laboratory experiments in the room-temperature gas cell provided the necessary knowledge and assurance to continue the testing of the laser in a field environment.

4.3. Field Demonstrations

With the excellent results from the experiments in the controlled laboratory environment, the next step in the sensor development was to test it in more realistic combustion environments. Two facilities were chosen for the field tests: a gas turbine auxiliary power unit (APU) at Honeywell Engines and Systems in Phoenix, Arizona and a well-stirred reactor (WSR) at Wright-Patterson Air Force Base in Dayton, Ohio. The results from each test will be discussed individually.

The theoretical curves for the results of the field tests were found in almost the same manner as for the gas cell experiments. In the field demonstrations, all measurements were made in open exhaust tubes, so the pressure was input as atmospheric pressure (101 kPa) for all calculations. The path length (see section 3.5) and pressure were input to the code and held fixed during the fitting procedure. As described previously, the NO concentration and collisional-broadening coefficient were varied manually until the experimental and theoretical absorption spectra matched visually. Thermocouple readings of the temperatures were used as a starting point for the temperature in the theoretical code, but variations around the measured values were required to optimize the fit. The resulting theoretical absorption lines and parameters are indicated in the remaining figures for each field demonstration. The values for 2γ in all figures are given at 298 K.

For both of the field tests, the sensor was tuned to probe the isolated transition initially probed in the gas cell experiments. This was actually two overlapped transitions, $P_2(10)$ and $^{P}Q_{12}(10)$, at 44087.79 cm^{-1} and 44087.77 cm^{-1}, respectively. This line was chosen because it was sufficiently isolated from other lines to resolve the peak and part of the baseline in the same scan, even in the highly broadened atmospheric pressure conditions. The line is also fairly insensitive to temperature so that its strength did not decrease significantly even at the high temperatures of the combustion exhaust.

4.3.1. Well-Stirred Reactor Results

The first field demonstration experiments were performed on the well-stirred reactor (WSR) facility at Wright-Patterson Air Force Base in Dayton, Ohio. For our experiments, ethylene fuel was used and the WSR was run at a variety of equivalence ratios to produce NO levels from 1 to 140 ppm. Due to temperature limits in the reactor, the highest equivalence ratio was around Φ=0.75, which produced over 100 ppm of NO. Concentrations of NO dropped sharply as the reactor was run leaner until only 1 or 2 ppm was produced at equivalence ratios close to lean blowout (Φ=0.4). To confirm the operation of the sensor after transportation and realignment, the reactor was run at low

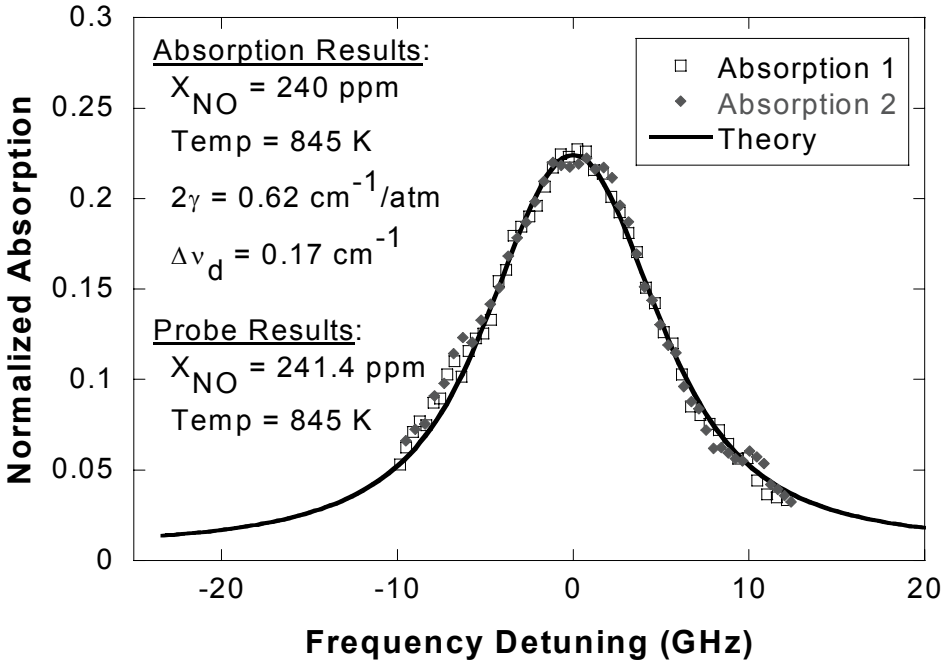

Fig. 4.6. Comparison of measured and calculated absorption line shapes for initial WSR experiments with Φ=0.4 and 3000 ppm seeded into the reactor.

temperatures (Φ=0.4) and seeded with 3000 ppm of NO in N_2. Levels of around 240 ppm were present in the exhaust of the flame, producing a very clear absorption feature. The resulting absorption spectrum is shown in Figure 4.6. Processing the absorption scan confirmed the accuracy of the sensor, as seen by the close agreement between experiment in theory in Figure 4.6.

After positively identifying NO in the exhaust stream, the seeding gas was removed and the WSR was run at a high equivalence ratio to detect NO generated during the combustion. At an equivalence ratio of Φ=0.75, around 90 ppm of NO was produced in the reactor. The resulting absorption scan is shown in Figure 4.7. Other scans were recorded as the equivalence ratio was dropped to measure lower levels of NO. One such scan is shown in Figure 4.8 for Φ=0.698, where around 50 ppm of NO was produced.

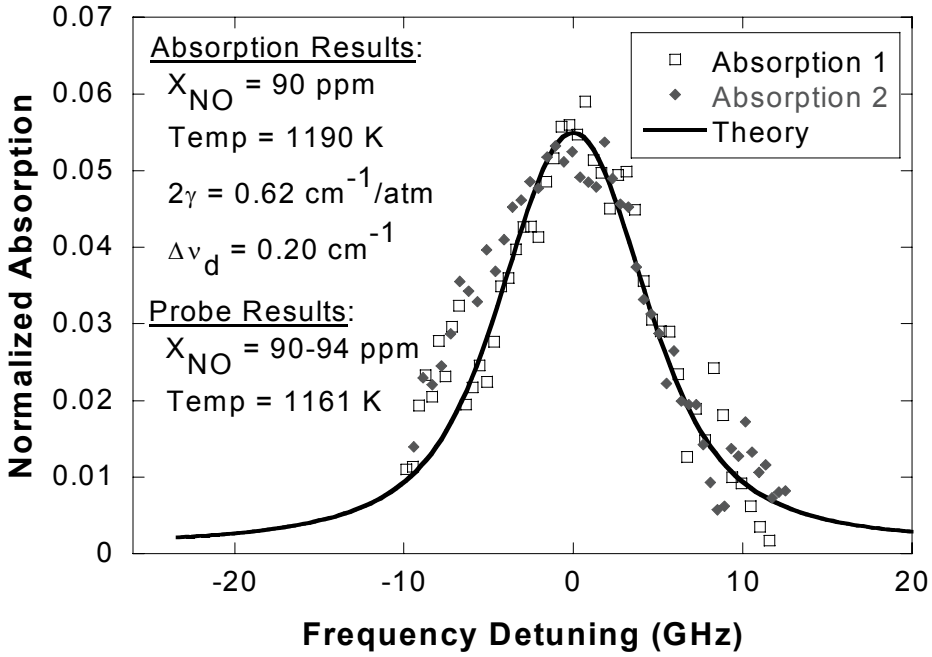

Fig. 4.7. Comparison of measured and calculated absorption line shapes for initial WSR experiments with Φ=0.75.

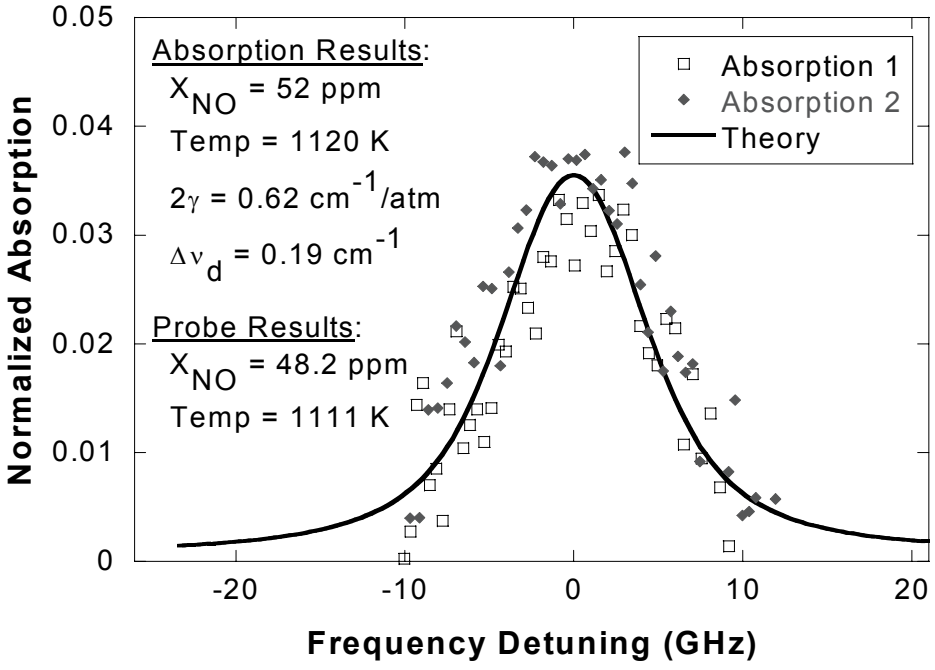

Fig. 4.8. Comparison of measured and calculated absorption line shapes for initial WSR experiments with Φ=0.698.

In Figures 4.6 through 4.8, the theoretical and experimental lineshapes agree closely. Clearly, the fit is extremely good for the large absorption in Figure 4.6. As the NO levels drop, the absorption levels drop as well, and the noise becomes more apparent, observed in Figures 4.7 and 4.8. Still, the general lineshapes fit reasonably well. Concentration values for all three conditions match extremely closely with those measured by the chemiluminescent analyzer. In Figure 4.7, the range of concentrations measured by the probe indicates the fluctuation during the course of the absorption scans. The best-fit value of 90 ppm coincides exactly with the low end of the range and deviates only 4% from the high end of the range. The uncertainty in the probe measurements is 3.6% for the WSR analyzer (see section 3.5), so the deviation is likely due to uncertainty in the probe measurements. The worst agreement in all three of the figures occurs in Figure 4.8 where the absorption measurement is 8% higher than the probe measurement. Assuming for the moment an uncertainty of ±10% for the sensor, then this value is well within the experimental uncertainty. The ±10% uncertainty in the sensor measurements will be justified later in this section.

Comparisons between temperature measurements in the WSR results must be made with some caution. First, the temperature measurements were made at only one location in the exhaust stream. With the wide variation in temperature across the stream, it is not certain exactly what temperature (e.g. centerline, etc.) is being measured. Second, the thermocouple readings were not corrected for radiation because of the small thermocouple size. The actual temperature of the gas, though, is higher than the values recorded by the thermocouple due to radiation losses to the surroundings. Third, the temperature measurement from the sensor represents the path-averaged temperature of the gas, so it will lie between the centerline temperature and the ambient temperature. With such uncertainties in the actual exhaust temperature, the thermocouple readings only serve as ballpark values to use in the curve-fitting routine and give some validity to the resulting temperature. Mindful of this, we see that the absorption temperature measurements are all within 30 K of the thermocouple readings, which is quite reasonable given the temperatures and conditions of the reactor.

The last parameter from the fitting routine, the collision-broadening coefficient, also requires some explanation. The resulting value, $2\gamma = 0.62$ cm^{-1}/atm, is consistent in all three figures. This value is higher than the values mentioned earlier by Chang et al.[13] and Danehy et al.[14] of 0.583 ± 0.03 cm^{-1}/atm and 0.586 ± 0.04 cm^{-1}/atm, respectively, for NO broadened by N_2. Despite the large percentage of N_2 in air, other molecules are present in the combustion exhaust that will affect the broadening, such as oxygen (O_2), carbon monoxide (CO), carbon dioxide (CO_2), and water vapor (H_2O). DiRosa and Hanson have investigated the collision broadening of the (0,0) band of NO by O_2 and H_2O and found values for 2γ of 0.53 cm^{-1}/atm and 0.79 cm^{-1}/atm, respectively, at 295 K.[42, 43] In typical combustion close to stoichiometric equivalence ratios, water vapor concentrations will be much higher than oxygen concentrations. Consequently, NO broadening will be more affected by water vapor, which has a larger collision-broadening coefficient than pure N_2. Thus we see that the value of 0.62 cm^{-1}/atm from the best-fit routine is a reasonable value for NO broadened by both N_2 and H_2O.

Although there is good agreement between measured values, substantially more noise is present in the absorption spectra than in the gas cell measurements. Several factors explain the increase in noise. Obviously, we expect some increase in noise simply due to the change in environment from the laboratory to the field. Vibrations from the pumps, exhaust fans, and other equipment required to run the WSR caused vibrations in the lasers and optics. The increased temperatures near the reactor also affected the operation of the sensor slightly. With the equipment running but no flame, the effect of these vibrations and temperature were observed and recorded. Indeed, slightly more noise was present, slightly over 0.2% compared to 0.17% in the laboratory, but it was satisfactory given the operating environment.

Once the WSR was ignited, however, the noise increased substantially. This noise was due to beam steering by the hot exhaust gases and the 6-pass arrangement used for these experiments. Changes in index of refraction in the gas due to different density regions cause the UV beam to deviate along its path through the hot gases. The motion of the beam is magnified by the multi-pass setup, which increases the path length of the

beam through the gases. This beam steering introduces noise in two ways. First, with the 6-pass arrangement through the flame, several reflections are required on each mirror, and some of the beams lie close to the edges of these mirrors. Any motion in the beam could clip the beam on one of these mirror edges or on the edge of the PMT face and cause a fluctuation in UV intensity. Second, the signal from the PMT could vary even if the beam was not clipped before entering the detector. Since the sensitivity of the PMT varies with location on the detector area, the motion of the beam from the hot exhaust causes a random fluctuation in the absorption signal. The situation is aggravated further by the lens in front of the signal PMT, which substantially reduced the size of the beam striking the face of the PMT. In both scenarios, the effect of beam steering is quite pronounced and is believed to be the major contributor to the increase in noise from the gas cell experiments.

Another set of experiments was performed on the WSR several months after the initial experiments to attempt to decrease this noise. The goal was to measure NO levels in the flame that were close to the detection limit of the sensor. Improvements were made in the experimental setup to reduce vibrations transmitted to the sensor and to reduce the possible effects of beam steering (e.g. fewer passes, reflections closer to the center of the mirrors). Unfortunately, the ECDL operated so poorly that very few meaningful results came out of these experiments. Figure 4.9 shows the results from an absorption scan for Φ=0.75. Due to improvements since the first experiments in the WSR, temperatures inside the reactor were hotter than before, producing higher levels of NO. Therefore, the same equivalence ratio produced NO concentrations of 140 ppm in this set of experiments.

The results from the second set of experiments are very similar to the initial results in the WSR. In Figure 4.9, the noise is quite reduced from the original experiments in the WSR, and the theoretical and experimental lineshapes agree well. Absorption values for the concentration are 10 ppm, or 7%, lower than those measured by the probe. With a probe uncertainty of 3.6% and an estimated sensor uncertainty of ±10%, the results are well within experimental uncertainty. Temperature measurements with the sensor also

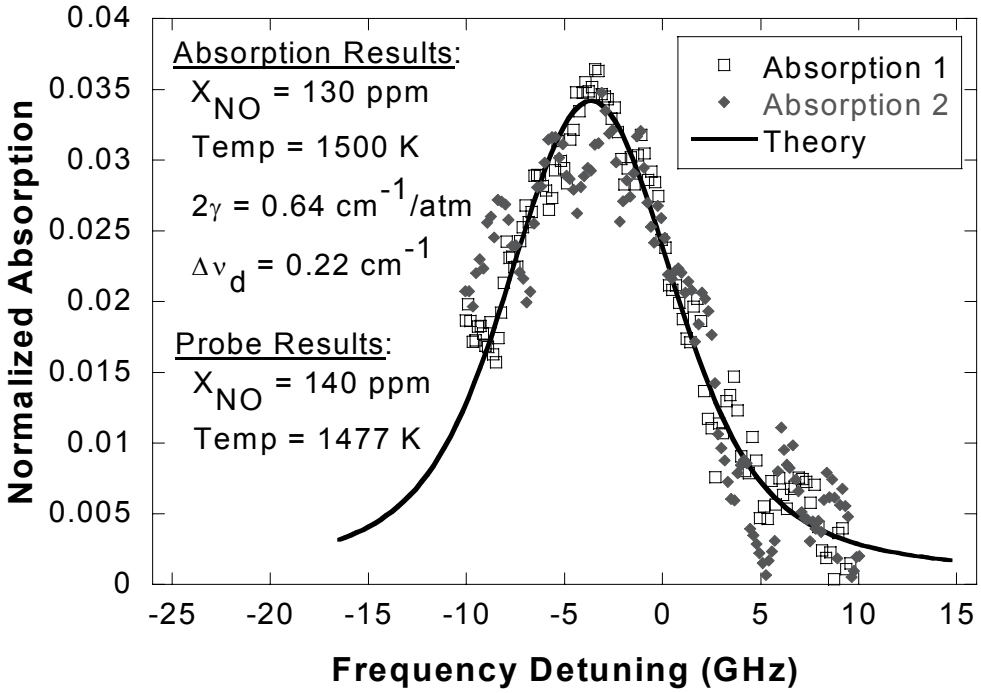

Fig. 4.9. Comparison of measured and calculated absorption line shapes for later WSR experiments with Φ=0.75.

agree within 23 K of the thermocouple readings, which is reasonable given the uncertainty in thermocouple readings described previously. The collision-broadening coefficient was found to be 0.64 cm^{-1}/atm, which is slightly higher but still consistent with previous results.

While the results in Figure 4.9 indicate that the noise was successfully reduced from the previous WSR experiments, the noise is still significantly higher than expected. The majority of this noise can be attributed to the poor operation of the ECDL during the experiments. In fact, examining only the first half of the scan, Absorption 1, the noise is significantly reduced. This is shown more clearly in Figure 4.10. Mode-hops in the ECDL occurred during the second half of the scan and contributed to the noise visible in Absorption 2. The other source of noise in the experiments was due to beam steering by

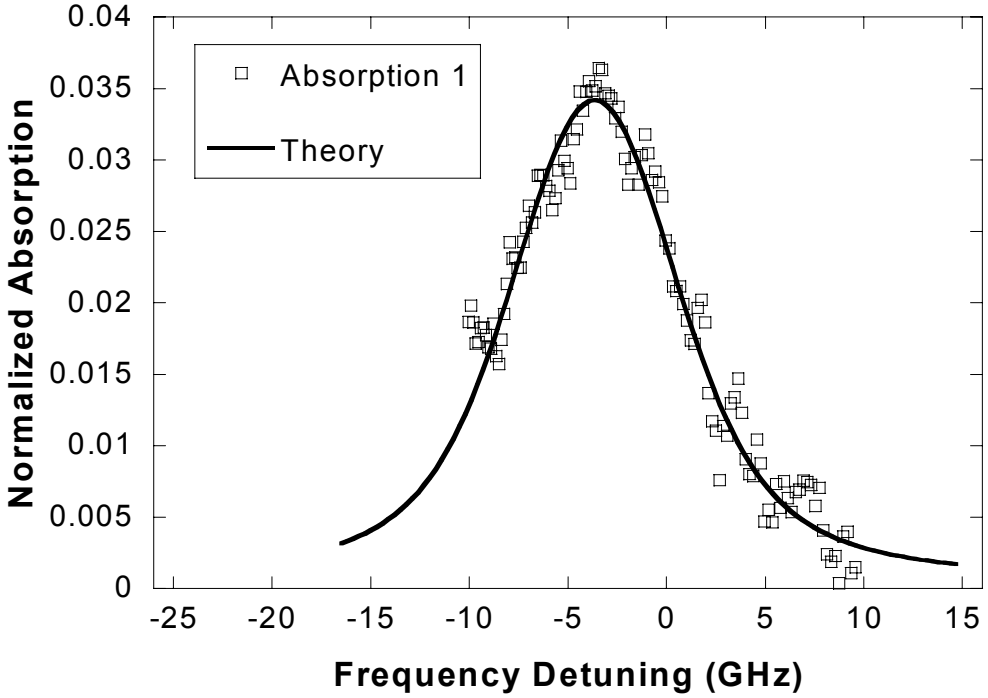

Fig. 4.10. Measured and calculated absorption line shapes from Fig. 4.9 showing only the first half of the scan to demonstrate the multi-mode behavior of the second half of the scan.

the hot exhaust gases, as explained earlier. This PMT signal fluctuation is believed to cause the majority of the noise not attributed to the ECDL operation.

Despite the noise present in both WSR tests, the overall results from these experiments were very good. As seen in Figure 4.10, as little as 3% absorption was clearly observed in the tests. Few of the groups reviewed in section 2.2 performed *in situ* measurements of NO in flames with their diode-laser-based sensors. With this sensor, relatively low levels of NO were measured in the flame even with direct absorption. The satisfactory results in the adverse environment of the WSR indicated that the sensor was ready for the extremely harsh environment of a gas turbine.

4.3.2. Gas Turbine APU Results

After good results at the WSR facility, subsequent field tests were performed on a gas turbine APU engine at Honeywell Engines and Systems in Phoenix, Arizona. The

sensor was operated remotely from outside of the test cell because of the extremely loud operation of the APU. The noise and vibrations were due to the huge volume of air flowing through the turbine operating at 48,000 rpm. Inside the test cell, the temperature was hot and the vibrations were very severe. These extreme conditions made the tests difficult to prepare and conduct, especially with the delicate nature of the optical system. Nonetheless, the results from this field demonstration were very encouraging.

For these tests, the APU was run on JP-8 fuel at a variety of load conditions. Loads were applied to the engine in two ways. First, a load could be applied to the generator by applying a resistance across the leads of the generator, thus producing electrical power. Second, air could be bled from the compressor stage of the turbine. The fuel flow to the APU is actively controlled so that the speed of the turbine remains constant. Therefore, whenever a load is applied to the APU, the fuel flow increases, raising the temperature in the combustion chamber and producing more NO. Both loads could be applied at once, creating the fully loaded condition. Figure 4.11 shows the first results

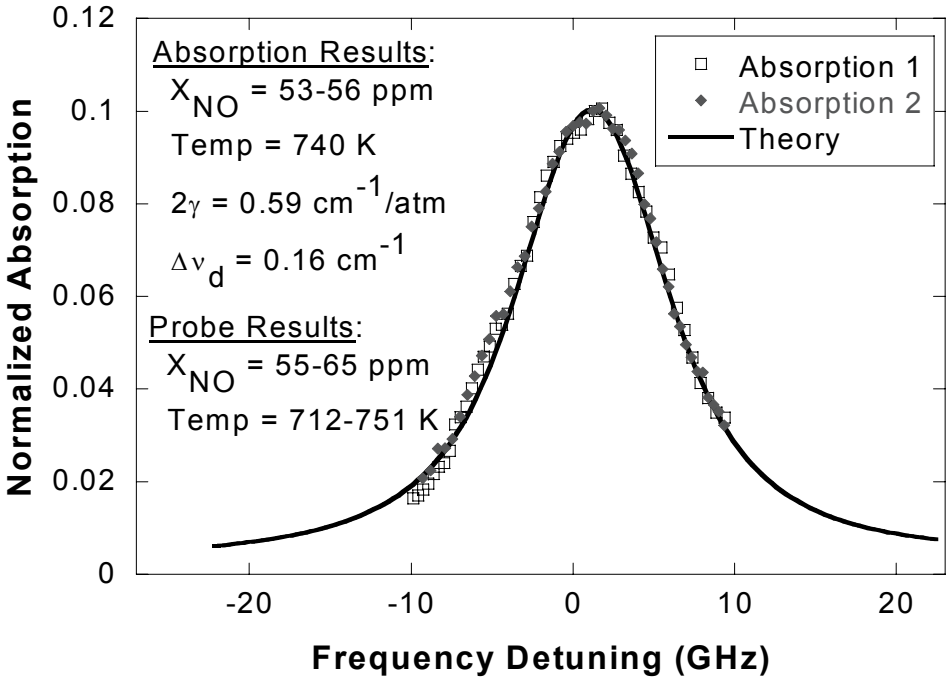

Fig. 4.11. Comparison of measured and calculated absorption line shapes for measurements on the APU running at full load.

from a full load condition where around 60 ppm of NO was produced. Decreasing one or both of the applied loads resulted in lower NO levels from the engine, and three such conditions were tested. Finally, the lowest levels of NO were measured at the idle condition without any applied load. The significant results from each of these conditions will now be discussed.

The results from a full load condition are shown in Figure 4.11. With very little noise in the scan, the close agreement between theoretical and experimental lineshapes is clear. Before comparing the concentrations, one note is required. The NO concentration in Figure 4.11 does not reflect the actual measured concentration. In this particular scan, instead of using an air scan to normalize the data according to equation 3.1, a scan from an idle condition was used. This was done because the air scans for that particular run were invalid. Since there was NO present in the idle condition scan, the best-fit value for Figure 4.11 is 49 ppm, which is lower than the actual concentration by the amount of NO present in the idle scan. From later measurements, the idle condition typically produced 4 to 7 ppm of NO, so the actual concentration of NO shown in Figure 4.11 is the sum of these two concentrations: 53 to 56 ppm. Unfortunately, for this particular scan the probe-sampling apparatus was not yet set up, so the actual concentration was not measured. However, later measurements of the same load condition indicated NO levels from 55 to 65 ppm, as shown in Figure 4.11. Therefore, the absorption and probe measurements of NO agree to within experimental uncertainty (±1% for the probe, ±10% for the sensor).

Another comment is required before comparison of the temperatures in Figure 4.11 and the remaining figures. Unlike the WSR experiments, multiple thermocouples were used to measure the temperature variation across the exhaust tube of the APU. The range of temperatures in all of the figures indicates this radial variation. These values were not corrected for radiation either, but they were small thermocouples and the temperature was relatively low so the radiation loss will be small. They were also located on the end of the hot exhaust tube so that only half of each thermocouple was exposed to the cooler surroundings, resulting in lower radiation losses as well. In this

context, the thermocouple measurements play the same role as in the WSR: to provide an initial guess for the best-fit routine and to provide a range for the final answer. The resulting temperatures measured by the sensor are the path-averaged values and are expected to be within the range of thermocouple measurements. Indeed, Figure 4.11 reflects this agreement.

For the collision-broadening coefficients in Figure 4.11 and all of the APU results, we expect the values to lie between those from the gas cell experiments and those from the WSR experiments. The water vapor will again broaden NO more effectively than N_2, so the collision-broadening should be larger than the gas cell measurements of 0.585 cm^{-1}/atm. It should be similar to and possibly smaller than the WSR value because of the greater volume of oxygen present in the exhaust, which broadens NO less than N_2, slightly reducing the broadening coefficient. The value of $2\gamma = 0.59$ cm^{-1}/atm in Figure 4.11 does in fact agree with these expectations.

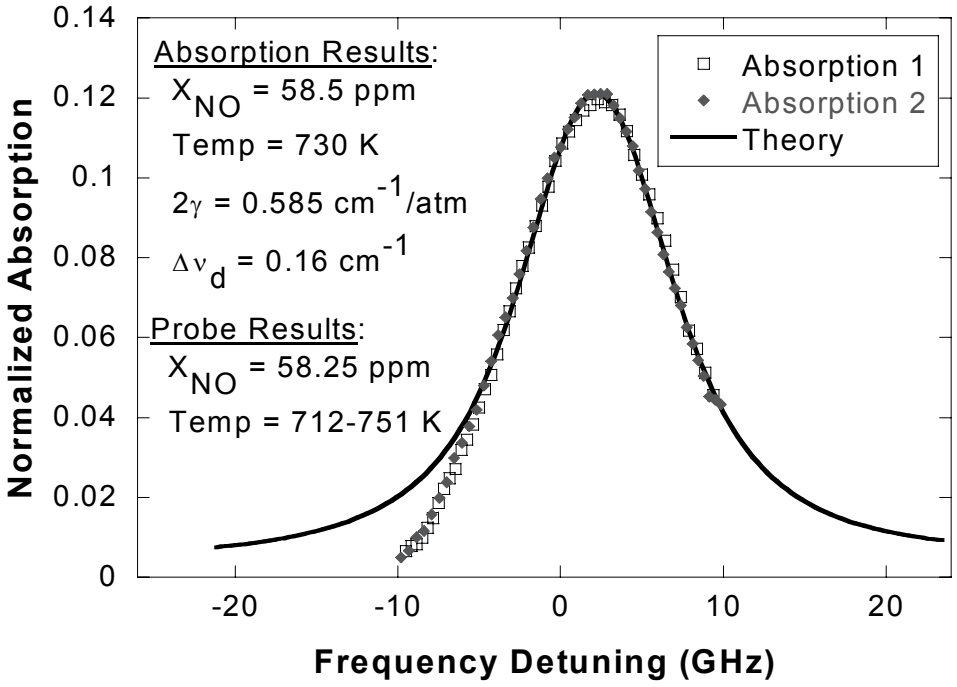

Fig. 4.12. Comparison of measured and calculated absorption line shapes for a second full load test on the APU.

Another scan at the full load condition is given in Figure 4.12. Here, the agreement between theoretical and experimental lineshapes is good over most of the scan. However, the theoretical and experimental curves deviate on the left edge of the scan. The cause for this is assumed to be in the normalizing air scans. The NO concentration measured in this scan agrees very closely to the probe sampling measurement. The remaining parameters also agree closely, as explained for Figure 4.11.

Lower load conditions are shown in Figures 4.13 and 4.14. In both figures, the agreement of the lineshapes and all parameters is excellent. The <3% difference in concentration measurements is especially noteworthy. The value of $2\gamma = 0.64$ cm^{-1}/atm in Figure 4.13 is slightly higher than previous values but still within a reasonable range.

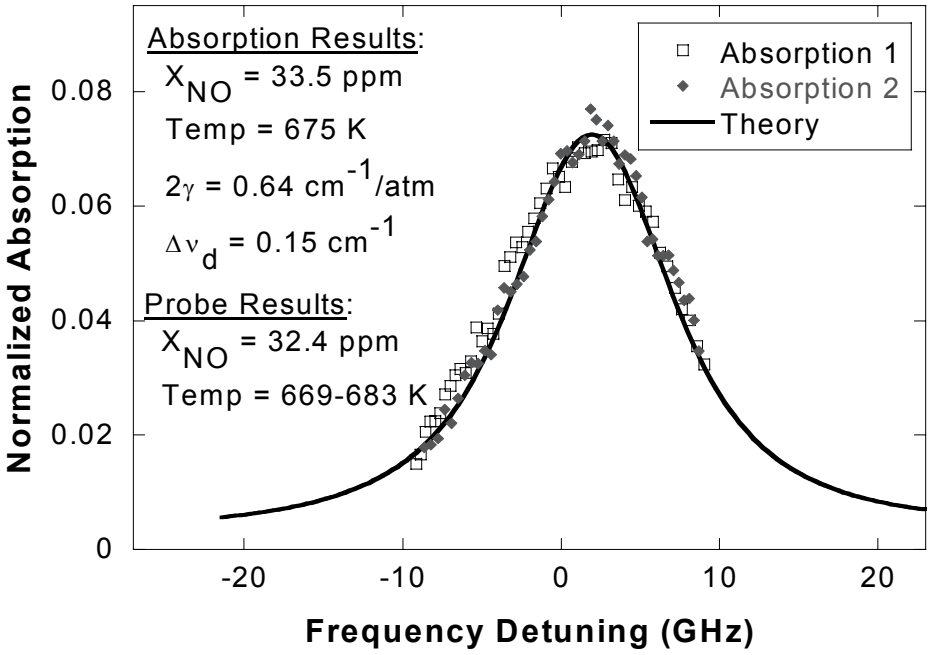

Fig. 4.13. Comparison of measured and calculated absorption line shapes for measurements on the APU running at roughly a half load condition.

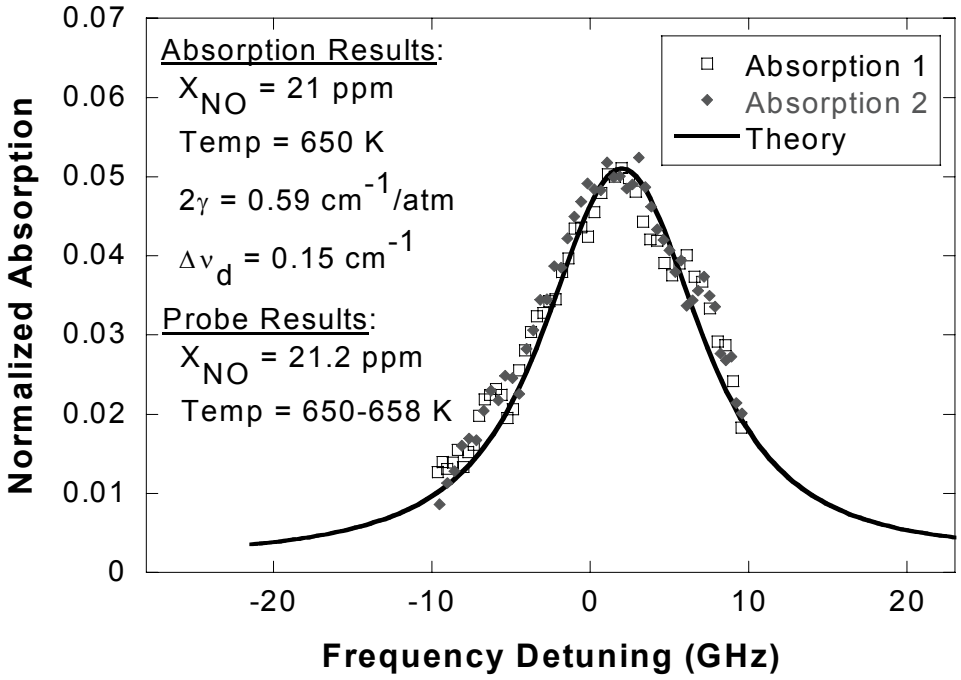

Fig. 4.14. Comparison of measured and calculated absorption line shapes for measurements on the APU running at roughly a third of full load.

Results from a near idle condition are shown in Figure 4.15. While the lineshapes, temperatures, and broadening-coefficients agree well with expectations, the concentrations differ by almost a factor of 2. These anomalous results are believed to be caused by errors in the probe. Error in the sensor measurements could be attributed to drift in the PMTs during the course of the experiment. On multiple instances, the signal PMT voltage was observed to drift. Since air scans were usually taken before starting the APU and then again after stopping it, the PMTs could drift quite significantly between the NO scan and the air scan. This resulted in invalid results, usually, with no recognizable absorption spectrum visible in the normalized data. In this case, however, the lineshapes and all other parameters agree well. This suggests that the error lies in the probe measurements. Previously, Zabielski et al. demonstrated that probe and optical measurement of NO in the UV region differed up to 25%.[44] Curiously, their measurements on a Pratt & Whitney burner running at an aircraft idle condition

indicated that water-cooled probe measurements of NO were only 80 – 90% of the concentrations measured optically.

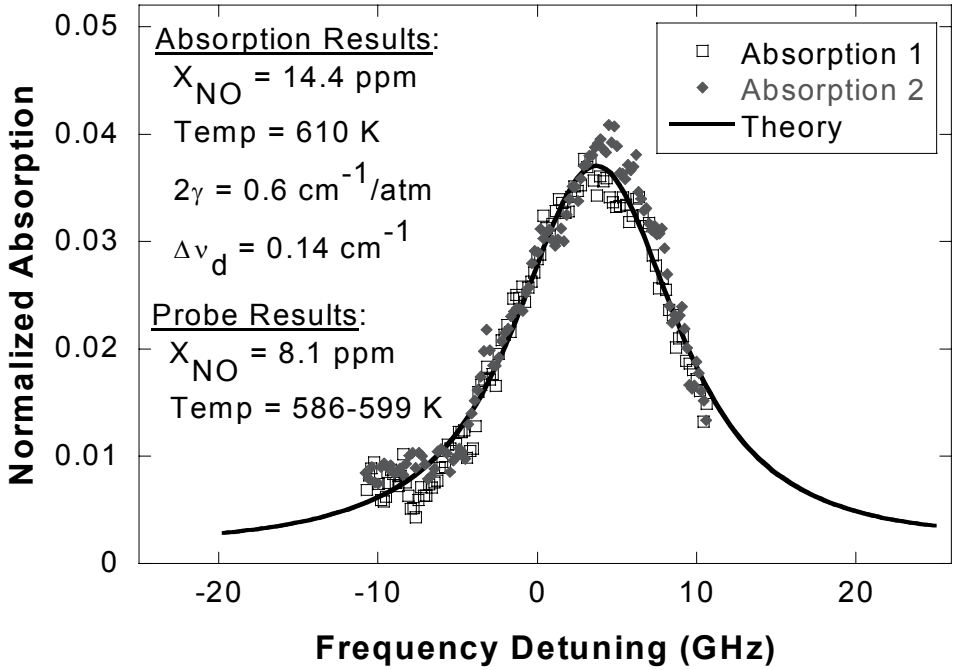

Fig. 4.15. Comparison of measured and calculated absorption line shapes for measurements on the APU running at a near idle condition.

Finally, results from the idle condition are shown in Figures 4.16 and 4.17. In these last two figures, the results were less than satisfactory. The low amount of absorption in the scans led to a significant increase in the signal to noise (S/N) ratio and the fits became worse than the previous results. In Figure 4.16, the fit between the theoretical and experimental lineshapes is poorer than previous fits. There is also a huge discrepancy in the collision-broadening coefficient when compared to the expected value. This would also suggest that the lineshapes do not match, since the low value for 2γ indicates that the line is much narrower than expected. The most likely cause for the deviant results is the drift in the PMTs in the time between the air scans and the idle scan. The higher S/N ratio also played some role in the anomaly.

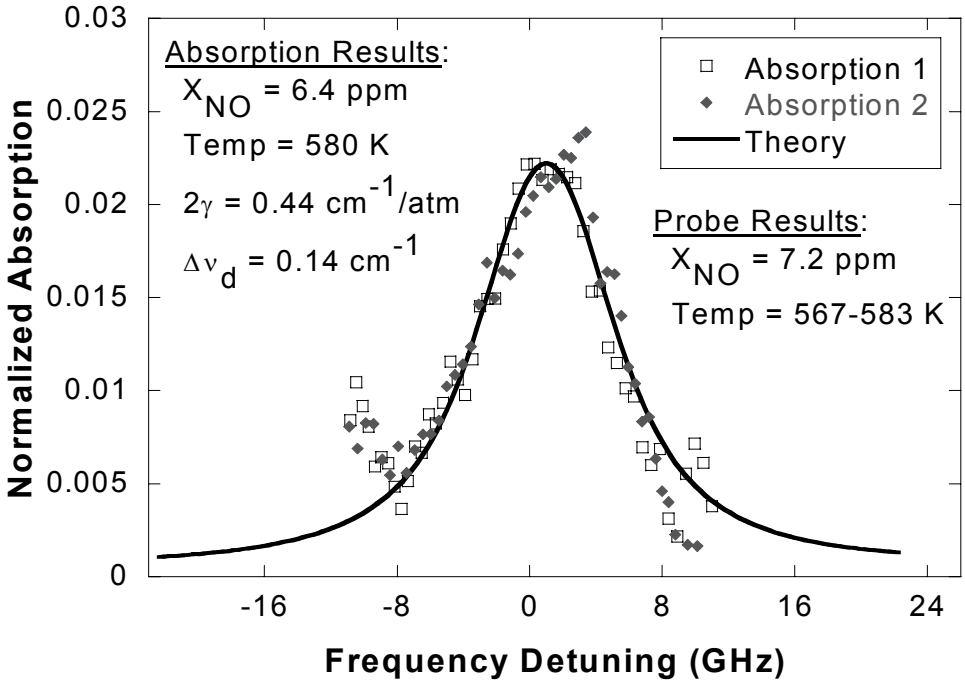

Fig. 4.16. Comparison of measured and calculated absorption line shapes for measurements on the APU running at an idle condition.

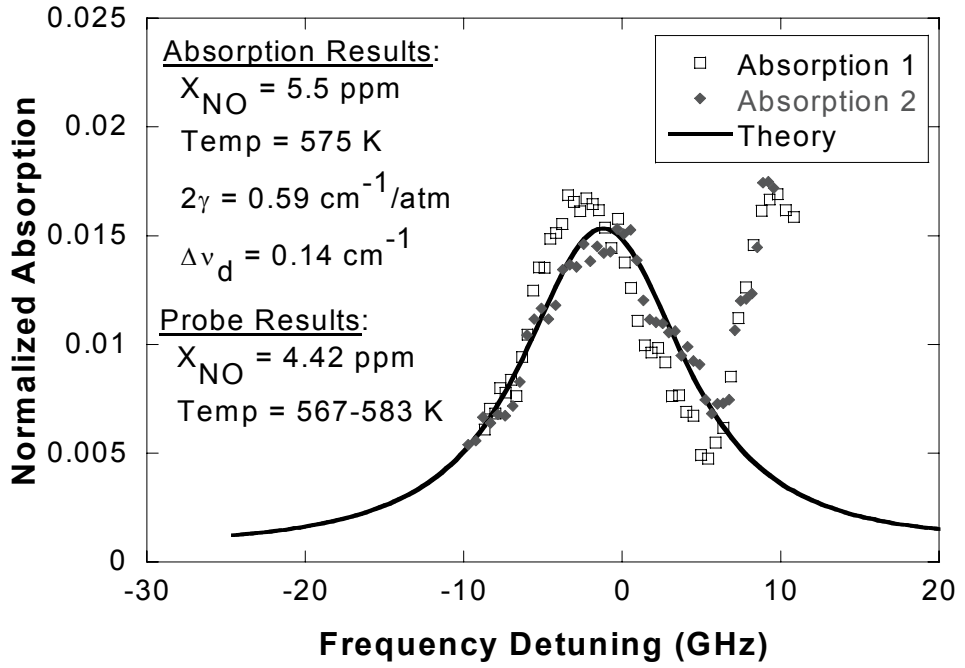

Fig. 4.17. Comparison of measured and calculated absorption line shapes for a second test of the APU running at idle condition.

The results from all of the field demonstrations are summarized in Table 4.3. The overall agreement between all of the parameters affirms the accuracy of the sensor. Favorable comparisons of parameters (i.e. collision-broadening coefficients and lineshapes) with the literature provides an external confirmation of the sensor operation as well. Additionally, these results confirm previous studies showing the close agreement between optical and probe concentration measurements of NO.[44]

After analyzing the noise in all of the field demonstration results, a slightly higher value was observed than in the gas cell results. The rms standard deviation of the noise was found in the same method as for the gas cell, and a value of 0.23% was calculated. This slight increase in noise is excellent in light of the huge increase in the noise of the environment. Calculating the shot noise again for these experiments (see Appendix B), the shot noise limit is 0.15%, indicating that the increase in observed noise was not entirely due to the change in the operating environment. An increase in the UV power and a change in the processing routine (binning 20 channels instead of 50 channels) contributed to the increase in noise in the detection system, as seen in the increase in shot noise limit. In fact, the noise actually improved from the gas cell tests since observed noise in the system is only a factor of 1.5 higher than the shot noise limit as

Table 4.3. Summary of measurements from WSR and APU field demonstrations. All measurements were made at atmospheric pressure (101 kPa). Collisional widths are given at 298 K.

	Temperature (K)		Concentration (ppm)		Width (FWHM) (cm^{-1})	
Fig	Thermocouple	Absorption	Probe	Absorption	Collisional	Doppler
4.6	845	845	241.4	240	0.62	0.17
4.7	1161	1190	90-94	90	0.62	0.20
4.8	1111	1120	48.2	52	0.62	0.19
4.9	1477	1500	140	130	0.64	0.22
4.11	712-751	740	55-65	53-56	0.59	0.16
4.12	712-751	730	58.25	58.5	0.585	0.16
4.13	669-683	675	32.4	33.5	0.64	0.15
4.14	650-658	650	21.2	21	0.59	0.15
4.15	586-599	610	8.1	14.4	0.6	0.14
4.16	567-583	580	7.2	6.4	0.44	0.14
4.17	567-583	575	4.42	5.5	0.59	0.14

opposed to a factor of 2 higher in the gas cell experiments. Nonetheless, the increase in noise did decrease the sensitivity of the sensor slightly. For an absorption of 0.23%, the resulting detection limit for the sensor is 0.8 ppm for a 1 meter path length in 1000 K gas (assuming a S/N ratio of 1 at the detection limit). For 300 K gas, this corresponds to 0.3 ppm of NO for a 1 meter path length.

The uncertainty in the concentration measurement made by the sensor can also be deduced from the results of all the tests. For the gas cell experiments, an uncertainty of ±10 ppm (or 10%) was estimated for the concentration measurements. In the field demonstrations, the difference in probe and absorption measurements varied widely, but in general the differences were never greater than 10%. Therefore, the overall uncertainty in the sensor concentration measurements is estimated at ± 10%. This value is identical to that obtained by a more rigorous uncertainty analysis performed by Webber for CO_2.[45] Sources for the experimental uncertainty in the field demonstrations are the same as in the gas cell experiments. However, the uncertainty in the path length is much greater since the medium of interest is not well confined as in the gas cell experiments. An error of up to ± 4 cm is possible in the path length since the multi-pass arrangements magnify the uncertainty.

Returning again to the uncertainty in the infinitely narrow laser linewidth, it is clear that the assumption is much more accurate for NO spectroscopy at atmospheric pressures. The large pressure broadening coefficients for NO in various gases results in absorption linewidths on the order of 20 GHz. The estimated UV linewidth of 80 MHz is narrower by a factor of 250, indicating that the infinitely narrow linewidth is certainly stronger for the tests at atmospheric pressures.

The overall performance of the sensor in the field demonstrations was very good even in the harsh environments surrounding the combustors. Absorption line shapes were fully-resolved for a variety of combustion operating points, and NO concentration and temperature measurements with the sensor agreed very well with the probe and thermocouple measurements. All of these results are very promising for the future development of this sensor.

5. CONCLUSIONS AND RECOMMENDATIONS

The development of a diode-laser-based sensor for measuring nitric oxide (NO) is described in this thesis. The sensor is based on the absorption of ultraviolet (UV) radiation by the NO molecule. UV radiation at 226.8 nm is produced via sum-frequency generation (SFG) by mixing 532-nm and 395-nm radiation in a BBO crystal. The tunable UV radiation was used to probe several transitions in the (0,0) band of the $A^2\Sigma^+$-$X^2\Pi$ electronic transition of NO. Three separate experiments were performed to test the operation of the sensor in a variety of environments. These experiments were used to demonstrate the feasibility of this type of sensor and to prove that it can potentially be used in real combustion environments to replace existing NO sensor technology.

5.1. Summary of Results

In the development and application of this new sensor, there were three main objectives outlined in the first chapter. The first was to design and assemble a laser system to produce sufficient UV radiation to perform spectroscopic measurements of NO. Second, the laser system had to be used to make spectroscopic measurements of NO in a controlled laboratory environment to verify the sensor operation and to validate the theoretical calculations. Finally, the sensor had to be demonstrated in a realistic combustion environment to prove its feasibility as a commercial NO sensor. Consistent with these objectives, the results are summarized below:

1. The laser system was successfully designed and constructed to produce around 280 ± 140 nW of UV radiation at 226.8 nm in the SFG process. The resulting power was nominally very close to the theoretical power of 288 nW calculated for the conditions of the laser system.
2. Initial measurements of NO were successfully demonstrated in a room-temperature gas cell in the laboratory. A variety of transitions were probed at

multiple sub-atmospheric pressures in the cell producing fully-resolved absorption spectra. NO concentration and pressure measurements with the sensor all agreed very well with the bottle concentration and pressure transducer measurements. Collisional linewidths of the resulting absorption spectra agreed exactly with previous measurements by others. The resulting detection limit in the gas cell experiments was found to be 0.2 ppm-m (parts per million over a 1 meter path length) in 300 K gas (assuming a S/N ratio of 1 at the detection limit). In 1000 K gas, this detection limit corresponds to 0.6 ppm-m of NO. Uncertainty in the concentration measurements was estimated at ±10%.

3. Subsequent experiments were successfully carried out in two actual combustion environments to demonstrate the operation of the sensor in the field. Measurements were made on a well-stirred reactor (WSR) facility at Wright-Patterson Air Force Base in Dayton, Ohio and a gas turbine auxiliary power unit (APU) at Honeywell Engines and Systems in Phoenix, Arizona. Both experiments produced excellent results despite the extreme vibrations and temperatures around the combustion equipment. Concentrations and temperatures measured by the sensor were verified at each facility by probe-sampling chemiluminescent analyzers and thermocouples. Collisional linewidths also agreed with expected values from the literature. For the field tests, a slightly higher detection limit of 0.8 ppm-m for 1000 K gas was demonstrated. This corresponds to 0.3 ppm-m in 300 K gas. The overall uncertainty was again estimated to be ± 10%.

The overall success of these experiments convincingly proves the feasibility of the sensor described in this thesis. More than just a laboratory tool, this sensor was demonstrated to work accurately even in the harsh environment of actual combustion equipment. With continued progress in this research, this diode-laser-based sensor will soon replace the traditional NO sensor technology and provide a powerful tool for combustion control.

5.2. Future Work

To continue the development of this sensor, there are many possible avenues to be pursued. Some of these options are easily implemented and will be done in the near future. Other developments in the sensor are more involved and will not be implemented for some time.

5.2.1. Near Term Work

In the near future, one modification will be made to the sensor and further tests will be performed in different environments. We are currently planning on adding a small gas cell filled with a low-pressure NO mixture in the reference beam of the sensor. The reference cell will provide several benefits to improve the operation and accuracy of the sensor. In measurements on atmospheric pressure NO, the absorption lines are very broad and hard to distinguish in the raw data while running the sensor. The reference cell will provide a frequency reference to ensure that we are in fact scanning over an absorption line. Furthermore, the reference cell will eliminate the need for taking air scans. Since the concentration and pressure of the reference cell will be known, then the absorption through the cell will be known exactly and can be compensated for when used as the reference scan. Data processing procedures for analyzing the absorption data will be modified to take into account the presence of the NO cell in the reference channel.

With this modification, tests are planned to measure the NO concentration in coal exhaust. These measurements will be made in collaboration with Dr. Kalyan Annamalai in his 30-kW co-fired boiler burner facility at Texas A&M University (described in Annamalai et al.[46]). The facility was modified with reburn capability and a premixed propane burner to simulate realistic coal combustion conditions. Ammonia will be injected into the fuel stream to simulate the NO production in coal-fired power plants. Our sensor will be used to quantify the NO reduction as a result of the reburn process. These tests will also determine the effect of particulate loading on the sensor measurements. Demonstration of the sensor in a particle-laden exhaust stream such as

this will open up new applications for this sensor in coal-fired power plants and other industrial combustion facilities.

5.2.2. Long Term Improvements

For long term improvements in the sensor, the suggestions presented here address three key limitations of the current configuration of the sensor. Increasing the tuning range of the sensor and lowering the detection limit are the main two concerns. However, for potential combustion control applications, the data acquisition and processing time must also be improved significantly. Improvements for these limitations are the following:

1. A newly available 395-nm ECDL produced by Sacher Laser will replace the existing ECDL made by Toptica. The new laser reports a mode-hop-free tuning range of 100 GHz, over 4 times as large as the current ECDL. The large increase in tuning range will allowe multiple transitions to be probed in one scan, resulting in a more accurate fit of the parameters. It also allows measurements at higher pressures where the lines become extremely broad. Both of these advantages will improve the sensor dramatically. However, external computer control of the diode current and grating piezoelectric voltage will be required to achieve the enhanced tuning range.
2. Another option to increase the tuning range of the sensor is electro-optic modulation of the ECDL. The current configuration of ECDLs employs a piezoelectric crystal to physically move the diffraction grating and tune the wavelength. This severely limits the speed at which the laser can be tuned, and it also increases the susceptibility to vibrations. If the diffraction grating were fixed and an electro-optic crystal were used to change the angle of the beam striking the grating, then no moving parts are required. This has been demonstrated before, and the range and rate of tuning is only limited by the voltage applied to the electro-optic crystal.[47] Thus, the sensor could be tuned over extremely wide ranges at a rapid rate, significantly increasing the accuracy and sensitivity of the sensor.

3. Wavelength modulation spectroscopy (WMS) is another important tool that must be implemented to achieve ultra low detection limits by the sensor. WMS employs high tuning rates (kHz or greater) and phase-sensitive detection of the second harmonic to achieve absorption levels of 10^{-5} or lower (reference Silver).[48] Many groups have demonstrated the power of this technique in previous sensors.[21, 27, 28, 33]
4. Replacing the photomultiplier tubes (PMTs) with a different type of detector, avalanche photodiodes (APDs), is another means of increasing the sensitivity of the sensor. PMTs are capable of single photon measurements and are therefore extremely sensitive. Typically for this sensor, the UV is attenuated by a factor of 2000 to prevent the saturation of the PMTs. This means that only 0.05% of the generated UV is detected in the measurements. With APDs, more of the UV could be used in the measurements and greater sensitivity could be obtained with the sensor.
5. Much work needs to be done with the computer software and the data acquisition system to reduce the overall acquisition and processing time of the sensor. No effort was made to optimize either the collection or the processing routines and both pieces of software can be streamlined to improve the efficiency. Further analysis of the spectroscopic equations might yield a more efficient means of calculating the theoretical absorption so that the fitting routines will run faster. Also, fewer points can be sampled on the oscilloscope to speed up data transfer during the experiment. These efforts are necessary in order for this sensor to be a useful tool in combustion diagnostics and control.

With continued improvements of this sensor, it can become an indispensable tool for NO emissions measurements and combustion diagnostics. The potential use of this sensor in combustion control certainly warrants continued research and development in the future.

REFERENCES

1. U.S. EPA Office of Air Quality Planning and Standards, "National Air Pollutant Emission Trends, 1900-1998," Report EPA-454/R-00-002, U. S. Environmental Protection Agency, Research Triangle Park, NC (2000).
2. J. Colls, *Air Pollution, 2nd Ed.* (Spon Press, New York, 2002).
3. Editors, "Editorial", NO **1**, 1 (1997).
4. N. Irving Sax and R. J. Lewis, Sr., *Dangerous Properties of Industrial Materials: Volume III, 7th Ed.*, (Van Nostrand Reinhold, New York, 1989).
5. N. Docquier and S. Candel, "Combustion control and sensors: a review," Progress in Energy and Combustion Science **28**, 107-150 (2002).
6. Vaught Engineering Inc., "Low-NOx Measurement: Gas Turbine Plants. Final Report on Review of Current Measuring and Monitoring Practices," Report CRTD Vol. 52, ASME International, Center for Research and Technology Development, Washington, DC (1999).
7. M. G. Allen, "Diode laser absorption sensors for gas-dynamic and combustion flows," Meas. Sci. Technol. **9**, 545-562 (1998).
8. E. R. Furlong, R. M. Mihalcea, M. E. Webber, D. S. Baer, and R. K. Hanson, "Diode-laser sensors for real time control of pulsed combustion systems," AIAA J. 37, 732-737 (1999).
9. R. P. Lucht, R. C. Peterson, and N. M. Laurendeau, "Fundamentals of Absorption Spectroscopy for Selected Diatomic Flame Radicals," Report PURDU-CL-78-06, School of Mechanical Engineering, Purdue University, West Lafayette, IN (1978).
10. G. Herzberg, *Molecular Spectra and Molecular Structure: I. Spectra of Diatomic Molecules, 2nd Ed.* (D. Van Nostrand Company, Inc., Princeton, NJ, 1950).
11. J. Luque and D. R. Crosley, "LIFBASE: Database and Spectral Simulation Program (Version 1.5)," SRI International Report MP 99-009 (1999).
12. A. C. Eckbreth, *Laser Diagnostics for Combustion Temperature and Species* (Gordon and Breach Publishers, Amsterdam, The Netherlands, 1996).
13. A. Y. Chang, M. D. DiRosa, and R. K. Hanson, "Temperature dependence of collision broadening and shift in the NO A $\leftarrow$ X (0,0) band in the presence of argon and nitrogen," J. Quant. Spectrosc. Radiat. Transfer **47**, 375-390 (1992).
14. P. M. Danehy, E. J. Friedmann-Hill, R. P. Lucht, R. L. Farrow, "The effects of collisional quenching on degenerate four-wave mixing," Appl. Phys. B **57**, 243-248 (1993).

15. J. R. Reisel, C. D. Carter, and N. M. Laurendeau, "Einstein coefficients for rotational lines of the (0,0) band of the NO $A^2\Sigma^+$ - $X^2\Pi$ system," J. Quant. Spectrosc. Radiat. Transfer **47**, 43-54 (1992).

16. R. Freedman and R. W. Nicholls, "Molecular constants for the v"=0 ($X^2\Pi$) and v'=0,1 ($A^2\Sigma^+$) levels of the NO molecule and its isotopes," J. Molec. Spectrosc. **83**, 223-227 (1980).

17. F. P. Incropera, *Introduction to Molecular Structure and Thermodynamics* (John Wiley & Sons, New York, 1974).

18. W. J. Kessler, D. M. Sonnenfroh, B. L. Upschulte, and M. G. Allen, "Near-IR diode lasers for *in-situ* measurements of combustor and aeroengine emissions," paper AIAA 97-2706, presented at the 33rd AIAA/ASME/SAE/ASEE Joint Propulsion Conference, Seattle, WA, 6-9 July 1997.

19. D. M. Sonnenfroh and M. G. Allen, "Absorption measurements of the second overtone band of NO in ambient and combustion gases with a 1.8-μm room-temperature diode laser," Appl. Opt. **36**, 7970-7977 (1997).

20. R. M. Mihalcea, D. S. Baer, and R. K. Hanson, "A diode-laser absorption sensor system for combustion emission measurements," Meas. Sci. Technol. **9**, 327-338 (1998).

21. D. B. Oh and A. C. Stanton, "Measurement of nitric oxide with an antimonide diode laser," Appl. Opt. **36**, 3295-3297 (1997).

22. D. D. Nelson, M. S. Zahniser, J. B. McManus, C. E. Kolb, and J. L. Jimenez, "A tunable diode laser system for the remote sensing of on-road vehicle emission," Appl. Phys. B **67**, 433-441 (1998).

23. L. Menzel, A. A. Kosterev, R. F. Curl, F. K. Tittel, C. Gmachl, F. Capasso, D. L. Sivco, J. N. Baillargeon, A. L. Hutchinson, A. Y. Cho, and W. Urban, "Spectroscopic detection of biological NO with a quantum cascade laser," Appl. Phys. B **72**, 859-863 (2001).

24. D. M. Sonnenfroh, W. T. Rawlins, M. G. Allen, C. Gmachl, F. Capasso, A. L. Hutchinson, D. L. Sivco, J. N. Baillargeon, and A. Y. Cho, "Application of balanced detection to absorption measurements of trace gases with room-temperature quasi-cw quantum-cascade lasers," Appl. Opt. **40**, 812-820 (2001).

25. A. A. Kosterev, A. L. Molinovsky, F. K. Tittel, C. Gmachl, F. Capasso, D. L. Sivco, J. N. Baillargeon, A. L. Hutchinson, and A. Y. Cho, "Cavity ringdown spectroscopic detection of nitric oxide with a continuous-wave quantum-cascade laser," Appl. Opt. **40**, 5522-5529 (2001).

26. S. Wehe, M. Allen, X. Liu, J. Jeffries, and R. Hanson, "NO and CO absorption measurements with a mid-IR quantum cascade laser for engine exhaust application," paper AIAA 2003-0588, presented at the 41st Aerospace Sciences Meeting and Exhibit, Reno, NV, 6-9 January 2003.

27. G. Hancock, V. L. Kasyutich, and G. A. D. Ritchie, "Wavelength-modulation spectroscopy using a frequency-doubled current-modulated diode laser," Appl. Phys. B **74**, 569-575 (2002).

28. K. A. Peterson and D. B. Oh, "High-sensitivity detection of CH radicals in flames by use of a diode-laser-based near-ultraviolet light source," Opt. Lett. **24**, 667-669 (1999).

29. H. R. Barry, B. Bakowski, L. Corner, T. Freegarde, O. T. W. Hawkins, G. Hancock, R. M. J. Jacobs, R. Peverall, and G. A. D. Ritchie, "OH detection by absorption of frequency-doubled diode laser radiation at 308 nm," Chem. Phys. Lett. **319**, 125-130 (2000).

30. G. J. Ray, T. N. Anderson, J. A. Caton, R. P. Lucht, and T. Walther, "OH sensor based on ultraviolet, continuous-wave absorption spectroscopy utilizing a frequency-quadrupled, fiber-amplified external-cavity diode laser," Opt. Lett. **26**, 1870-1872 (2001).

31. J. P. Koplow, D. A. V. Kliner, and L. Goldberg, "Development of a narrow-band, tunable, frequency-quadrupled diode laser for UV absorption spectroscopy," Appl. Opt. **37**, 3954-3960 (1998).

32. L. Corner, J. S. Gibb, G. Hancock, A. Hutchinson, V. L. Kasyutich, R. Peverall, and G. A. D. Ritchie, "Sum frequency generation at 309 nm using a violet and a near-IR DFB laser for detection of OH," Appl. Phys. B **74**, 441-444 (2002).

33. D. B. Oh, "Diode-laser-based sum-frequency generation of tunable wavelength-modulated UV light for OH radical detection," Opt. Lett. **20**, 100-102 (1995).

34. J. Alnis, U. Gustafsson, G. Somesfalean, and S. Svanberg, "Sum-frequency generation with a blue diode laser for mercury spectroscopy at 254 nm," Appl. Phys. Lett. **76**, 1234-1236 (2000).

35. R. W. Boyd, *Nonlinear Optics* (Academic Press, San Diego, 1992).

36. T. Walther, "Applied optics and photonics lecture notes," taught at the Institute for Applied Physics, TU Darmstadt, Darmstadt, Germany (August 2002).

37. Inrad, Inc., "BBO Crystals Data Sheet," http://www.inrad.com/pdf/Inrad_datasheet%20BBO%20Crystal.pdf (2002).

38. J. W. Blust, D. R. Ballal, and G. J. Sturgess, "Fuel effects on lean blowout and emissions from a well-stirred reactor," Journal of Propulsion and Power **15**, 216-223 (1999).

39. J. E. Nenniger, A. Kridiotis, J. Chomiak, J. P. Longwell, and A. F. Sarofim, "Characterization of a toroidal well stirred reactor," in *Twentieth Symposium (International) on Combustion* (Combustion Institute, Pittsburgh, PA, 1984), pp. 473-479.

40. SNLO nonlinear optics code available from A. V. Smith, Sandia National Laboratories, Albuquerque, NM 87185-1423, through www.sandia.gov/imrl/XWEB1128/xxtal.htm.

41. S. F. Hanna, R. Barron-Jimenez, T. N. Anderson, R. P. Lucht, J. A. Caton, and T. Walther, "Diode-laser-based ultraviolet absorption sensor for nitric oxide," Appl. Phys. B **75**, 113-117 (2002).

42. M. D. DiRosa and R. K. Hanson, "Collision-broadening and shift of NO $\gamma(0,0)$ absorption lines by H_2O, O_2, and NO at 295 K," J. Mol. Spectrosc. **164**, 97-117 (1994).

43. M. D. DiRosa and R. K. Hanson, "Collision-broadening and shift of NO $\gamma(0,0)$ absorption lines by O_2 and H_2O at high temperatures," J. Quant. Spectrosc. Radiat. Transfer **52**, 515-529 (1994).

44. M. F. Zabielski, L. G. Dodge, M. B. Colket, III, and D. J. Seery, "The optical and probe measurement of NO: a comparative study," in *Eighteenth Symposium (International) on Combustion* (Combustion Institute, Pittsburgh, PA, 1981) pp. 1591-1598.

45. M. E. Webber, "Diode laser measurements of NH_3 and CO_2 for combustion and bioreactor applications," Ph.D. dissertation (High Temperature Gasdynamics Laboratory, Department of Mechanical Engineering, Stanford University, Stanford, CA, 2001).

46. K. Annamalai, B. Thien, and J. Sweeten, "Co-firing of coal and cattle feedlot biomass (FB) fuels. Part II. Performance results from 30 kW_t (100,000) BTU/h laboratory scale boiler burner," Fuel (in press).

47. L. Levin, "Construction and design of an electro-optically tunable mode-hop-free external cavity diode laser," M.S. thesis (Division of Atomic Physics, Lund Institute of Technology, Lund, Sweden, 2000).

48. J. A. Silver, "Frequency-modulation spectroscopy for trace species detection: theory and comparison among experimental methods," Appl. Opt. **31**, 707-717 (1992).

APPENDIX A

THEORETICAL ABSORPTION PROGRAM

```
program absorption

implicit none

integer::i,j,species,numcol,numrow
double precision::NUlower,NUupper,NUstep,deltaNUc,deltaNUd,centerfreq
double precision::nlower(2),nupper,length,Temp,p,xgas(2),A21(13,10000)
double precision::t(6),c(6),s(6),ztot,pi,lightspeed,lntwo,h,kb
double precision::gamair(2,10000),gamself(2,10000),nbroad(2,10000)
double precision::c2,QTref(2),QTemp(2),PTemp,junk,numlines(2)
double precision::E(2,10000),NU21(13,10000),gamma,Sij(2,10000)

!Define constants
   !pi approximation
   pi=4.0d0*datan(1.0d0)

   !speed of light constant (cm/sec)
   lightspeed=2.99792458d+10

   !natural log of two approximation
   lntwo = 0.69314718056d0

   !Boltzmann's constant (J/K)
   kb=1.38054d-23

   !Planck's Constant (J-s)
   h=6.6260755d-34

   !second radiation constant (hc/k) in (cm-1 K)
   c2=h*lightspeed/kb

   !read Voigt Profile constants
   open(unit=15,file="t.txt",status="unknown")
   read(15,*)(t(j),j=1,6)
   close(15)

   !read Voigt Profile constants
   open(unit=16,file="c.txt",status="unknown")
   read(16,*)(c(j),j=1,6)
   close(16)

   !read Voigt Profile constants
   open(unit=17,file="s.txt",status="unknown")
   read(17,*)(s(j),j=1,6)
   close(17)

   !Read in parameters from Labview program
```

```
!Parameters are: lower laser frequency (cm-1), upper laser frequency
!(cm-1),frequency step for laser (cm-1), temperature (K),
! pressure (torr),concentration of gas 1 (NO or CO) (ppm),
!concentration of gas 2(CO2) (%),path length (m), collision-
!broadening coefficient (FWHM)(cm-1/atm), and
!species (1=NO, 2=OH, 3=CO and CO2)
open(unit=20, file="absparams.txt",status="unknown")
read(20,'(10d12.4)') NUlower,NUupper,NUstep,Temp,p,xgas(1),xgas(2),&
   & length,gamma,junk
close(20)
species=int(junk)

!Convert from % to ppm for CO2
xgas(2)=xgas(2)*1.00d4

!center frequency of scanning range (for frequency detuning for
!plotting)

centerfreq=(NUupper+NUlower)*lightspeed/2.00d9


if (species==1) then
   write(*,*) "Performing NO calculations..."

   !Define variables for NO

   !collisional width (cm^-1)    n=0.75 for N2 from Chang et al.
   deltaNUc=(p/760.0)*gamma*(298.0/Temp)**0.75

   !doppler width (cm^-1)
   deltaNUd=0.099d0*dsqrt(Temp/298.0)

   !opens Lifbase output file for emissions
   open(unit=10, file="Nospemj.txt",status="unknown")

   !opens Lifbase output file for frequency
   open(unit=11, file="NOfreqj.txt",status="unknown")

   !number of columns and rows in text file:
   numcol=13
   numrow=80

   !reads all emissions transitions (s^-1)
   read(10,*)((A21(i,j),i=1,numcol),j=1,numrow)

   !reads all frequency transitions (cm^-1)
   read(11,*)((NU21(i,j),i=1,numcol),j=1,numrow)

   !population of lower level (m^-3)
   nlower(1)=p*133.322368*(xgas(1)*1.0d-6)/(kb*Temp)

   !population of upper level (m^-3)
   nupper=0.0000d0
```

```
else if (species==2) then

   write(*,*) "Performing OH calculations..."
   !Define variables for OH

   !opens Lifbase output file for emissions
   open(unit=10, file="OH20a.txt",status="unknown")

   !opens Lifbase output file for frequency
   open(unit=11, file="OH20frq.txt",status="unknown")

   !number of columns and rows in text file:
   numcol=13
   numrow=25

   !reads all emissions transitions (s^-1)
   read(10,*)((A21(i,j),i=1,numcol),j=1,numrow)

   !reads all frequency transitions (cm^-1)
   read(11,*)((NU21(i,j),i=1,numcol),j=1,numrow)

   !collisional width (cm^-1)
   deltaNUc=(p/760.0)*gamma*dsqrt(298.0/Temp)

   !population of lower level (m^-3)
   nlower=p*133.322368*(xgas(1)*1.0d-6)/(kb*Temp)
   !write(*,*) "n1=",n1

   !population of upper level (m^-3)
   nupper=0.0000d0

else if (species==3) then
   write(*,*) "Performing CO calculations..."


   !CO Files*****************************
   !opens transition information file from Hi-Tran
   open(unit=10, file="COlines-hitemp-isotopes.prn",&
   &status="unknown")

   !opens partition sum information from HITran
   open(unit=11, file="CO_partition_sums.dat",status="unknown")

   !number of rows in text file
   numrow=357

   !reads all transitions frequencies (cm^-1),
   !line strengths (cm^-1/(molecule*cm^-2)), air and self broadened
   !halfwidths (cm-1/atm @296K), lower state energy (cm-1), and
   !coefficient of temperature dependence on air-broadened halfwidth
   !(all from HiTran)

   i=1
   j=1
```

```
do while (j<=numrow)
   read(10,'(d14.6,e11.3,f10.4,f10.4,d13.4,f8.2)')&
      &NU21(1,i),Sij(1,i),gamair(1,i),gamself(1,i),E(1,i),&
      &nbroad(1,i)
   if ((NU21(1,i)>=NUlower) .and. (NU21(1,i)<=NUupper)) then
      i=i+1
   else if (NU21(1,i)>NUupper) then
      exit
   end if
   j=j+1
end do
numlines(1)=i-1

!partition sum for CO at 296K from HiTran data
QTref(1)=107.116643

!reads partition sum information to find Q at reference temp
!and desired temp
read(11,'(f10.1,d12.6)') PTemp, QTemp(1)
do while ((PTemp/=Temp) .and. (PTemp<3000.0))
   read(11,'(f10.1,d12.6)') PTemp, QTemp(1)
end do


!CO2 Files*****************************
!opens transition information file from Hi-Tran
open(unit=15, file="CO2lines-hitemp-isotopes.prn",&
   &status="unknown")

!opens partition sum information from HITran
open(unit=16, file="CO2_partition_sums.dat",status="unknown")

!number of rows in text file
numrow=8690    !8690

!reads all transitions frequencies (cm^-1),
!line strengths (cm^-1/(molecule*cm^-2)),
!air and self broadened halfwidths (cm-1/atm @296K),
!lower state energy (cm-1), and
!coefficient of temperature dependence on air-broadened
!halfwidth (all from HiTran)

i=1
j=1
do while (j<=numrow)
   read(15,'(d14.6,e11.3,f10.4,f10.4,d13.4,f8.2)') NU21(2,i), &
     &Sij(2,i),gamair(2,i),gamself(2,i),E(2,i),nbroad(2,i)
   !write(*,*) NU21(2,i),Sij(2,i),gamair(2,i),gamself(2,i), &
      &E(2,i),nbroad(2,i)
   if ((NU21(2,i)>=NUlower) .and. (NU21(2,i)<=NUupper)) then
      i=i+1
   else if (NU21(2,i)>NUupper) then
      exit
   end if
```

```
         j=j+1
      end do
      numlines(2)=i-1

      !partition sum for CO2 at 296K from HiTran data
      QTref(2)=286.93107

      !reads partition sum information to find Q at reference temp
      !and desired temp
      read(16,'(f10.1,d12.6)') PTemp, QTemp(2)
      do while ((PTemp/=Temp) .and. (PTemp<3000.0))
         read(16,'(f10.1,d12.6)') PTemp, QTemp(2)
      end do

      !close CO2 Files
      close(15)
      close(16)

      !population of lower level (m^-3)
      nlower(1)=p*133.322368*(xgas(1)*1.0d-6)/(kb*Temp)           !CO
      nlower(2)=p*133.322368*(xgas(2)*1.0d-6)/(kb*Temp)           !CO2

      !population of upper level (m^-3)
      nupper=0.0000d0

   else
      write(*,*) "Invalid choice"
   end if

   !open file for output
   open(unit=13,file='out.txt',status="replace")

   if (species/=3) then
      !find partition function
      call partitionfunction(species,ztot)
   end if

   !find absorption for each frequency
   call findabsorption(species)

   close(10)
   close(11)
   close(13)



contains
!*****************************************************
!*****************************************************
!subroutine definitions
```

```
!*************************************************
subroutine partitionfunction(species,ztot)
!*************************************************
!calculate the partition function for the species

implicit none

double precision::B(0:7),Y(0:7),D(0:7),we,wexe,weye,alpha
double precision::F1,F2,zrot,F1zero,G,zvib,ztot,A,C,mu
integer::v,n,lambda,nmin,nmax,vmin,vmax,species

   !open(unit=1, file="zrot.txt",status="unknown")

   if (species==1) then
      !constants for NO
      v=0
      B(0)=1.696190d0
      D(0)=5.326d-6
      A=123.0372d0
      C=-1.1871d-3
      we=1904.405d0
      wexe=14.1870d0
      weye=0.0d0
      nmin=1
      nmax=80
      vmin=0
      vmax=10
      mu=D(v)/B(v)

      !Find rotational partition function
      zrot=0.00d0
      do n=nmin,nmax,1
         Y(v)=(A+C*(n)**2)/B(v)
         alpha=(Y(v)-2.0)**2/4.0+((n+1.0)**2-1.0)*&
            &(1+2.0*mu*(2.0*(n+1.0)**2-Y(v))+&
            &mu**2*((2.0*(n+1.0)**2-1.0)**2-1.0))
         F1=B(v)*((n+1.0)**2-1.0)-D(v)*((n+1.0)**4-(n+1.0)**2+1.0)-&
                  &B(v)*sqrt(alpha)
         Y(v)=(A-C*(n-1.0)**2)/B(v)
         alpha=(Y(v)-2.0)**2/4.0+((n)**2-1.0)*(1+2.0*mu*(2.0*(n)**2- &
            &Y(v))+mu**2*((2*(n)**2-1.0)**2-1.0))
         F2=B(v)*((n**2)-1.0)-D(v)*((n)**4-(n)**2+1.0)+B(v)*sqrt(alpha)
         zrot=zrot+2*(2.0*(n+0.5)+1.0)&
            &*dexp(-h*lightspeed*F1/(kb*temp))+ 2.0*(2.0*(n-0.5)+1.0)&
            &*dexp(-h*lightspeed*F2/(kb*temp))
      end do

   else if (species==2) then
      !Constants for OH
      v=0
      B(0)=18.515d0
      Y(0)=-7.547d0
      D(0)=0.00187d0
      we=3735.2d0
```

```
      wexe=82.2d0
      weye=0.0d0
      lambda=1
      nmin=1
      nmax=40
      vmin=0
      vmax=6

      !Find rotational partition function
      zrot=0.00d0

      do n=nmin,nmax,1
         F1=B(v)*(((n+1.0)**2)-(lambda**2)-0.5*sqrt(4.0*((n+1.0)**2)+&
            &Y(v)*(Y(v)-4.0)*(lambda**2)))-D(v)*(n**2)*((n+1.0)**2)
         F2=B(v)*((n**2)-(lambda**2)+0.5*sqrt(4.0*(n**2)+&
            &Y(v)*(Y(v)-4.0)*(lambda**2))) - D(v)*(n**2)*((n+1.0)**2)
         zrot=zrot+2.0*(2.0*(n+0.5)+1.0)*dexp(-h*lightspeed*
            &(F1)/(kb*temp))+2.0*(2.0*(n-0.5)+1.0)*dexp(-h*lightspeed*&
            &(F2)/(kb*temp))
      end do

   end if

   !Find vibrational partition function
   zvib=0.00d0
   do v=vmin,vmax,1
      G=we*(v+0.5)-wexe*(v+0.5)**2+weye*(v+0.5)**3
      zvib=zvib+dexp(-h*lightspeed*G/(kb*temp))
   end do

   !Total Partition function
   ztot=zvib*zrot

   !close(1)

end subroutine partitionfunction




!*****************************************************
subroutine findabsorption(species)
!*****************************************************

implicit none

integer::i,j,k,species
double precision::alpha21,A21i,NU21i,deltaxi,gci,k21i,g1,g2,gv
double precision::Njvalue,jvaluei,jupper,absorption,wr,wi,x,y,SijT
double precision::NUlaser,currfreq,freqdet,molecmass(2),gammacorr
double precision::lambda21i

   !Molecular Mass
   molecmass(1)=28      !CO
```

```
molecmass(2)=44      !CO2

!Initialize laser frequency
NUlaser=NUlower

if (species==3) then
!CO and CO2 from Hi-Tran

   !This DO LOOP adds up all the transition absorptions at each
   !laser frequency
   do while (NUlaser<=NUupper)

      !set Voigt Profile parameter to zero
      x=0.00d0

      !set absorption to zero
      absorption=0.0d0

      !index through species (k) and line strengths from HiTran file
      !(j)
      do k=1,2

         !set al.pha21 to zero
         alpha21=0.00d0

         do j=1,numlines(k)

            !gets transition frequency for current transition (first
            !column of array)
            NU21i=NU21(k,j)

            !calculate temperature and pressure correction of
            !halfwidth
            gammacorr=(296.0/Temp)**nbroad(k,j)*(gamair(k,j)*&
               &(p/760.0)*(1-xgas(k)*1.0d-6)+&gamself(k,j)*xgas(k)*&
               &1.0d-6*(p/760.0))

            !collisional width (cm^-1)   !factor of 2 for HWHM from
            !HITRAN
            !gamma is a scaling factor from Labview
            deltaNUc=2*gammacorr*gamma

            !doppler width (cm^-1)
            deltaNUd=7.162d-7*NU21i*dsqrt(Temp/molecmass(k))

            !set Voigt Profile outputs to zero
            wr=0.00d0
            wi=0.00d0

            !Voigt Profile parameter
            x=2*dsqrt(lntwo)*((NUlaser-NU21i)/deltaNUd)
            y=dsqrt(lntwo)*(deltaNUc/deltaNUd)

            call voigtfunction(x,y,wr,wi)
```

```
            gv=sqrt(lntwo/pi)*(2/deltaNUd)*wr

            !calculate line strength at specified temperature
            SijT=Sij(k,j)*QTref(k)*dexp(-c2*E(k,j)/Temp)*&
               &(1.0-dexp(-c2*NU21i/Temp))/(QTemp(k)*&
               &dexp(-c2*E(k,j)/296.0)*(1.0-dexp(-c2*NU21i/296.0)))
            !SijT=Sij(j)

            if ((int(NU21i)==2230)) then
               !write(*,*) NU21i,k,gammacorr,SijT
               !write(*,*) NU21i,k,deltaNUc,deltaNUd
            end if

            !term used to add up all transitions
            alpha21=alpha21 + SijT*gv

            !if (mod(j,100)==0) then
            !write(*,*) "NU21i=",NU21i,"Sij=",Sij(j)
            !write(*,*) "gv=",gv,"alpha=",alpha21
            !write(*,*)
            !end if

         end do !j loop

         !absorption,multiply by 100 to convert from m to cm
         !1.00d-6 to convert from cm^-1 to m^-3
         absorption=absorption+(1-dexp(-alpha21*length*100*&
            &nlower(k)*1.00d-6))

      end do !k loop

      !find laser frequency and frequency detuning
      currfreq=NUlaser*lightspeed/1.00d9
      freqdet=currfreq-centerfreq

      !output laser frequency and absorption
      write(13,'(f20.8,",",f20.8,",",f20.8)')&
         &NUlaser,freqdet,absorption
      !write(13,'(f20.8,",",f20.8,", stupid")') NUlaser,freqdet

      !increment laser frequency
      NUlaser=NUlaser+NUstep

   end do !NUlaser
!end CO calculations

else
!Files from LIFBase (NO and OH)

   !Voigt Profile parameter
   y=dsqrt(lntwo)*(deltaNUc/deltaNUd)

   !This DO LOOP adds up all the transition absorptions at each
```

```
!laser frequency
do while (NUlaser<=NUupper)

   !set al.pha21 to zero
   alpha21=0.00d0

   !set Voigt Profile parameter to zero
   x=0.00d0

   !do loop to extract columns from transition arrays
   do i=2,numcol,1

      !do loop to extract rows from transition arrays
      do j=1,numrow,1

         !gets transition frequency for current transition
         NU21i=NU21(i,j)

         !gets emission coeff for current transition
         A21i=A21(i,j)

         !first column of data file is j-value of the transition
         k=1

         !set Voigt Profile outputs to zero
         wr=0.00d0
         wi=0.00d0

         !gets current j-value for lower level of current
         !transition
         jvaluei=NU21(k,j)    !jground

         !find the j-value for the upper level
         select case(i) !column of the LIFbase file
         case(2,3,8,12)
            !deltaj=-1
            jupper=jvaluei-1
         case(4,5,10,11)
            !deltaj=0
            jupper=jvaluei
         case(6,7,9,13)
            !deltaj=1
            jupper=jvaluei+1
         end select

         !find degeneracies of upper and lower levels
         g1=2*jvaluei+1.0d0         !lower level
         g2=2*jupper+1.0d0          !upper level

         !find new number density value of the lower level
         call lowerdensity(species,jvaluei,i,Njvalue,NUlaser)

         !Voigt Profile parameter
         x = 2*sqrt(lntwo)*((NUlaser-NU21(i,j))/deltaNUd)
```

```
                if (NU21i > 0) then

                   call voigtfunction(x,y,wr,wi)

                   gv=sqrt(lntwo/pi)*(2/deltaNUd)*wr

                   !wavelength of the resonance (cm)
                   lambda21i=1/(NU21i)

                   !absorption line strength (1/(cm*s))
                   k21i=(((g2/g1)*Njvalue/(1.0d+6)-nupper)*&
                      &((lambda21i)**2)*A21i)/(4.0*2.0*Pi*lightspeed)

                   !term used to add up all transitions
                   alpha21=alpha21 + k21i*gv
                end if

             end do  !j loop

          end do  !i loop

          !absorption,multiply by 100 for units
          absorption=1-dexp(-alpha21*length*100.0)

          !find laser frequency and frequency detuning
          currfreq=NUlaser*lightspeed/1.00d9
          freqdet=currfreq-centerfreq

          !output laser frequency and absorption
          write(13,'(f20.8,",",f20.8,",",f20.8)')&
             &NUlaser,freqdet,absorption
          !write(13,'(f20.8,",",f20.8,",dumb")') NUlaser,freqdet

          !increment laser frequency
          NUlaser=NUlaser+NUstep

       end do  !Nulaser loop
    end if !NO and OH calculations


end subroutine findabsorption



!*****************************************************
subroutine lowerdensity(species,jvaluei,col,Njvalue,NUlaser)
!*****************************************************

implicit none

double precision::Njvalue,jvaluei,NUlaser,we,wexe,weye
double precision::v,F,G,n,alpha,mu,A,C,B(0:7),Y(0:7),D(0:7)
integer::lambda,col,species
```

```
if (species==1) then

   !Constants for NO
   B(0)=1.696190d0
   D(0)=5.326d-6
   A=123.0372d0
   C=-1.1871d-3
   we=1904.405d0
   wexe=14.1870d0
   weye=0.00d0
   mu=D(0)/B(0)
   v=0

   !Calculate rotational term energy
   select case(col)
   case(2,4,6,11,12,13)
      !i=1
      n=jvaluei-0.5
      Y(v)=(A+C*(n)**2)/B(v)
      alpha=(Y(v)-2.0)**2/4.0+((n+1.0)**2-1.0)*(1.0+2.0*mu*&
         &(2.0*(n+1.0)**2-Y(v))+mu**2*((2.0*(n+1.0)**2-1.0)**2-1.0))
      F=B(v)*((n+1.0)**2-1.0)-D(v)*((n+1.0)**4-(n+1.0)**2+1.0)-&
         &B(v)*sqrt(alpha)
   case(3,5,7,8,9,10)
      !i=2
      n=jvaluei+0.5
      Y(v)=(A-C*(n-1.0)**2)/B(v)
      alpha=(Y(v)-2.0)**2/4.0+((n)**2-1.0)*(1.0+2.0*mu*&
         &(2.0*(n)**2-Y(v))+mu**2*((2.0*(n)**2-1.0)**2-1.0))
      F=B(v)*((n**2)-1.0)-D(v)*((n)**4-(n)**2+1.0)+B(v)*sqrt(alpha)
   end select


else if (species==2) then

   !Constants for OH
   B(0)=18.515d0
   Y(0)=-7.547d0
   D(0)=0.00187d0
   we=3735.2d0
   wexe=82.2d0
   weye=0.00d0
   lambda=1
   v=0

   !calculate rotational term energy
   select case(col)
   case(2,4,6,8,9,10)
      !i=1
      n=jvaluei-0.5
      F=B(v)*(((n+1.0)**2)-(lambda**2)-0.5*sqrt(4.0*((n+1.0)**2)+&
```

```
            &Y(v)*(Y(v)-4.0)*(lambda**2)))-D(v)*(n**2)*((n+1.0)**2)
      case(3,5,7,11,12,13)
         !i=2
         n=jvaluei+0.5
         F=B(v)*((n**2)-(lambda**2)+0.5*sqrt(4.0*(n**2)+&
           &Y(v)*(Y(v)-4.0)*(lambda**2))) - D(v)*(n**2)*((n+1.0)**2)
      end select
   end if


   !Calculate vibrational term energy
   v=0
   G=we*(v+0.5)-wexe*(v+0.5)**2+weye*(v+0.5)**3

   !Calculate lower density
   Njvalue=nlower(1)*((2.0*jvaluei+1)*&
      &dexp(-h*lightspeed*(F+G)/(kb*Temp)))/ztot


end subroutine lowerdensity




!*****************************************************
subroutine voigtfunction(x,y,wr,wi)
!*****************************************************

implicit none

double precision::wr,wi,y1,y2,y3,r,r2
double precision::x,y,d,d1,d2,d3,d4
integer::k


!  do y=0.0,3.0,0.1

!     do x=0.0,4.0,0.1

!        wr=0
!        wi=0
      y1=y+1.5
      y2=y1*y1

      if(y>0.85.or.abs(x)<(18.1*y+1.65))then

         do k=1,6

            r=x-t(k)
            d=1.0/(r*r+y2)
            d1=y1*d
            d2=r*d

            r=x+t(k)
```

```
            d=1.0/(r*r+y2)
            d3=y1*d
            d4=r*d

            wr=wr+c(k)*(d1+d3)-s(k)*(d2-d4)
            wi=wi+c(k)*(d2+d4)+s(k)*(d1-d3)

         end do
!               write(10,*) y,x,wr

      else
!           end if


!        if (abs(x)<12) then

         wr=dexp(-x*x)

         y3=y+3

         do k=1,6

            r=x-t(k)
            r2=r*r
            d=1.0/(r2+y2)
            d1=y1*d
            d2=r*d
            wr=wr+y*(c(k)*(r*d2-1.5*d1)+s(k)*y3*d2)/(r2+2.25)

            r=x+t(k)
            r2=r*r
            d=1.0/(r2+y2)
            d3=y1*d
            d4=r*d
            wr=wr+y*(c(k)*(r*d4-1.5*d3)-s(k)*y3*d4)/(r2+2.25)
            wi=wi+c(k)*(d2+d4)+s(k)*(d1-d3)

          end do
!             write(10,*)y,x,wr

!        else
         end if

!     end do
!  end do


end subroutine voigtfunction


end program meen485_absorption
```

APPENDIX B

SHOT NOISE CALCULATIONS

The ultimate detection of the sensor has a fundamental limit known as the shot-noise limit. Shot noise arises because of the probabilistic nature of the photocathode emission process in the PMTs.[12] The statistical variance of this process is simply the number of photoelectrons created during the data collection process, N_e. The signal to noise ratio (SNR) at the shot noise limit is defined as the square root of the variance, or

$$SNR = \sqrt{N_e} \tag{B.1}$$

and the relative noise level (relative error, *RE*) at this limit is

$$RE = \frac{1}{SNR}. \tag{B.2}$$

To determine the number of photoelectrons created during the process, we use the current measured from the PMT during detection, I_{PMT}. The total number of photoelectrons emitted from the photocathode is

$$N_e = \frac{I_{PMT} \cdot \tau}{Gain \cdot e \cdot N_{channels}} \tag{B.3}$$

Where e is the charge per electron and τ is the measurement time. For the R166 PMTs from Hamamatsu, the gain was given as $1x10^7$. The measurement time for our experiments was 0.2 seconds per scan (5 Hz scan rate) for 32 scans averaged on the oscilloscope. Hence, the total measurement time was 6.4 seconds. The number of channels, $N_{channels}$, for our measurements was equal to the number of channels in the oscilloscope (10,000) divided by the number of channels binned in software.

For the gas cell experiments, 50 channels were binned in software, so $N_{channels}$=200. For the field demonstrations, only 20 channels were binned resulting in $N_{channels}$=500. For a maximum observed voltage of -55 V and an impedance of 1 MΩ, the calculated *RE* is $9.53x10^{-4}$ for the gas cell experiments and $1.51x10^{-3}$ for the field demonstrations. The difference in the two noise levels is due solely to the change in binned channels.

VITA

Thomas N. Anderson earned a Bachelor's of Science degree in Mechanical Engineering from Texas A&M University in December 2001, graduating Summa cum Laude. Part of his education was funded by a Walter W. Lechner Scholarship awarded by Texas A&M University. During his undergraduate education, he earned a number of awards including the Edwin S. Holdredge Award for highest GPA upon reaching senior status and the Simmang Award for Thermal Sciences. He was a member of multiple honor societies including the Pi Tau Sigma Honorary Mechanical Engineering Society where he served as an officer for two years. He was also active in the student chapter of the American Society of Mechanical Engineers (ASME), serving in various leadership roles for several years.

During the summers in his undergraduate career, he gained practical experience through internships with two major companies. In the summer of 1999 he worked at Standard Gypsum, LLC in McQueeney, Texas, assisting the plant engineer with various capital projects at a drywall manufacturing plant. The next summer he worked for Case Coporation in Burr Ridge, Illinois, in the mid-size tractor drivetrain design department.

In the fall of 2000, he began working in the Diode-Laser-Based Sensor Laboratory in the Mechanical Engineering Department at Texas A&M University under Dr. Robert Lucht. He initially helped with a diode-laser-based sensor for the hydroxyl radical before beginning work on a diode-laser-based sensor for nitric oxide. After starting graduate school in January 2002, he was completely responsible for the sensor development, including performing field tests in Ohio and Arizona.

While pursuing his Master's of Science degree at Texas A&M University, he earned a National Science Foundation Graduate Research Fellowship as well as fellowships from the Mechanical Engineering Department and the Texas Society of Professional Engineers. He was also actively involved with the Mechanical Engineering Graduate Student Organization, serving as secretary.

He can be reached permanently at 1901 Thormeyer Rd., Seguin, TX 78155.